

ATR-FTIR and Raman Imaging to Study Permanent and Primary Teeth From different Places and Ages.

Dissertation

Zur Erlangung des akademischen Grades doctor rerum naturalium

(Dr. rer. nat.)



seit 1558

vorgelegt dem Rat der Physicalische Chemie Fakultät
der Friedrich-Schiller-Universität Jena

von Master-Physik. Mohammad Anwar Alebrahim
geboren am 11.02.1982
in Irbid/Jordan

Gutachter:

- 1 PD. Dr. Christoph Krafft
- 2 Prof. Dr. Bernd Sigush

Datum der Verteidigung:

08-05-2013

Declaration of Originality

I certify that the work presented here is, to the best of my knowledge and belief, original and the result of my own investigations, except as acknowledged, and has not been submitted, either in part or whole, for a degree at this or any other university.

Ich erkläre, dass ich die vorliegende Arbeit selbstständig und nur unter Verwendung der angegebenen Hilfsmittel, persönlichen Mitteilungen und Quellen angefertigt habe und dass ich nicht die gleiche, eine in wesentlichen Teilen ähnliche oder eine andere Abhandlung bei einer anderen Hochschule als Dissertation eingereicht habe.

Mohammad Alebrahim.

CURRICULUM VITAE

Personal Details

Full name: **Mohammad anwar ali alebrahim**
Date of birth: 11th February 1982
Nationality: Jordanian
Current address: Tel: 004917677469616
Albert -Einstein str 9
07745 Jena
Germany
E-mails: mohammad.anwaralebrahim@ipht-jena.de
nmarneh@yahoo.com

Education

1999-2000 Certificate of secondary education, kharja Secondary School in Jordan.
2000-2004 Al Al-bayt university, AL-mafraq, Jordan. Bachelor of Physics.
2004-2006 Al Al-bayt university, AL-mafraq. Master in physics, graduated with honour degree.
Thesis: A study of Optical Properties of PMMA Iodine Mixture Thin Films Using Spectroscopic Ellipsometry.
2009-2013 PhD student at Jena university- Institute of photonic technology
Thesis: ATR-FTIR and Raman Imaging to Study Hard Tissue (permanent and primary teeth). By Prof, Jürgen Popp.

Work Experience

- Teacher in Ministry of Education, Jordan, for two years.
- Lecturer, Jordan College for Science and Technology.
- Researcher at institute of photonic technology in group of Optical Cell Diagnostics (PD. Dr Christoph Krafft).

Publications

ATR-FTIR and Raman imaging of primary and permanent. Calcified Tissue International.
Submitted

Research Interests:

Characterization of calcified tissues, (Dentin, Enamel, Bone).

Biomedical and dental materials for tissue replacements.

Vibrational Spectroscopic characterization and spectroscopically resolved chemical imaging (Infrared and Raman).

Optical properties of materials and photonic crystal by spectroscopic ellipsometry.

Other Qualifications

Extensive knowledge in:

- Vibrational spectroscopy/ Imaging & mapping (Raman and FTIR).
- Attenuated Total Reflectance (ATR).
- X-ray diffraction (XRD), X-ray fluorescence (XRF).
- Scanning electron microscope (SEM) and energy dispersive X-Ray analysis (EDX).
- Variable angle spectroscopic ellipsometry (VASE).

Computer capabilities

Using various computer application programs such as graphical and Analytical programs, Origin, Easy Plot, Acrobat, and office Packet.

Matlab, OPUS, Cytospec.

DEDICATIONS

To

My Mother and Father

My Brothers and Sisters

With Love

ACKNOWLEDGEMENTS

First of all, praise and all thanks for Almighty Allah for his assistance and protection.

A few sentences are too short to make a complete account of my deep appreciation for my supervisor Professor **Juergen Popp**. Who gave me a chance to do my PhD at University of Jena in Germany. His curiosity, dedication and passion for research impressed and influenced me deeply.

I am grateful for my co-supervisor **Dr. Christoph Krafft** who provided valuable suggestion to my work and was always available when I needed her help. It was his unflattering trust and constant encouragements which have been essential to my success through my study. I wish to thank him for his steady support in the most difficult times. His trust and honesty, his efforts in understanding a student's personality translated for me.

I would also like to thank my colleagues at institute of photonic Technology, for providing a stimulating and fun environment in which to learn and grow. It was a particular pleasure to work with them.

I wish to thank Professors Bernd W. Sigusch from Department of Conservative Dentistry, University Hospital Jena in Germany, Professors Sevgi Haman Bayari from Department of Physics Education, Faculty of Education, Hacettepe University in Turkey, and Dr. Wassef Shekhaneh Department of applied science (Archaeometry), Yarmouk University in Jordan, Whom provided me the teeth samples which were used in this work.

Table of contents

Dedication.....	vi
Acknowledgment.....	vii
Table of contents.....	viii
List of tables.....	x
List of figures.....	x
Zusammenfassung.....	xiii
Chapter1 Introduction	
1.1 Statement of the problem.....	1
1.2 Specific objectives.....	2
1.3 Presentations.....	2
Chapter 2 Literature review	
2.1 Tooth anatomy.....	4
2.1.1 Enamel.....	7
2.1.2 Dentin.....	8
2.1.3 Dentin Enamel Junction (DEJ).....	8
2.2 Hydroxyl apatite (HAP).....	9
2.3 Substitution in Hydroxyl apatite.....	11
2.4 Bone.....	13
2.5 Vibrational spectroscopy in mineralized tissue.....	14
Chapter 3 Materials, Methods and Theoretical Basis	
3.1 Origin of Infrared and Raman Spectroscopy.....	22
3.2 Vibrational theory of molecules and crystals.....	24
3.3 Selection rules for infrared and Raman spectra.....	26
3.4 Raman spectroscopy.....	27
3.5 Fourier transform infrared spectroscopy.....	29
3.6 Attenuated total reflectance.....	30

3.7	Chemical imaging (from classical to imaging).....	33
3.8	Spectral analysis.....	35
3.8.1	Univariate analysis.....	35
3.8.2	Multivariate analysis.....	35
3.9	Curve fitting.....	37
3.9.1	Second derivative spectra.....	38
3.9.2	Gaussian curve fitting.....	39
3.10	Materials.....	41
3.10.1	Dental materials.....	41
3.10.2	Sample analysis.....	42
3.10.3	Spectral data analysis.....	44
3.10.4	Tooth slice.....	44
Chapter 4 Result and discussion		
4.1	IR and Raman teeth spectra.....	46
4.2	Curve fitting results.....	50
4.3	Carbonate substitution on the apatite crystal.....	53
4.4	Mineral to matrix ratio.....	54
4.5	Carbonate to phosphate ratio.....	56
4.6	Cross links.....	59
4.7	Crystallinity.....	62
4.8	Raman dating of the archaeological teeth.....	65
Chapter 5 Result and discussion of DEJ		
5.1	Univariate analysis result	69
5.2	Multivariate analysis result.....	72
5.2.1	K-Means Cluster & hierarchical cluster analysis result.....	73
5.2.2	Vertex component analysis (VCA).....	75
Chapter 6 Conclusion.....		
		79
References.....		81

List of tables

Table 2.1 Raman and infrared spectroscopic band assignments for mineralized tissue.....	16
Table 2.2 Measures of human teeth properties by ATR-FTIR and Raman imaging.....	17
Table 3.1 Properties of IR subbands of A, A2 & B-type carbonate.....	53
Table 4.1 The band width of the ν_1 phosphate band of human dental tissues from permanent and primary teeth spectra \pm the standard deviation.....	65

List of figures

Fig. 2.1A: Beneath the erupted primary (baby or milk) teeth lie the permanent.....	4
Fig. 2-1B: Dental anatomy of the permanent teeth and primary one, illustrating.....	5
Fig. 2.2: Anatomy of tooth.....	6
Fig. 2.3: The crystal structure of hydroxyapatite, viewed along of c axis.....	10
Fig. 2.2: Crystallographic position diagram of CO_3^{2-} substituted of HAP structure.....	12
Fig 2.3: The hierarchical structure of bone at its various length scales.....	13
Fig. 2.4: Typical IR and Raman spectrum of the human permanent dentin.....	15
Fig. 3.1: Typical apparatus of IR spectroscopy.....	23
Fig. 3.2: Differences in mechanism of infrared and Raman spectroscopy.....	24
Fig. 3.3: Energy level diagram for Raman scattering.....	28
Fig. 3.4: The set-up of an interferometer.....	29
Fig. 3.5: Schematic representation of the ATR principle.....	31
Fig. 3.6: Data cube generated during one chemical imaging experiment.....	33
Fig 3.7: Three approaches exist to register one hyperspectral imaging data cube.....	34

Fig. 3.8: Classification of methods for extracting distribution maps and some examples.....	36
Fig 3.9: Fourier self deconvolution in details starting with a Lorentz line.....	39
Fig. 3.10: Gaussian curve-fitting of a sample spectrum.....	40
Fig. 3.11: Varian model 670, equipped with a microscope model 620, of a FTIR microscopic imaging.....	42
Fig. 3.12: Raman microspectrometer (Kaiser Optical System, AnnArbor, MI, USA).....	43
Fig. 3.13: Teeth slices from permanent and primary teeth illustrating the enamel and dentin.....	45
Fig. 4.1: Typical infrared and Raman spectra of permanent dentin and enamel	49
Fig. 4.2.1: Curve-fitting analysis of $\nu_1\nu_3$ phosphate of IR spectra.....	50
Fig. 4.2.2: Curve-fitting analysis of amide I profile of IR (A) and Raman (B) dentin spectra.....	51
Fig. 4.2.3: Curve-fitting analysis of carbonate IR permanent (C) & Raman (D) teeth spectra.....	52
Fig. 4.3A: ATR-FTIR and Raman images variation of mineral-to-matrix ratio of permanent and primary (German & Turkish) teeth.....	55
Fig. 4.3B: ATR-FTIR and Raman images variation of mineral-to-matrix ratio of permanent and primary Jordanian (Archaeological) teeth.....	56
Fig. 4.4: ATR-FTIR and Raman mapping of variation of carbonate to phosphate ratio in permanent & primary teeth.....	59
Fig. 4.5 A: ATR-FTIR and Raman variation of collagen crosslinking index of permanent & primary of German & Turkish teeth.....	61
Fig. 4.5 B: Raman variation of collagen crosslinking index of permanent & primary of archaeological teeth.....	62
Fig 4.6 A & B: ATR-FTIR variation of mineral crystallinity index of permanent & primary teeth.....	64
Fig. 4.7 A: I_{2941} / I_{960} relative intensities as a function of tooth burial period.....	67
Fig 4.7 B: I_{2941} / I_{960} relative intensities of Jordan ancient teeth.....	67
Fig. 5.1: scheme of a cross-sectional tooth slice.....	68
Fig. 5.2: Raman images and relative intensity ratios of the DEJ based on intensity ratios of 1450/960 at occlusal (A) and cervical (B) positions for permanent teeth.....	69

Fig. 5.3: relative intensity ratios of 1070/960 across the enamel/DEJ/dentinzone at occlusal (A) positions and at cervical (B) positions.....	70
Fig. 5.4: Raman spectra in protein-derived (A) and in mineral-derived (B) spectral regions from dentin and the DEJ.....	71
Fig. 5.5: representative average Raman clustering image (A) with three components and its related spectra (B).....	72
Fig. 5.6: Map of hierarchical cluster analysis	74
Fig. 5.7: Composite image of vertex component analysis (A) of a 70 x 70 Raman image from a permanent human tooth, of the first three components (B).....	76

Zusammenfassung

Zähne sind aus folgenden Schichten aufgebaut: Zahnschmelz, Zahnbein (Dentin), Zahnmark (Pulpa) und Zahnzement (Cementum). Der Zahnschmelz besteht zu 95% aus Hydroxylapatit, einem kristallinen Mineral, dessen Hauptbestandteile Calcium und Phosphat sind. Das unter dem Schmelz liegende Zahnbein enthält nur zwei Drittel kristallines Mineral. Da der Rest aus einer eiweißhaltigen Matrix – überwiegend dem Strukturprotein Collagen Typ 1 – und Wasser besteht, ist Dentin weicher als der Zahnschmelz. Es ist wohlbekannt, dass Karies schneller in Milchzähnen von Kindern als Zähnen von Erwachsenen fortschreitet. Dies steht mit großer Wahrscheinlichkeit mit dem unterschiedlichen Aufbau und Struktur im Zusammenhang, da Erwachsenenzähne mehr mineralisiert sind als Milchzähne. Diese unterschiedlichen Eigenschaften spielen insbesondere eine Rolle in der Zahnheilkunde wie der Behandlung von Karies in Milchzähnen.

Infrarot- (IR-) und Raman-Spektroskopie sind nicht destruktive und markerfreie schwingungsspektroskopische Methoden, die chemische und molekulare Analysen von mineralisierten Geweben wie Knochen und Zähne ermöglichen. Aufgrund von verschiedenen physikalischen Auswahlregeln von IR- und Raman-Spektroskopie unterscheiden sich Bandenintensitäten und Bandenbreiten und verschiedene spektrale Merkmale werden für die gleichen Eigenschaften herangezogen. Das Mineral zu Matrix Verhältnis kann bestimmt werden aus der intensivsten Bande von Hydroxylapatit, die in IR-Spektren um 1010 cm^{-1} und in Raman-Spektren um 960 cm^{-1} zentriert ist, und der intensivsten Protein-Bande bei 1660 cm^{-1} . Bandendekonstruktion wird angewendet, um überlappende Unterbanden in IR-Spektren zu trennen. Intensitätsverhältnisse einer IR-Bande bei 1415 cm^{-1} und eine Unterbande bei 1030 cm^{-1} werden für das Carbonat zu Phosphat Verhältnis berechnet, IR-Unterbandenverhältnisse bei 1660 und 1690 cm^{-1} für die Collagenquervernetzung und IR-Unterbandenverhältnisse bei 1030 und 1020 cm^{-1} für die Kristallinität von Hydroxylapatit. Die Substitution von Hydroxylgruppen in Hydroxylapatit durch Carbonate ergibt A, A2 und B-Typ genannte Geometrien, die durch IR-

Banden bei 878, 860 und 871 cm^{-1} repräsentiert werden. Intensitätsverhältnisse von Raman-Banden bei 1070 und 960 cm^{-1} werden für das Carbonat zu Phosphat Verhältnis berechnet, Raman-Unterbanden bei 1660 und 1690 cm^{-1} für die Collagenquervernetzung und der Halbwertsbreite der Raman-Bande bei 960 cm^{-1} für die Kristallinität von Hydroxylapatit.

Die Mehrzahl der IR- und Raman-Untersuchungen im Zusammenhang mit Zähnen sind für die Dentin-Adhesiv-Composite Verbindung von Zahnersatz durchgeführt worden. Nur wenige IR- und Raman-Studien existieren bisher für Milchzähne und deren Vergleich mit Erwachsenenzähnen. Die Ziele der vorliegenden Arbeit sind deshalb, zum ersten Mal die oben genannten schwingungsspektroskopischen Parameter für die chemischen und molekularen Eigenschaften von Milch- und Erwachsenenzähnen zu bestimmen. Dabei werden sowohl IR- als auch Raman-Merkmale analysiert, um die spektralen Ergebnisse jeweils zu bestätigen. Schwingungsspektroskopische Images wurden aufgenommen, um die spektralen und lateralen Informationen zu kombinieren. Die Spektren jedes Image wurden gemittelt, um Variationen innerhalb einer Probe zu kompensieren. Während aktuelle Proben aus der Türkei und Deutschland präpariert wurden, sind ebenfalls archäologische Proben aus Jordanien analysiert worden. Systematische Abweichungen zwischen Dentin und Zahnschmelz verschiedener Herkunft und Alter werden diskutiert.

Chapter 1

Introduction

1.1 Statement of the problem

Human body contains different kinds of tissue with similar cells and substances between those cells. Hard tissue is tissue that has become mineralized (bone & teeth); it has many cells that have become firm, hardened or rigid. Typically hard tissue is related to bones, teeth, kidney stones, gallstones and cartilage. Study of hard tissue is one of the most important in human evolutionary sciences, which lead to answer questions about how anatomy informs human development. Material science is an applied science based on relationship between the structure and properties of materials. The researchers use those results to synthesize new materials with special properties. Therefore, in this work we have investigated chemical structure, physical properties and the difference in the calcified tissues (enamel, dentin and the dentin enamel junction, DEJ) in human permanent and primary teeth from different places and different ages.

Enamel is the hardest and most mineralized part of the teeth and of entire body, about 96% of mineral (HA) (hydroxylapatite), 4% is water and organic materials. Dentin makes up the tooth and is less mineralized and less brittle than enamel with 75% of mineral (HA), 20% collagen and 5% water. These inorganic (minerals) and organic (collagen) are arranged in specific hierarchical structures. Convergence or separation zone (DEJ) from the enamel to the dentin with different properties in biomechanical and composition might have an important role in preventing crack propagation from enamel to dentin.

Numerous studies have been reported on permanent teeth, while only few investigations were the subject of primary teeth. It is known that the dentin properties of permanent teeth and primary teeth are different. Permanent dentin is more mineralized than primary tooth dentin [1]. These differences between permanent and primary teeth should be well known to enhance our materials in clinic dentistry. So far, these differences cause many clinical problems especially in restorative dentistry. The full understanding of the nature properties of dental human teeth (enamel and dentin) helps the researchers to develop the dental materials. For example, composite materials are commonly used in dental clinical which are softer than ceramics and at the same time we still suffer from real problems like the failure and micro-leakage. How can we

take advantage from our excellent understanding of the nature of these dental human teeth (enamel and dentin)? How researchers in biomaterials can develop the dental materials based on the nature of chemical properties of teeth? Do we have to use the same clinical treatments on repairing permanent and primary teeth?

In conclusion, the study of chemical and physical properties of dental human teeth (enamel and dentin) gives many advantages and benefits in biomaterial field to improve the synthesis of dental materials on respect to the nature properties of human teeth (permanent and primary).

1.2 Specific objectives

This dissertation based on IR and Raman spectroscopic aims:

- ❖ To investigate the chemical structure (inorganic and organic components) and physical structure of enamel and dentin of human teeth
- ❖ To compare that chemical and physical properties of the enamel and dentin of human permanent teeth with the primary ones.
- ❖ To study the carbonate substitution process inside the hydroxylapatite lattice of enamel and dentin, the A-type carbonate and B-type carbonate.
- ❖ To unveil the width of dentin enamel junction (DEJ), and its molecular features compared to the dentin and enamel by applying the multivariate spectral analyses, (hierarchical cluster HCA, K-means clustering, and vertex component analysis VCA).

1.3 Presentations

The study contains six chapters. The histological component of teeth based on hydroxylapatite with illustrating the substitutional process inside it, and background of previous investigations (literature review) are reviewed in chapter 2.

Chapter 3 includes the materials and methods which have been used in this study (preparation of teeth and their place provided).As well as, the work principle of Raman and IR spectroscopy are explained with the theoretical basis.

Chapter 4 and 5 are showing the results and discussion of composition parameters. In chapter 4 I show the curve-fitting of some Raman and IR spectral region to make sure that the hidden peaks which were used in this study existed or not. Chapter 5 contains Raman imaging result of dentin enamel junction (DEJ). Usually the study of hard tissue by Raman and IR imaging based on the height peak, its width or to the intensity ratio. Some of these intensities peak ratio became a standard method to quantify and qualify that tissue. For instance, mineral to matrix ratio, carbonate to phosphate ratio, collagen crosslinking, and crystallinity. Finally, the last chapter is the summary of this work and future work suggestions based on our finding.

Chapter 2

2.1 Tooth anatomy

The human teeth are divided into two sets of teeth, the primary teeth (commonly called baby teeth or deciduous teeth) and the permanent teeth (adult or secondary teeth). The main functions of teeth are to bite and chew food by helping of saliva to wet the food, and teeth also help in saying certain sounds. Fig. 2-1A, shows the childhood dentition where the permanent teeth in blue color take place of primary teeth in different ages depending on type of teeth as displayed in fig. 2-1B. Usually, there are 20 primary teeth poke through the gum over the time from 6 months to around 2 years. After 7-8 years those primary teeth start to fall out and they are replaced with 32 new permanent teeth.

Childhood Dentition



Fig. 2.1 A: Beneath the erupted primary (baby or milk) teeth lie the permanent teeth (shown in blue). The twenty primary teeth are replaced as the child grows. (<http://www.anatomywarehouse.com/anatomy-of-the-teeth-anatomical-chart-324>)

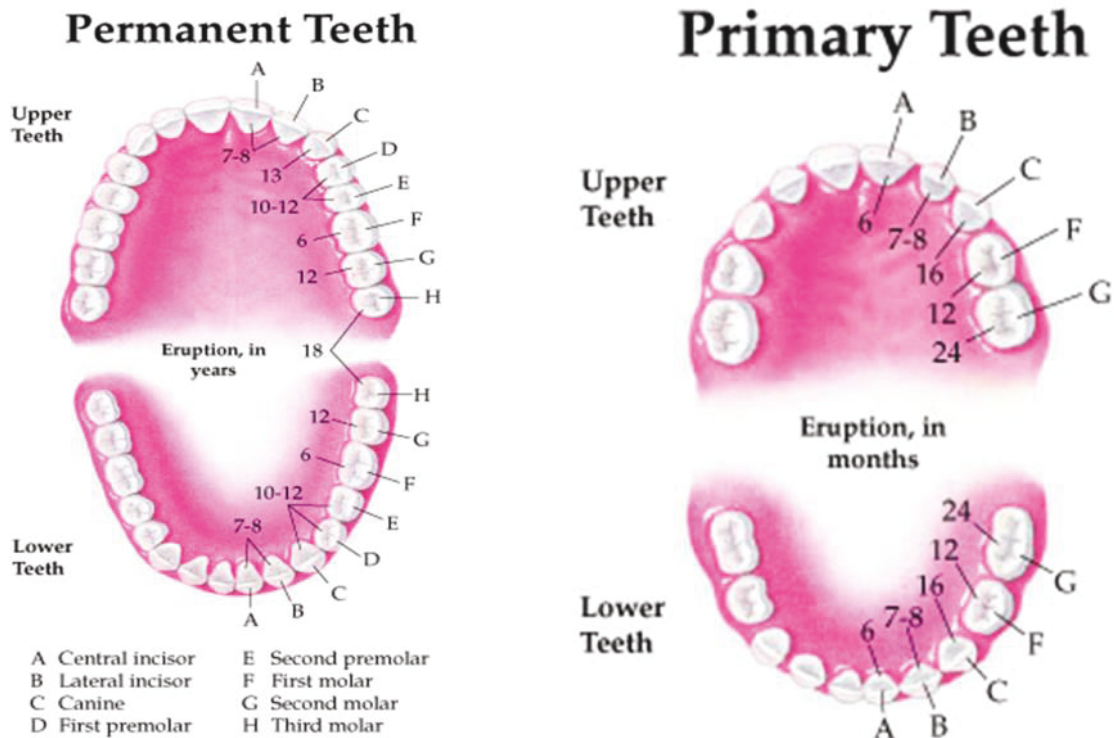
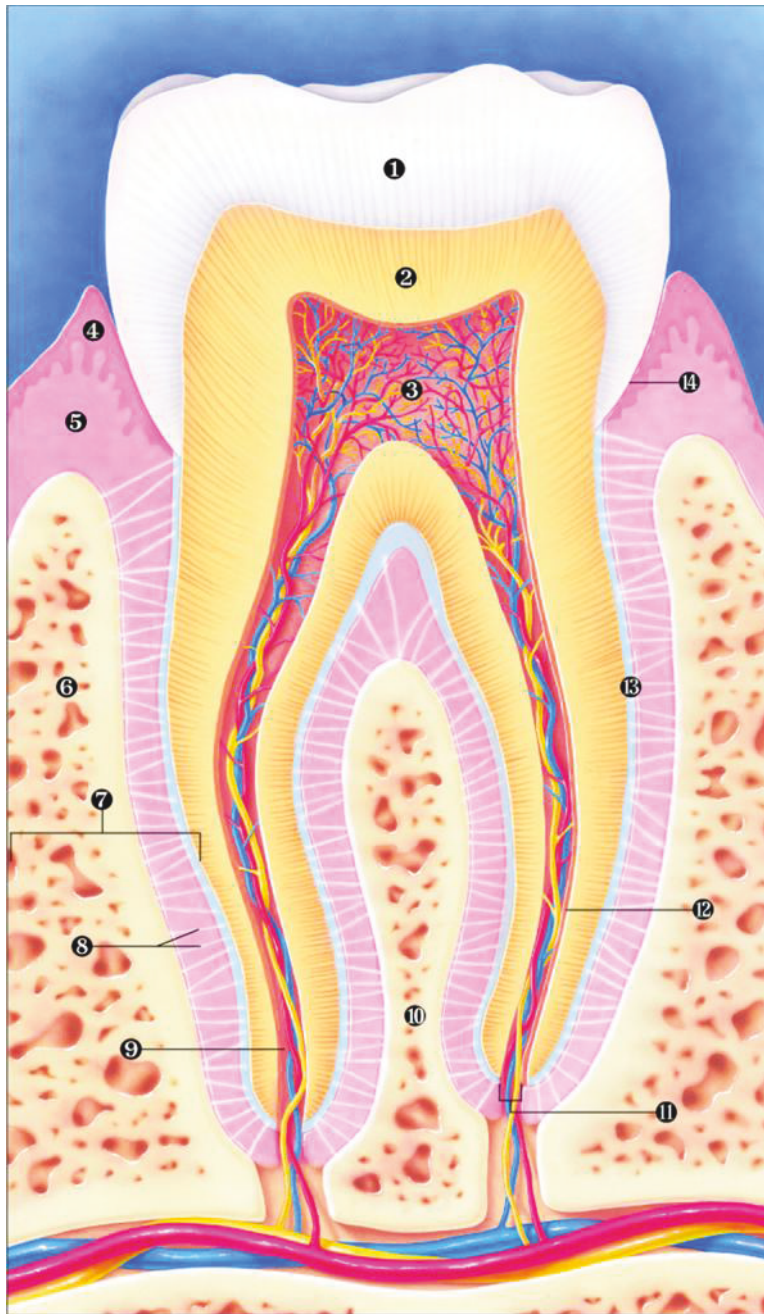


Fig. 2-1B: Dental anatomy of the permanent teeth and primary one, illustrating the age tooth comes in. (<http://www.anatomywarehouse.com/anatomy-of-the-teeth-anatomical-chart-324>).

The tooth is the hardest substance in the human body. It contains from several tissues with different composition (inorganic and organic materials). The main tissues are: enamel, dentin, cementum and pulp as shown in figure 2.2. The enamel which is the outer layer of tooth protects the dentin by help of the transition area (DEJ) from crack propagation. It contains mainly hydroxylapatite (HAP) and little amount of water and organic material. The normal color of enamel varies from light yellow to grayish white with thickness around 2.5 mm [2]. The enamel hardness is related to tightly arranged rows of calcium and phosphorus crystal within the organic matrix structure and it is harder than the bone. However, dentin is the second layer inside the tooth with less content of minerals and softer than enamel and more like bone. Dentin has microscopic channels (dentinal tubules) connect with the central nerve of the tooth within the pulp. These tubules include fluid and cellular structure, which increase the pain sensation [3].



- | | | |
|--|-----------------------------------|--------------------------|
| 1 Enamel | 5 Lamina propria of gingiva (gum) | 10 Interradicular septum |
| 2 Dentin, with dentinal tubules | 6 Bone | 11 Apical foramina |
| 3 Pulp chamber containing vessels and nerves | 7 Periodontium | 12 Odontoblast layer |
| 4 Gingival (gum) epithelium | 8 Periodontal membranes | 13 Cementum |
| | 9 Root canal | 14 Gingival sulcus |

Fig. 2.2: Anatomy of tooth.

(<http://www.anatomywarehouse.com/anatomy-of-the-teeth-anatomical-chart-324>).

The root of the dentin is covered with a thin layer called cementum. It is constructed from cells called cementoblasts, and it contains around 45% to 50% inorganic material (HAP) by weight and it is slightly softer than dentin. The upper substance of the cementum is the periodontal membrane which bonds the root of the tooth to the bone of the jaw [4]. The interior part of tooth is the pulp made up of soft tissue with blood vessels to provide nutrients to the tooth. The tooth can sense heat and cold by the nerves inside, as well as it has small lymph vessels to carry white blood cells to assist fight bacteria. Finally, the pulp extends within the tooth root by a root canal. This canal connects surrounding tissue via apical foramina (opening the tip of the root) which helps nerve and blood supply to the pulp [5].

2.1.1 Enamel

Enamel is about 95% mineral by weight and 87% by volume [6]. Most of this mineral is hydroxyapatite but its phase not pure (HAP), there are other apatites and other minerals such as magnesium and carbonates, these mineral components have been reported to vary from the outer enamel surfaces to the enamel dentin junction, and the density were reported to decrease towards the EDJ [7-11]. It is the hardest and most highly substance in the human body and it varies in thickness over the surfaces of the tooth, often thickest is 2.5 mm [12]. The normal color of enamel changes from white to grayish white and the enamel on primary teeth has a more opaque crystalline form and thus appears whiter than the permanent teeth. The basic unit in enamel is an enamel rod with 4-8 μm diameter found in rows along the tooth and it is perpendicular to the underlying dentin [8]. In permanent teeth the enamel rods near the cemento-enamel junction tilt towards the root of tooth. There are two types of enamel proteins that are not fully understood, amelogenin and amelins. The difficulties in protein investigation in the enamel are related to several reasons. The first one is the small amount inside the enamel which around 1% by weight or 7% by volume, and the second reason is the sample preparations and application of protein analysis techniques on a highly mineralized tissue, and also the conformations of protein usually were destroyed during the extraction and purification [13-14]. However there are only limited investigations on this topic till now.

Water forms hydrogen-bond bridges across adjacent peptide chains and maintains functional conformation of protein content remnants and collagen fibers in enamel, due to that. Water has

an important role in enamel functions because dehydration changes the mechanical properties of enamel [15-16].

2.1.2 Dentin

Dentin is a calcified tissue of the body, and along with enamel, cementum, and pulp is one of the four major components of teeth. Usually, it is covered by enamel on the crown and cementum on the root and surrounds the entire pulp. It is composed of approximately 50% inorganic material, 30% organic material and 20% fluid by volume. Dentin mineral is a carbonate rich, calcium deficient apatite [17]. It supports the tooth enamel and absorbs the pressure of eating, where the enamel would fracture when exposed to the forces of mastications without the dentin structure support. Its color is yellow and the tooth generally takes the same color due to the transparency of enamel. Dentin contains microscopic channels called dentinal tubules. The diameter is 2.5 μm near the pulp chamber and 0.63 μm near the dentin-enamel junction [18]. Similarly the number of the tubules is 45,000/ mm^2 near the pulp and 20,000/ mm^2 near the enamel [19]. The tubular net is liable for the intrinsic moisturizing of the tissue making the dentin a semi-permeable tissue. The difference between dentin and enamel is a lived and dynamic tissue [20-21].

The organic component is predominantly type I collagen with minor contribution from other proteins that can be categorized as phosphoproteins, glycoproteins and γ -carboxyglutamate-containing proteins [22]. The composition of dentinal fluid is reportedly similar to plasma but to date, it has been poorly characterized [23-24]. The mechanical properties of dentin are very important in determining tooth strength. It is well known that dentin properties of permanent teeth in adults and primary teeth in adolescents are different. Permanent tooth dentin is more mineralized than primary tooth dentin [7]. This difference can cause many clinical problems especially in restorative dentistry. The structure–property relationships of dentin vary with location, physiological, aging and disease processes.

2.1.3 Dentin enamel junction (DEJ)

The dentin enamel junction is the boundary between the enamel and the dentin that form the solid architecture of tooth [25]. In other words, the DEJ is the transition area from the outer layer of tooth (enamel) to the second one (dentin). It is characterized as scalloped border,

convexities of the enamel fit into corresponding concavities in the dentin. This adaptation is thought to enhance the bonding between enamel and dentin [26]. The scallops are micrometer-scaled (25 – 100 μm) in human tooth [27] and the amount and depth of the scallops was found to vary between species, type of teeth and between locations within single teeth [26-28]. DEJ is the initial location for cells that are responsible for the secretion of enamel and dentin [29]. The DEJ plays an important role in preventing crack propagation from enamel to dentin and inhibiting further catastrophic tooth fracture [30]. Because of this role (crack- preventing), the physical properties, such like, the width, microhardness and elastic modulus of the DEJ, become very critical information [31]. The chemical composition of the DEJ has been investigated as a series of 25-200 μm diameters scallops that contain 80-120 nm parallel Type-I collagen fibrils extending from the dentin into the enamel [30]. Previous studies, focused on determining single fracture parameter, such as toughness and width for DEJ, by considering the DEJ is a unique interface [32-33]. Some new results are focused on hardness and Young's modulus mapping across the DEJ from micro to nano-indentation [26, 34-36]. These mapping test show the elastic modulus decreases from around 70 GPa within enamel to around 20 GPa within dentin by the transition area (DEJ) with width 12-25 μm and around 100 μm determined by nanoindentation and microdentation respectively.

Researchers provide useful information to understand the morphology and the mechanical properties. For example, some results from optical spectroscopy [37] showed the median DEJ width was 10 μm ranging from 7 μm to 15 μm . On the other hand, new result by using Micro-Raman spectroscopy appeared that the width is dependent on the intratooth location [31]. They found that the width of transition zone is 12 ± 3.2 microns at occlusal position and 6.2 ± 1.2 microns at cervical position. So far, the state of transition zone by consideration its important role is still not fully understood.

2.2 Hydroxyl apatite (HAP)

Since the major component of tooth is the HAP, it is necessary to know its structure. HAP is a natural mineral consisting of a complex form of calcium apatite with chemical formula $\text{Ca}_{10}(\text{PO}_4)_6(\text{OH})_2$ [38]. HAP has a hexagonal symmetry and the crystal structure has been

described in the space group $P6_3/m$ with lattice parameters $a = b = 9.432 \text{ \AA}$, $c = 6.881 \text{ \AA}$ [39-40]. As shown in figure 2.3.

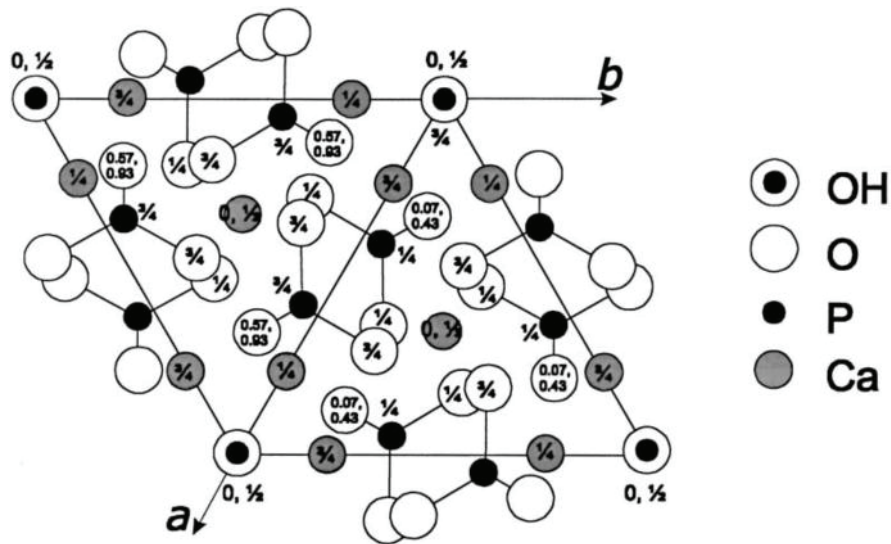


Fig. 2.3: The crystal structure of hydroxyapatite, viewed along of c-axis [41].

The structure consists of an array of PO₄ tetrahedra from a helix that occupies levels $Z = 0.25$ and $z = 0.75$ held together by Ca and OH ions. The ten calcium ions are arranged in two environments, and are designated Ca(I) and Ca(II). There are four calcium atoms in Ca(I) environments and six in Ca(II) environments. In general, hydroxyapatite (HAP), Ca₁₀(PO₄)₆(OH)₂, is used as a model for inorganic components of bones and teeth. However, apatites as they occur in biological tissues, mineral formations and laboratory products can incorporate a wide variety of impurities and are seldom found in pure stoichiometric form.

There are three types of pure calcium phosphate that have been classified based on the apatite structure:

- 1- The apatite type, Ca₁₀(PO₄)₆X₂, which includes the derivatives of hydroxyapatite (X = OH⁻)(HAP) and fluorapatite (X = F⁻) (FAP) as well as those related to apatite-type structures such as octacalcium phosphate (OCP), Octacalcium bis(hydrogenphosphate) tetrakis(phosphate) pentahydrate, Ca₈(HPO₄)₂(PO₄)₄·5H₂O and tetracalcium phosphate (TTCP), Ca₄(PO₄)₂O.
- 2- The glaserite type, which can be considered to include all polymorphs of tricalcium phosphates (TCP), Ca₃(PO₄)₂.

3- The Ca-PO₄ sheet-containing compounds, which include dicalcium phosphate dehydrate (DCPD), CaHPO₄·2H₂O, dicalcium phosphate anhydrous (DCPA), CaHPO₄, and monocalcium phosphates, Ca(H₂PO₄)₂·H₂O and Ca(H₂PO₄)₂ [42].

Hydroxyapatite is a thermally unstable compound, decomposing at temperatures from about 800-1200°C depending on its stoichiometry. The stoichiometry of hydroxyapatite is highly significant if thermal processing of the material is required. Calcium phosphate phases of alpha and beta-tricalcium phosphate, tetracalcium phosphate occur with slight imbalances in the stoichiometric ratio of calcium and phosphorus in HA from the molar ratio of 1.67. It is also important to know the close relation between the stoichiometry, acidity and solubility. Thus, it is known that the lower the Ca/P ratio and the larger the acidity of the environment, the higher will be the solubility of the HA [43].

2.3 Substitution in Hydroxyl apatite

HAP composes the inorganic phase of teeth and bone [44-45], and it is an essential and attractive material for biomedical applications [46-49]. Substitutions can occur in HAP for the calcium ions, the phosphate groups, or the hydroxyl group. In living tissue, substitution in the HAP by different cations helps maintaining a normal metabolism. One of the major substitutions in the biological apatite is CO₃²⁻, ranging approximately between 3 to 8% compared to others, such as Mg²⁺, Na⁺, K⁺, Cl⁻, F⁻ and many others ions [44, 50-51]. It is found that the substitution concentration is varied as a function of age [52]. For example, CO₃²⁻ was found to increase with age whereas the HPO₄²⁻ decreased. Also the materials properties of HAP including morphology, lattice parameters, stability, mechanical properties, and magnetic properties are affected by the incorporation of those cations, reviewed elsewhere [53-68]. For example, the replacement of some of the hydroxyl groups by fluoride ions, decrease solubility in acids [69]. Carbonate ions, on other hand, tend to disrupt a number of ionic interactions that stabilize apatite structure. This increases the susceptibility of enamel attack to carious attack.

Part of this study is about the substitution process of CO₃²⁻ in biological HAP inside the enamel and dentin of permanent and primary teeth by using the FTIR spectroscopy. It is known that the chemical environment in bioapatites is more complicated than the synthesis one [70]. This means that the HAP substituted in living tissue, is not really understood like synthetic HAP.

Inside the HAP lattice structure, CO_3^{2-} ions exchanged with OH^- groups to create the A-type carbonate, or take place of PO_4^{3-} tetrahedra to create the B-type carbonate [71-72]. The association of the CO_3^{2-} ions with apatite has been studied by many different methods: molar composition determination [73], X-ray diffraction [52, 73-77], infrared spectroscopy [71-79], electron spin resonance [77, 80], and Raman spectroscopy [81-82]. For example, the interesting mechanism due to the CO_3^{2-} incorporation into the biological apatite was proposed by *Legros and co-workers* [83]. By using Fourier transform infrared (FTIR) spectroscopy and X-ray spectroscopy from *Leventouri and co-workers*, they reported that both A and B-type carbonate substitutions with the B-type carbonate greater than the A-type carbonate by a factor up to 5. Same group deduced that the increase of the carbonate content as function of age from the ratio of the $\nu_2 \text{CO}_3$ to the $\nu_1 \text{PO}_4$ modes [52]. As shown in figure 2.2, the formation of a vacancy in O-III or O-III', was assumed, while PO_4^{3-} was exchanged with CO_3^{2-} [83]. In order to maintain the charge balance in the whole HAP structure, the negative charge due to the vacancy of O-III or O-III' was positively charged by releasing one Ca^{2+} and one OH^- [83].

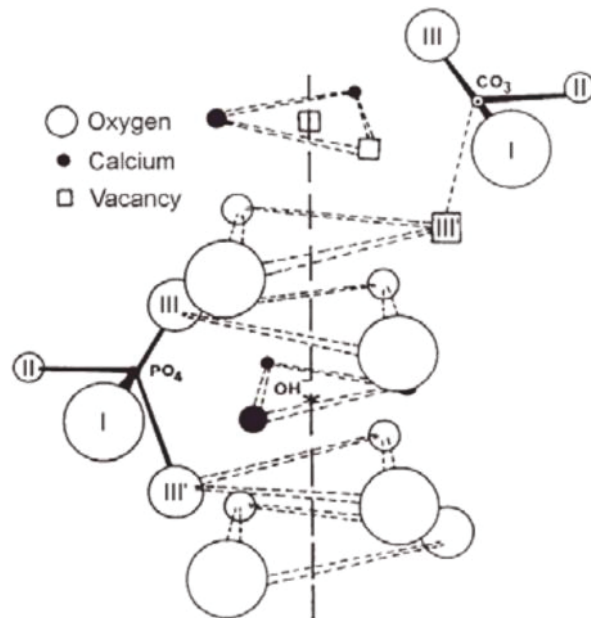


Fig. 2.2: Crystallographic position diagram of CO_3^{2-} substituted of HAP structure [84].

2.4 Bone

In quick scan of other typical hard tissues will help to understand some general concepts of nature designs of hard tissue. Bone tissue is a specialized form of connective tissue and is the main element of the skeletal tissues. It consists of structural features across unique hierarchical structural scales from nanocrystal scale to macrostructure shape, as illustrated in figure 2.3.

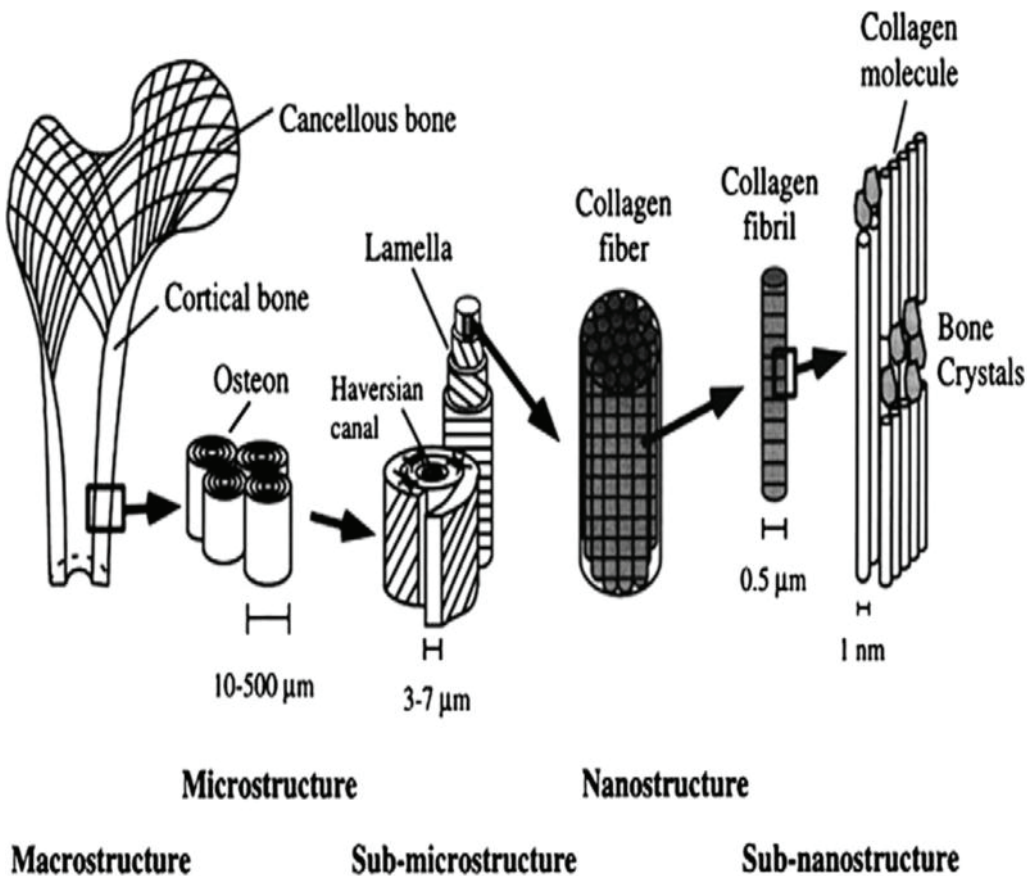


Fig 2.3: The hierarchical structure of bone at its various length scales. The microstructure of cortical bone consists of osteons with Haversian canals and lamellae, and at the nanoscale, the structural units are collagen fibers composed of bundles of mineralized collagen fibrils [85].

Bone composes of cells and an extracellular matrix in which fibers are embedded. Bone tissue is unlike other connective tissues in that the extracellular matrix becomes calcified. There

are two main categories of macrostructure of bone, the first one is the cancellous bone (spongy bone), which is composed of lattice or network of branching bone specules. The second one is the cortical bone (compact bone), appears as amass of bony tissue lacking spaces visible to the unaided eye. The bone matrix has two main components, the organic matrix which is composed of type I collagen fibers (about 95%) embedded in an amorphous ground substance. The inorganic component forms from hydroxyapatite $\text{Ca}_{10}(\text{PO}_4)_6(\text{OH})_2$ [86-87]. The same thing as in teeth the hydroxyapatite crystals in bone are imperfect due to other anions and cations, specially magnesium, chloride, and fluoride ions. Carbonate substitution inside HAP crystals of bone is the most important. Carbonate ions occupy phosphate ions in the crystal (A-type substitutions) and it replaces hydroxide ions (B-type substitutions). Its importance based to direct effect of quality to that tissue such as its solubility [88].

As a brief comparison between the bone and teeth, for example, the mineral phase of enamel includes large HAP crystals, whereas bone has small ones with more substitutions vacancies. These differences increase the elasticity of bone compared to the enamel. Crystallographic analyses indicate that in bone and dentin phosphate is mostly replaced by carbonate, whereas in enamel it is usually replaced by with chloride [88].

2.5 Vibrational Spectroscopic Analysis in Mineralized Tissues

Recently, vibrational spectroscopy, both infrared (IR) and Raman, has been extensively used to study mineralized tissues. These tissues may have formed of physiologic or pathologic processes [89-99]. Teeth, bones and casified cartilage are formed by physiologic processes, whereas, kidney and salivary stones, atherosclerotic plaques, and other pathologic deposits are formed through pathologic processes. Vibrational spectroscopy has the considerable advantage of being sensitive to both the mineral and organic components of mineralized tissues, thus allowing the study of mineral-matrix interactions as well as each individual component's properties. Sample preparation is relatively simple for both types of spectroscopy and once the specimen is excised and sectioned, no further preparation is necessary. These spectroscopic techniques help to provide a complete picture of the composition unattainable by other

commonly used methods such as X-ray diffraction or nuclear magnetic resonance (NMR). IR and Raman spectroscopies enable studies at micron-scale spatial resolution. The diffraction-limited spatial resolution achievable when using IR spectroscopy is 10–20 μm , while the shorter wavelengths examined using the visible excitation of Raman spectroscopy yield a diffraction-limited spatial resolution of 1 μm or less.

Analyses of changes in mineral and matrix (organic phase) in healthy and diseased tissue provide significant information to assess that tissue quality. Recently, vibrational spectroscopic imaging has become widely used in hard tissue studies, and it is recommended to be an essential tool. Dental enamel and dentin have similar composition as other mineralized tissues but with more or less crystalline and more highly oriented mineral. Figure 2.4 represents the typical IR and Raman spectrum of dentin teeth, and the relative band assignments and position are summarized in Table 2-1.

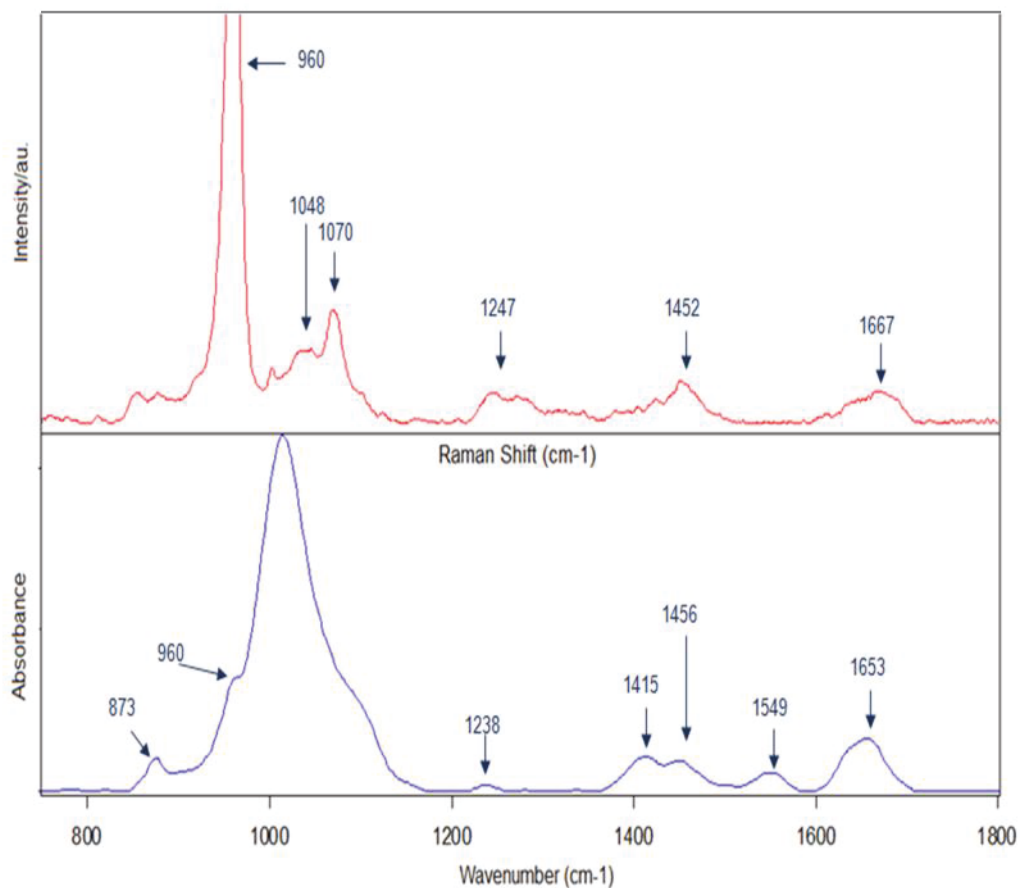


Fig. 2.4: Typical IR and Raman spectrum of the human permanent dentin.

Peak (cm ⁻¹)	assignment	observable
860	v ₂ of A2-type Carbonate (CO ₃ ²⁻)	IR
871	v ₂ of B-type Carbonate	IR
878	v ₂ of A-type Carbonate	IR
876	v ₂ of CO ₃ ²⁻	IR
960	v ₁ of PO ₄ ²⁻	IR, Raman
1003, 1013	HPO ₄ ²⁻	IR
1020	HPO ₄ ²⁻	IR
1030	apatitic Phosphate	IR
1048	v ₃ of PO ₄ ²⁻	Raman
1055	v ₃ of PO ₄ ²⁻	IR
1070	v ₃ of B-type Carbonate	Raman
1240, 1248	Amide III	IR, Raman
1415	v ₃ of CO ₃ ²⁻	IR
1450	CH ₂ bending	IR, Raman
1545	Amide II	IR
1660, 1665	Amide I	IR, Raman
1660	Amide I (α -helix)	IR, Raman
1610	Amide I (aromatic rings)	IR, Raman
1630, 1678	Amide I (β -sheets)	IR, Raman
1645	Amide I (random coils)	IR, Raman
1690	Amide I (turns)	IR, Raman

Table 2.1: Raman and infrared spectroscopic band assignments for mineralized tissue [99-103].

In hard tissue investigations the important advantage of both IR and Raman imaging is that they allow parameters imaging (table 2.2) that measure tissue quality and competence. These are more often measured as band height or band area ratios, and in some cases as band area widths.

Parameter	Definition (IR imaging)	Definition (Raman imaging)
Mineral-to-Matrix Ratio	Area of 900–1200 cm^{-1} phosphate band/area of amide I band (1590–1720 cm^{-1})	Area of 900–1000 cm^{-1} phosphate band/area of amide I band (1590–1720 cm^{-1})
Carbonate-to-phosphate ratio (C/P)	Intensity ratio of CO_3 band at 1415 and PO_4 at 1030 subband	Intensity ratio of CO_3 band at 1070 and PO_4 at 960 cm^{-1}
Collagen Crosslinks	Intensity ratio of subband at 1660 and 1690 cm^{-1}	Intensity ratio of subband at 1660 and 1690 cm^{-1}
Crystallinity	intensity ratio of subbands at 1030 and 1020 cm^{-1}	FWHM of phosphate peak at 960 cm^{-1}

Table 2.2: Measures of human teeth properties by ATR-FTIR and Raman imaging, adapted from reference [104, 105].

In the IR spectrum the mineral to matrix is a measure of the mineral content, and it is calculated as the ratio of the integrated Phosphate $\nu_1 \nu_3$ envelope at (900 – 1200 cm^{-1}) to the collagen amide I envelope at (1600 – 1700 cm^{-1}) [98]. This has been correlated with the ash weight [106]. Measure is similar in Raman spectra, by using the Phosphate envelope ν_1 alone [91] or the ratio of the Phosphate envelope ν_1 to the amide I envelope. The amide envelope is sensitive to the state of collagen crosslinking [107] and, more generally, to changes in the hydrogen bonding in collagen fibrils. For example, in dentin equilibrated with alcohols or

acetonitrile, the components of the amide I envelope shift to slightly different wavenumbers, and their intensities increase dramatically with the displacement of water [108].

Carbonate to phosphate ratio, in the IR spectrum is calculated from the area of CO_3^{2-} ν_2 component at 866 cm^{-1} (labile carbonate), 871 cm^{-1} (B-type carbonate), and 878 cm^{-1} (A-type carbonate) and the area of PO_4^{2-} ν_1 ν_3 envelope [109]. In Raman spectra the carbonate band assignment was difficult because of the overlap of the major carbonate ν_1 mode at 1070 cm^{-1} with a component of phosphate ν_3 1076 cm^{-1} in carbonated apatite [110]. These bands have been assumed to be a single broad carbonate band [100].

Crystallinity is a metric related to mineral maturity, and it is a measure of mineral crystallite size, mineral maturity and the amount of the substitution into apatitic lattice. Crystallinity increases when the crystals are larger and more perfect (less substitution). It is directly proportional to the inverse width of the 002 reflection (c-axis reflection) in the powder X-ray diffraction pattern of teeth or bone mineral [111]. In the IR spectrum the crystallinity is calculated from the subbands intensity ratio of 1030 cm^{-1} to the 1020 cm^{-1} , the band at 1030 cm^{-1} is a component of PO_4^{2-} ν_3 , while the 1020 cm^{-1} has been attributed to HPO_4^{2-} [109, 112]. These correlation bands should be usable in Raman spectrum, but the literature review of hard tissue (bone and teeth) focused on the width of the phosphate ν_1 band at 960 cm^{-1} to calculate the crystallinity from Raman spectra [113].

Collagen crosslinking is measured as changes in amide I envelope [107, 114]. The biochemical analysis of collagen model peptide showed that pyridinoline (Pyr) crosslinks resulted in a band at 1666 cm^{-1} and dehydrodihydroxylysinoxaline (de-DHLNL) crosslinks at 1690 cm^{-1} . These bands have been used in the IR spectrum to detect the collagen crosslinks, similar matrices also used in Raman spectra [115-116]. From the previous work, it is known that the Pyr crosslinks content increases with bone collagen maturity, while the de-DHLNL crosslinks decreases [117].

Vibrational spectroscopy, both infrared (IR) and Raman, has been employed by an increasing number of researchers in the study of dental hard tissues and relative materials. For instance, Primary teeth present structural differences from permanent teeth, such as lesser thickness of dentin and proportionally bigger pulp chamber than its successor teeth [118]. The dentin quality of primary and permanent teeth was inspected by Fourier transformed Raman spectroscopy (FT-Raman) scanning electron microscopy/energy-dispersive spectroscopy (SEM/EDS) and hardness test [119-121]. That group found that the inorganic content molecular arrangement of primary dentin is different from permanent dentin. The hardness was similar to primary and permanent dentin, decreasing to both only after acid etching and the organic content is modified by acid etching in primary dentin as well as in permanent dentin. It has been reported by using micro-Raman spectroscopy to differentiate between sound and eroded primary enamel that there was no statistically significant difference found between phosphate group concentration [122]. *Gunilla klinger and co-workers* have been studied the primary teeth by using a polarized light microscope, and scanning electron microscope, and X-ray microanalysis [123]. They found that there were several aberrations of both enamel and dentin in primary teeth from patients with Ehlers-Danlos syndrome (EDS), and they explained that the occurrence of both more dental caries and tooth fractures in patients with EDS. The changes in properties of the maturing mantle and circumpulpal dentin were quantitatively analyzed by *K. verdelis and co-workers* [124]. That study showed differences between mantle and circumpulpal dentin in the pattern of that changes. Analysis of the molecular structure of human enamel with fluorosis using micro-Raman spectroscopy and compare it with that of healthy enamel, has been studied by *Verónica Zavala-Alonso et al.*, The integral areas of ν_1 (960 cm^{-1}) phosphate peak as well as B-type carbonate peak (1070 cm^{-1}) were obtained to analyze structural differences. The mean of integral areas of ν_1 phosphate peak indicated greater mineralization in the severe fluorosis group and the mineralization of the carbonate peak at 1070 cm^{-1} decreased significantly in fluorotic groups [125]. *M.T. Kirchner et al.*, They have investigated the ancient and modern teeth by using (FT) Raman spectroscopy [126]. The investigation shows that the organic to inorganic ratio can be used to study the changes in dentine arising from burial conditions of interest both forensically and archaeologically. Moreover, Raman spectroscopy has enabled the measurement of stress in mineralized tissues by observing the $\text{PO}_4^{4-} \nu_1$ band shift [127-128]. The relationship between the peak position of Raman vibrational modes of interest and applied stress can be

investigated and calibrated by using standard samples with a loading apparatus. By assuming the axes of principal stress correspond to the main crystallographic directions of the crystal, the relationship can be expressed as: $\Delta\nu = \Pi_{ij} \sigma_{ij}$ where $\Delta\nu$ is the spectral shift of the selected Raman band, σ_{ij} and Π_{ij} are the stress and the piezo-spectroscopic coefficient, respectively [127]. *Pezzotti* reported the Π value of ν_1 phosphate band of a standard hydroxyapatite (HAP) sample under uniaxial stress, as 2.45 - 2.95 $\text{cm}^{-1}/\text{GPa}$ [127-128]. This technique has been used in the research of deformation [115] and fatigue [129] mechanisms of bone. In addition apatite minerals, water and proteins are also good infrared absorbers. IR spectroscopy has some advantages in observing water in hard tissue. Between 4000 and 400 cm^{-1} of enamel IR spectrum, four absorption bands associated to the water molecule are observed [130], while another report indicated a broad band at 3500-2900 cm^{-1} and another less intense band near 1642 cm^{-1} [101]. Moreover, infrared is a high sensitive technique for the detection of organic matrix in enamel and dentin. FT-IR photoacoustic phase analysis indicated a dramatic increase in the protein content relative to the phosphate content with increased depth from the enamel surface to a depth of about 200 μm [131]. Another IR investigation on the bleaching treatment on enamel illustrated the frequency of the Amide A and Amide I bands were significantly changed for enamel tissue after the treatment of high concentrations of bleaching agent [99]. *P. Fattibene et al.* also reported the decrement of IR band intensity above 1500 cm^{-1} after enamel deproteination [132].

The researchers have successfully applied the vibrational spectroscopy towards characterization of the adhesive dentin / enamel interface. *Sevgi Bayari and co-workers* have investigated the adhesive-dentin/enamel interface by using Raman microspectroscopy and small angle X-ray scattering, with different kind of adhesive materials [133]. The detailed Ramanspectroscopic characterization of the chemical structure and composition of adhesive resins, collagen and minerals include analysis of the adhesive–dentin interface with wet bonding [134], interfaces between self-etch adhesive systems and dentin [135], resin infiltration with single-step adhesive systems [136], dentin demineralization and adhesive penetration [137], novel adhesive systems using Silorane [138] and quantitative determination of adhesive resin [139]. Recently, besides univariate analysis, multivariate spectral analysis has also been applied in Raman imaging to unveil structural/chemical features of the adhesive–dentin interface [140]. The using of vibrational spectroscopy to study the interface area added excellent information to

understand very well the bonding between the dentin / enamel and the adhesive, such as, the penetration of the adhesive inside the tissue or the interaction between them specially the collagen cross linking.

In short, vibrational spectroscopy is a powerful tool for dental researchers. It has significant advantages for compositional analysis of dental tissue [141], in situ nano-mechanical observation [127], evaluation of dental treatments such as laser [142] and bleaching [99], and investigation of adhesive-dentin/enamel interface [133-140]. Therefore, we have used this technique in this study on permanent and primary human teeth.

Chapter 3

Materials, Methods and Theoretical Basis

Infrared and Raman spectroscopy provide information about the molecular makeup of materials [143-144], and thus have a wide range of applications to understand the nature of variety of materials types from the biological to the mineral phase [145]. The characteristic bands generated are typical for groups of chemical bonds and these can be used as a fingerprint to identify the material type. Infrared and Raman have different selection rules for generating spectra which are complementary. Furthermore, micro techniques are available to analyze small areas or individual grains. The analysis can often be carried out with no sample preparation, and is rapid, usually takes seconds of minutes to get single spectra or several minutes in imaging case for hard tissue measurements. With the recent development of the instruments it is possible for analysis to be carried out at locations. For these reasons the vibrational spectroscopy has been widely used for the characterization of many types of materials including the archaeological specimens [146].

3.1 Origin of infrared and Raman spectroscopy

In an infrared absorption experiment, infrared radiation with an intensity I_0 and frequency ν_0 is passed through a sample and the intensity of the transmitted light I is measured as a function of its frequency. Absorption of light at $\Delta E = h\nu$ occurs at frequencies corresponding to the energies of vibrational transitions. The function is described as Beer-Lambert law:

$$I = I_0 e^{-\epsilon cd}$$

Here, I_0 and I denote the intensities of the incident and transmitted beams, respectively, ϵ is the molecular absorption coefficient, and c and d are the concentration of the sample and the cell

length, respectively. In IR spectroscopy, both the percentage transmission (T), and absorbance (A) are usually plotted versus the wave number. The definitions of T and A are:

$$T (\%) = I/I_0 \times 100$$

And

$$A = \log I_0/I = \epsilon cd$$

For quantitative analysis, the absorbance should be used.

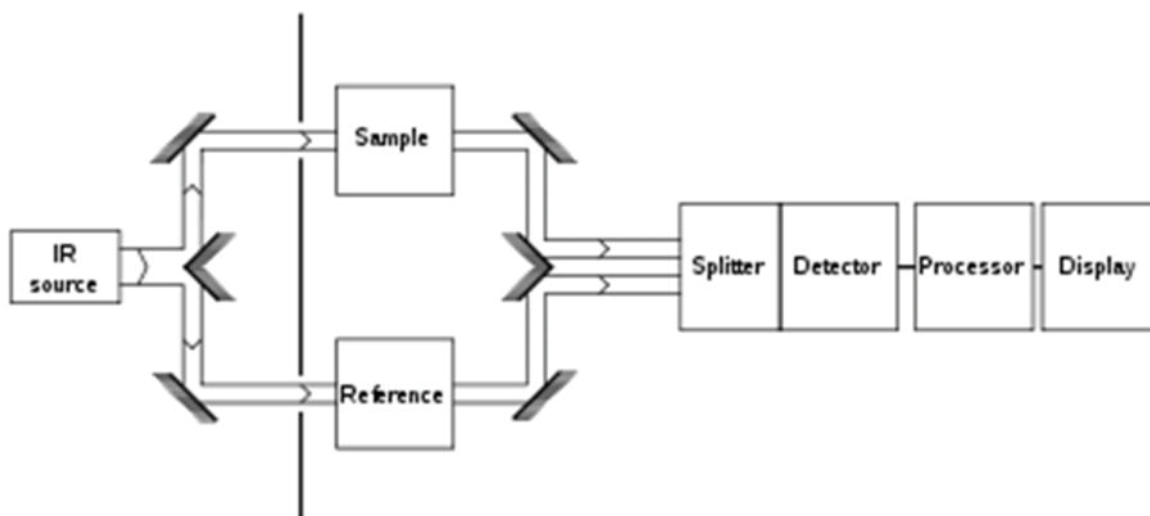


Fig. 3.1: Typical apparatus of IR spectroscopy, [Wikipedia, 2006].

A beam of infrared light is produced and split into two separate beams. One is passed through the sample, the other passed through a reference which is often the substance the sample is dissolved in. The beams are both reflected back towards a detector, however first they pass through a splitter which quickly alternates which of the two beams enters the detector. The two signals are then compared and a printout is obtained (Fig. 3.1).

The origin of Raman spectra is markedly different from that of IR spectra. In a Raman experiment, the sample is irradiated by a monochromatic laser beam (ν_0). Most of the incident light exits from the sample without change, but a small fraction (around 10^{-3} of the incident intensity) is inelastically scattered by atoms which can be observed in the direction perpendicular to the incident beam (Fig. 3.2). The scattered light consists of (1) Rayleigh scattering, strong and having the same frequency as the incident light beam (ν_0); (2) Raman scattering, very weak ($\sim 10^{-5}$ - 10^{-6} of the intensity of the incident laser beam) and having frequencies ($\nu_0 \pm \nu_m$), where ν_m

is a vibrational frequency of a molecule. The $\nu_0 - \nu_m$ and $\nu_0 + \nu_m$ lines are called the Stokes and anti-Stokes lines, respectively. Thus the Raman lines appear as weak peaks shifted in frequency from the Rayleigh line.

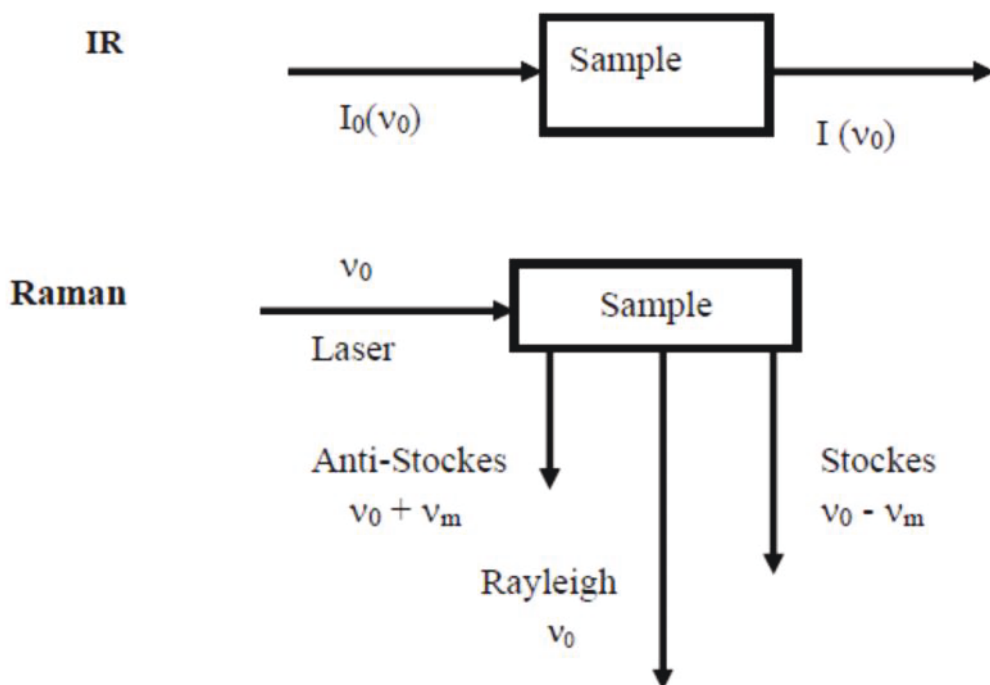


Fig. 3.2: Differences in mechanism of infrared and Raman spectroscopy.

3.2 Vibrational theory of molecules and crystals

a) Classical mechanical methods

The model of vibrations of molecules and crystals is well established [147]. In this model, nuclei and the interatomic interactions are treated as point masses and springs. The atomic vibration about their equilibrium positions is described in terms of classical Newtonian mechanics. The vibrational motion is harmonic in time because the restoring force is directly

proportional to displacement. Vibration corresponding to particular atomic displacement patterns (normal modes of vibrations) can be identified from the solutions of motion equations.

b) Quantum mechanical models

This advanced model describes not only the basic features of vibrational motion but also explains why vibrational spectra are line spectra rather than continuous absorptions and the interaction of vibrations with light. This model is based on Schrodinger's wave equation which is constructed in terms of the vibrational displacement coordinates q_i and a potential energy function $V(q_i)$. A set of vibrational wave function Ψ_i resolved from the partial differential equations in the vibrational wave equation describes a set of vibrational normal mode, and a set of quantized energy. In a vibrational spectroscopic experiment, a transition between vibrational levels with quantum numbers v_i and v_j is excited, and light is absorbed or emitted with an energy corresponding to the separations between the levels.

c) Crystal lattice vibrations

The number of vibrational modes observed for a molecule is equal to $3N-6$ or $(3N-5)$ for a linear molecule) determined by the number of degrees of vibrational freedom. In the case of crystal, N is very large, but most of the modes are not observed in infrared and Raman spectroscopy. The reason for this is the translational symmetry of the atoms in the crystal. Crystal lattice vibrations occur in the form of displacement waves travelling through the crystal. These lattice waves can be described longitudinal or transverse depending on the nuclear displacements which are parallel or perpendicular to the wave propagation direction. The displacements of nuclei give rise to an oscillating dipole wave with the frequency equal to the oscillation frequency of individual atoms about their equilibrium positions and wavelength defined by that of the associated lattice vibration. Only the wave length of lattice vibrations is comparable to that of incident light (approximately 5×10^{-5} - 5×10^{-6} Å in IR, and usually 10^{-3} - 10^4 Å in Raman spectra), when an interaction of lattice vibration with incident light takes place. In these long wavelength lattice vibrations, the vibrations within adjacent unit cells are essentially in phase, so the number of vibrational modes which may be observed in IR or Raman spectroscopy is equal to $3N-3$, where N is the number of atoms in the primitive unit cell. These

3N-3 vibrations are termed the optic modes. The three acoustic branches are responsible for the propagation of sound waves through the lattice [148].

3.3 Selection rules for infrared and Raman spectra

Raman and infrared (IR) spectroscopies can provide information about the vibrational and vibrational rotational modes of molecules. Vibrational-rotational bands are generally observed with gaseous samples, where the molecules are able to rotate freely. In condensed (liquid or solid) phases, however, one only observes vibrational frequencies of the sample. IR and Raman spectroscopies are complementary techniques, since transitions allowed in Raman may be forbidden in IR or vice-versa. This depends on symmetry considerations. An IR-active mode is one in which a particular vibration causes a change in the dipole moment of the molecule, while only those vibrations which change the molecular polarizability lead to Raman scattering. Therefore the activity of a certain vibrational mode depends highly on its symmetry and the symmetry of the molecule. One simple symmetry rule is the so called mutual exclusion rule for molecules with a center of symmetry. In such molecules no normal mode may be active in both the infrared and the Raman spectrum. In other words, some vibrational modes of a molecule or a crystal are IR - active and not Raman-active or vice versa, and some modes are not observable at all. According to quantum mechanics, a vibration is IR-active if the dipole moment is changed during the direct interaction of light beam with an oscillating molecular dipole. In general, asymmetric vibrations tend to give stronger infrared absorption than symmetric species. Similarly highly polar molecules and crystals have stronger infrared spectra than non-polar samples. In Raman scattering, the light beam induces an instantaneous dipole moment in molecule by deforming its electronic wave function. If the polarizability is changed during vibration, then this vibration is Raman-active. In general, molecules containing easily polarizable atoms (such as I, S, Ti) have very strong Raman spectra, while similar molecules with less polarizable atoms (Si, C, O) have weaker spectra. Most symmetric modes tend to give the strongest Raman signals as these are associated with the largest changes in polarizability. For more complicated molecules and crystals, IR and Raman activities of vibrational modes can be simplified by use of the molecular or unit cell symmetry, and the method of group theory [147].

3.4 Raman Spectroscopy

When light is scattered from a molecule or crystal, most photons are elastically scattered. The scattered photons have the same energy (frequency) and, therefore, wavelength, as the incident photons. However, a small fraction of light (approximately 1 in 10^7 photons) is scattered at optical frequencies different from, and usually lower than, the frequency of the incident photons. The process leading to this inelastic scatter is termed the Raman Effect. Raman scattering can occur with a change in vibrational, rotational or electronic energy of a molecule. If the scattering is elastic, the process is called Rayleigh scattering. If it's not elastic, the process is called Raman scattering. Raman scattering (or the Raman Effect) was discovered in 1928 by V. C. Raman who won the Nobel Prize for his work. If the substance being studied is illuminated by monochromatic light, for example from a laser, the spectrum of the scattered light consists of a strong line (the exciting line) of the same frequency as the incident illumination together with weaker lines on either side shifted from the strong line by frequencies ranging from a few to about 3500 cm^{-1} . The lines of frequency less than the exciting lines are called Stokes lines, the others anti-Stokes lines. Raman spectroscopy is very important practical tool for quickly identifying molecules and minerals. A Raman spectrometer was deployed on the Viking landers in 1972 and in other missions. Raman spectroscopy also has important scientific applications in studying molecular structure. In this experiment we will study both kinds of applications.

The Raman Effect arises when a photon is incident on a molecule and interacts with the electric dipole of the molecule. In quantum mechanics the scattering is described as an excitation to a virtual state lower in energy than a real electronic transition with nearly coincident de-excitation and a change in vibrational energy. The scattering event occurs in 10^{-14} seconds or less. The virtual state description of the scattering is shown in Figure 3.3. The energy difference between the incident and scattered photons is represented by the arrows of different lengths in Figure 1. Numerically, the Raman shift in wave numbers (cm^{-1}), is calculated through equation by

$$\bar{\nu} = \frac{1}{\lambda_{\text{incident}}} - \frac{1}{\lambda_{\text{scattered}}}$$

In which the λ 's are the wavelengths (in cm) of the incident and Raman scattered photons, respectively.

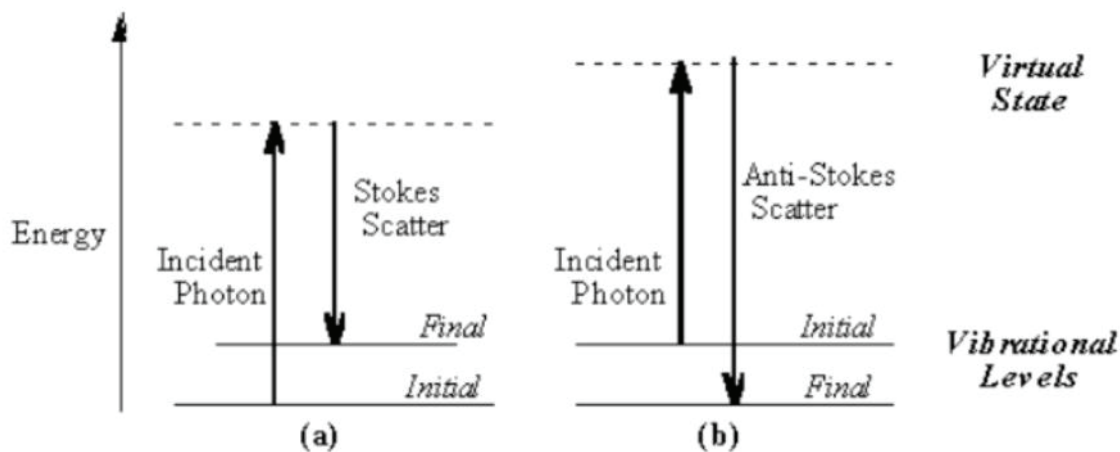


Fig. 3.3: Energy level diagram for Raman scattering; (a) Stokes scattering, (b) anti-Stokes scattering.

At room temperature the thermal population of vibrational excited states is low, although not zero. Therefore, the initial state is the ground state, and the scattered photon will have lower energy (longer wavelength) than the exciting photon. This Stokes shifted scatter is what is usually observed in Raman spectroscopy. Figure 3.3(a) depicts Raman Stokes scattering. A small fraction of the molecules are in vibrationally excited states. Raman scattering from vibrationally excited molecules leaves the molecule in the ground state. The scattered photon appears at higher energy, as shown in Figure 3.3(b). This anti-Stokes-shifted Raman spectrum is always weaker than the Stokes-shifted spectrum, but at room temperature it is strong enough to be useful for vibrational frequencies less than about 1500 cm^{-1} . The Stokes and anti-Stokes spectra contain the same frequency information. The anti-Stokes spectrum can be used when the Stokes spectrum is not directly observable, for example, because of poor detector response at lower frequencies [150-151].

3.5 Fourier transform infrared spectroscopy (FTIR).

Fourier transform infrared (FTIR) spectroscopy is a measurement technique for collecting infrared spectra. Instead of recording the amount of energy absorbed when the frequency of the infra-red light is varied (monochromator), the IR light is guided through an interferometer (Fig 3.4). The interferometer consists of an IR source, beamsplitter, two mirrors, a laser and a detector. IR radiation from the source is transmitted to the beamsplitter, which splits the beam into two. One of the split beams is reflected at a 90° angle onto a flat fixed mirror, while the other beam is transmitted to a flat mirror which moves back and forth at a constant velocity (Fig.3). The two beams are ultimately reflected from their respective mirrors and are recombined as they re-join at the beamsplitter. After passing the sample the measured signal is the interferogram. Performing a mathematical Fourier transform on this signal results in a spectrum identical to that from conventional (dispersive) infrared spectroscopy. FTIR spectrometers are cheaper than conventional spectrometers because building of interferometers is easier than the fabrication of a monochromator. In addition, measurement of a single spectrum is faster for the FTIR technique because the information at all frequencies is collected simultaneously. This allows multiple samples to be collected and averaged together resulting in an improvement in sensitivity. Virtually all modern infrared spectrometers are FTIR instruments.

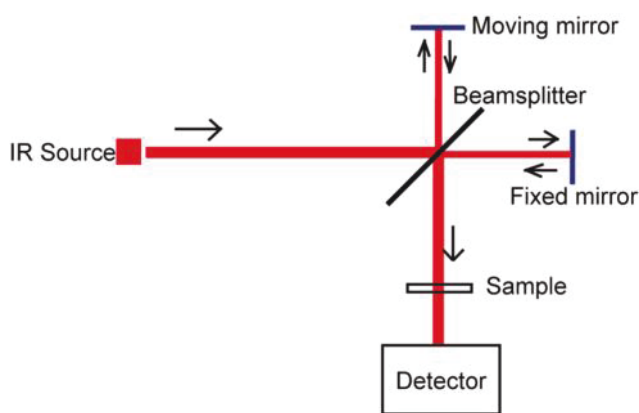


Fig.3.4: The set-up of an interferometer

3.6 Attenuated total reflectance (ATR)

Attenuated Total Internal Reflectance (ATR) Spectroscopy is a versatile and powerful technique for infrared sampling. Minimal or no sample preparation is usually required for rapid analysis. ATR is ideal for those materials which are strong absorbers. In addition, ATR is a useful technique for providing information about the surface properties or conditions of a material. The phenomenon of internal reflection was first reported in infrared spectroscopy in 1959. It was observed that if certain conditions were met, infrared radiation entering a prism made of a high refractive index infrared transmitting material (ATR crystal) will be totally internally reflected (Figure 3.4). This internal reflectance creates an evanescent wave which extends beyond the surface of the crystal into the sample held in contact with the crystal. In regions of the infrared spectrum where the sample absorbs energy, the evanescent wave will be attenuated [152].

The condition which must exist to obtain total internal reflectance is that the angle of the incident radiation, θ , must exceed the critical angle, θ_c . The critical angle is a function of the refractive indices of the sample and ATR crystal and is defined as

$$\theta_c = \sin^{-1} \frac{n_2}{n_1}$$

Where n_1 is the refractive index of the ATR crystal and n_2 is the refractive index of the sample. High refractive index materials are chosen for the ATR crystal to minimize the critical angle. A property of the evanescent wave which makes ATR a powerful technique is that the intensity of the wave decays exponentially with distance from the surface of the ATR crystal. The distance, which is on the order of microns, makes ATR generally insensitive to sample thickness, allowing for the analysis of thick or strongly absorbing samples [153].

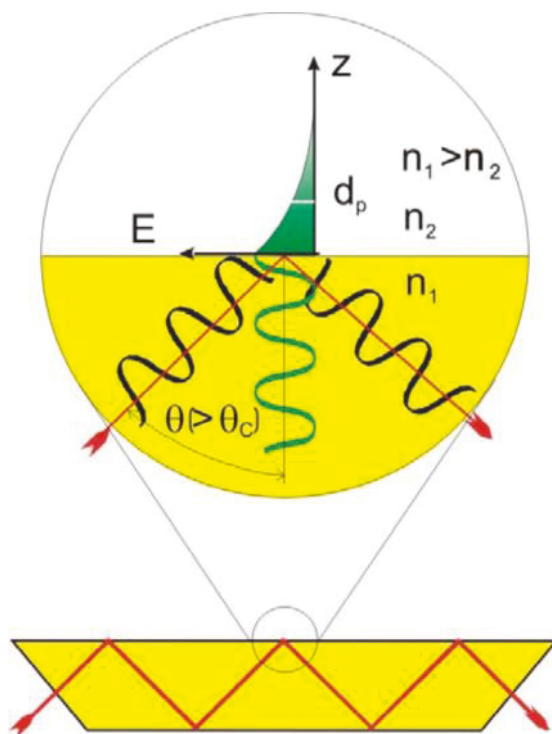


Fig. 3.5: Schematic representation of the ATR principle.

A useful relationship in ATR spectroscopy which can be used as a qualitative measure of the depth which the evanescent wave extends into the sample is defined as the depth of penetration, d_p . The depth of penetration is defined as the distance from the crystal-sample interface where the intensity of the evanescent wave decays to $1/e$ (approximately 37%) of its original value. It is calculated by:

$$d_p = \frac{\lambda}{2\pi \sqrt{n_1^2 \sin^2 \theta - n_2^2}}$$

The availability of different IR-ATR waveguide materials and geometries contributes to the development of a variety of IR-ATR sensing schemes. IR-ATR waveguides commonly include IR transparent optical fibers and ATR crystals. The former are typically made from materials including but not limited to silver halides (AgX), sapphire (Al_2O_3), and chalcogenides (AsSeTe glasses) the latter are typically made from zinc selenide (ZnSe), zinc sulfide (ZnS), Germanium (Ge), and silicon (Si). The physical properties and wavelength dependant transmittance of optical waveguides determines or limits their applicability for certain samples. The geometry and the

dimensions (e.g., thickness, length.) of optical waveguides can be adjusted to fulfill individual measurement requirements. In this thesis, prisms and hemispheres made from Germanium were utilized for the development of different IR-ATR sensing instruments for a variety of applications [153].

Fourier transform infrared imaging can provide both, spatial spectral information for the designated sample area. FTIR imaging couples an FTIR microscope system with a focal plane array (FPA) detector to enable the simultaneous collection of multiple spectra across the sampled area. The number of spectra collected per image is dependent on the size of the FPA; for example, a 32 X 32 array allows 1042 independent spectra to be collected in a single measurement. The images generated from the individual spectral bands are spatially resolved maps providing the location of each component in the sampled area. When operated in reflection or transmission mode FTIR has a maximum lateral resolution of around 5 – 10 μm . This spatial resolution is limited by diffraction and furthermore may not always be achievable because of signal-to-noise ratio consideration. For instance, *Verdelis et al.* were able to track maturation mineralization in early childhood dentin [154]. The spatial resolution achieved using transmission imaging allowed characterization of all stages of the dentin maturation.

Using the ATR attachment on the infrared microscopy system offers an increased spatial resolution of around 2 – 3 μm [155], because of the change in wavelength of the light as it passes through the internal reflection element. ATR can be applied to sample that are poorly reflective or not suitable for transmission measurements. Theoretical spatial resolution is dependent on the wavelength of the incident light and the numerical aperture of the objective lens and is given by the Rayleigh criterion

$$r = \frac{1.22 \lambda}{2NA}$$

Where, λ is the wavelength of the incident light, and NA is the numerical aperture

and

$$NA = n \sin \theta$$

Where, n is the refractive index of the ATR element and θ is the half the angular aperture [155].

3.7 Chemical imaging (from classical to imaging)

With classical spectroscopy one spectrum reflects the integrated information of the sample surface. Therefore the scientist acquires only mean information about the sample. Since the end of the 20th century the technical improvements have allowed the development of new detectors or methods to acquire simultaneously spectral and spatial information. This technique is referred as "chemical imaging". Spectra are spatially located and it is possible to identify the chemical species inside the samples and also to map their distributions. A chemical imaging experiment generates a three-way matrix called a data cube as shown in Figure 3.5. Two dimensions n and m depict the spatial localizations of the chemical species and one dimension allows their identification. Several thousands of spectra can be acquired with chemical imaging depending on the detector size. Those spectra contain more than a hundred wavelengths, that is why data are called hyperspectral.

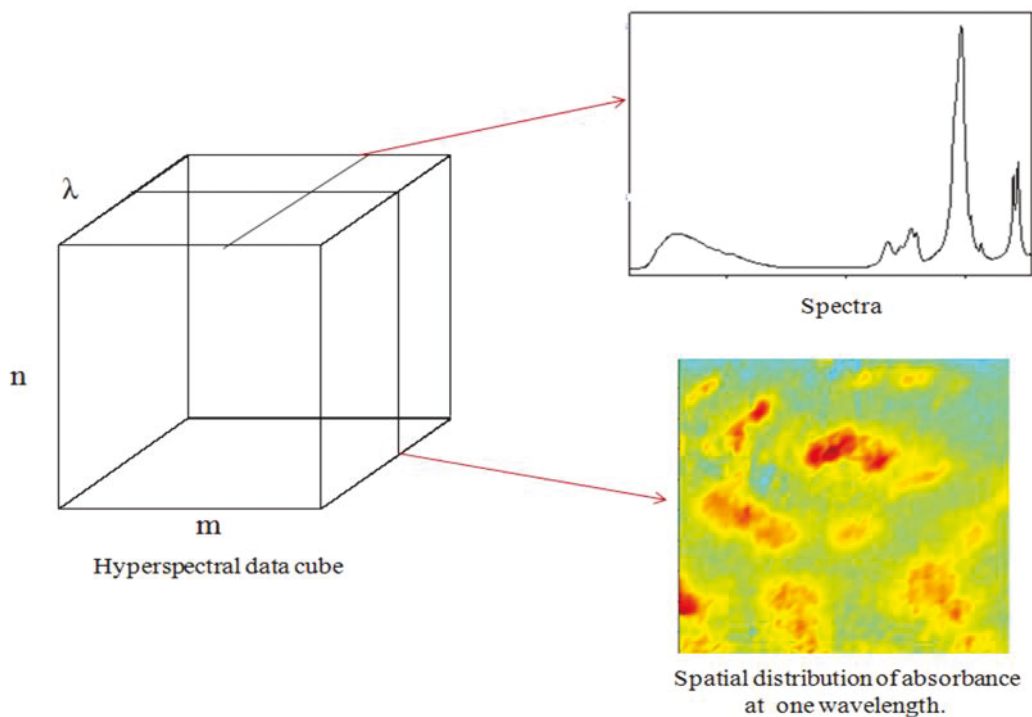


Fig. 3.6: Data cube generated during one chemical imaging experiment. Two dimensions depict the spatial distribution of the compounds, the third one, the spectral dimension, allows their identification.

They are three techniques to generate a hyperspectral cube as depicted in figure 3. 6. The first strategy is point mapping (Figure 3.6 (a)) and until years 2000 this technique was the most widespread one. It consists of a spectrometer combined with a microscope and a moving stage [156]. The user defines a regular grid of spatial positions above the surface of the sample. A spectrum is measured at one position, the sample moves to the next measurement point of the grid and another spectrum is registered. The process is iterative for all the positions in the area which defines the image. Today, nearly every constructors set up the possibility of using point mapping for microscopic spectroscopy.

The second method is called “line imaging” (Figure 3.6 (b)). A detector allows acquiring simultaneously one spatial dimension and the spectral dimension [157]. As with point mapping, the system acquires spectra according to predefined spatial positions and the line is moved right to left and/or up to down to cover the whole surface. A second configuration of line imaging experimental set up exists for process control. The detector is fixed and the samples, placed on a conveyor belt, are moving.

The third method uses Focal Plane Array (FPA) or Charge-Coupled Device (CCD) detectors (Figure 3.6 (c)) [158-159]. FPA are composed of several thousands of detector elements forming a matrix of pixels. They are optical detectors placed at the focal plane of spectrometers. It allows the acquisition of thousands of spectra at the same time [160]. The popularity of such systems has increased these last 10 years and several systems are now available.

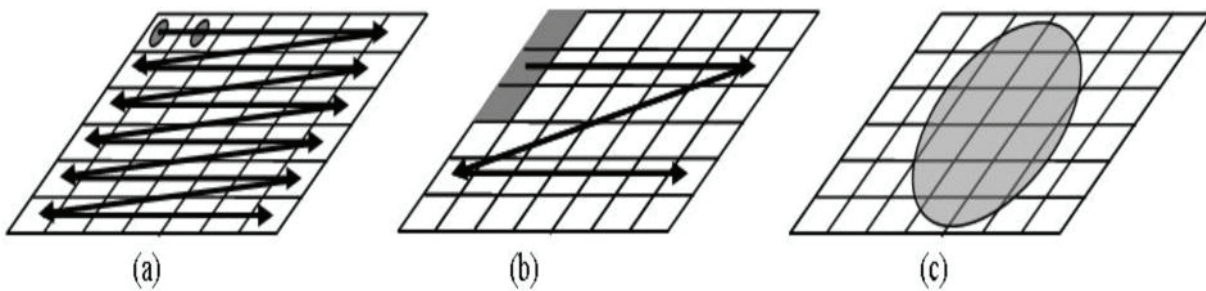


Fig 3.7: Three approaches exist to register one hyperspectral imaging data cube: (a) point mapping, (b) line mapping and (c) widefield approach, the latter one being the fastest one [158].

3.8 Spectral analysis

Both, Raman and infrared spectroscopies provide information that is rich in fine spectral features, thereby providing excellent structural information and the possibility to differentiate among image constituents based on their distinct ‘ spectral fingerprints ’. It is for this reason that resolution techniques, aimed at recovering the real pure spectra and distribution maps of the chemical components from a raw image, might benefit from the highest spectral definitions of Raman and infrared spectroscopic images. Mathematical algorithms usually are used to analyze the chemical imaging or to single point spectroscopy. These algorithms are applied to show the physical and chemical effects and characterize quantitative or qualitative contributions of individual sample components. As common in hard tissue, the spectral analysis technique is the univariate analysis (such as band intensities, intensity ratios and bandwidths). On the other hand we used the multivariate algorithm to study the transition area (DEJ).

3.8.1 Univariate analysis

For the interpretation of spectra, converting the spectra to absorbance display mode provides us the opportunity to read the absorbance value and relate it to the relative content of the biopolymers of interest. Peak intensity ratio calculation and mapping analysis of certain chemical functional groups or ratios are also common methods to deal with IR and Raman spectroscopic data [161-162]. An earlier study applied this analysis method and found that yellow- and brown-seed canola showed different characteristic peak intensities and chemical functional groups ratios, which indicated microstructure differences between canola varieties [163]. Univariate analysis explores each variable in a data set, separately. It looks at the range of value, as well as the central tendency of the value. It describes each variable on its own.

3.8.2 Multivariate analysis

Multivariate analysis takes into account all the spectral information contained in the data cube. As shown in Figure 3.7 several sub-divisions may be drawn up. On one hand there are the factorial methods which aim at decreasing the dimension by using an underlying multivariate distribution [164-165]. The measured data are modeled such as to be a linear combination of the

factors plus a term of noise. On the other hand, there are clustering techniques which aim at classifying the spectra into different groups of same features. Clustering techniques may be applied to the full spectra but also after factor analysis, in the reduced space [166].

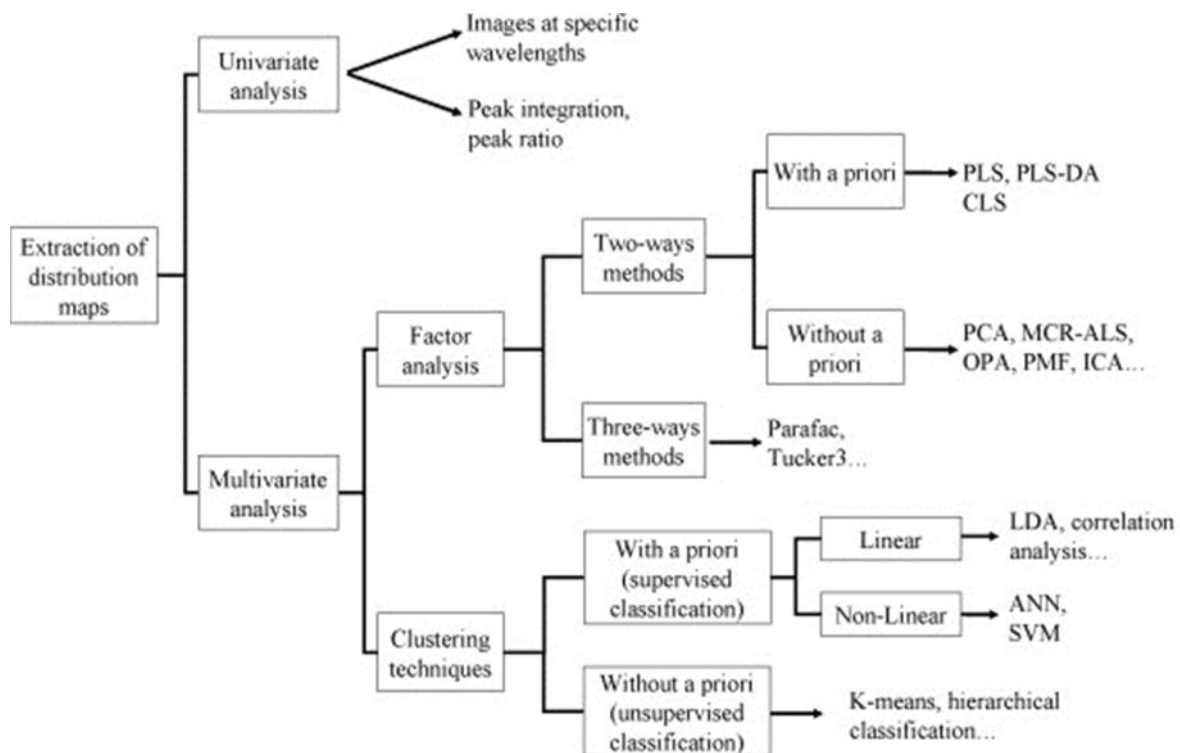


Fig. 3.8: Classification of methods for extracting distribution maps and some examples.

Hierarchical cluster analysis (HCA) and principal component analysis (PCA) are commonly applied in statistical data analysis [167]. Hierarchical cluster analysis is used to sort objectives according to a defined similarity [168]. HCA builds the cluster by combining the objectives according to the distance measurement. The objectives are treated and linked into larger groups by calculating criterion distance step by step. The previously established clusters are progressively merged into larger groups. Eventually, these algorithms form a hierarchical dendrogram to express the possible structure of the data [168-170]. The dendrogram, appearing as a tree structure, can be generated to visibly present the results. PCA is a widely used statistical technique to compress and de-noise large data sets. The principal components

represent the best set of axes that can be used to view the data. The data are uncorrelated in the new set of axes as opposed to the old one. This shows an important characteristic of the principal components in that they form a basis for the data. Therefore, it is easy to make out patterns in the data. Further, the principal components of each data are arranged in the decreasing order of their contribution to the variance.

K-means clustering is a method of cluster analysis which aims to partition n observations into k clusters in which each observation belongs to the cluster with the nearest mean. It is similar to the expectation-maximization algorithm for mixtures of Gaussians in that they both attempt to find the centers of natural clusters in the data as well as in the iterative refinement approach employed by both algorithms. On the other hand, VCA algorithm iteratively projects the spectral vectors onto a direction orthogonal to the subspace spanned by the endmembers already determined. The new endmember signature corresponds to the extreme of the projection, thus the name vertex component analysis. The algorithm iterates until all endmembers are exhausted. VCA is a fully automatic algorithm and works with or without dimensionality reduction [171].

3.9 Curve – fitting

Curve-fitting is a mathematical modeling tool to adjust the band parameters to obtain the best agreement to experimental data. The following equation is tried to be minimized as result of curve-fitting, where the $y(v_i)$ is the experimental data as a function of variable v , N is the total number of data and $f(v_i; a)$ is the fitted data.

$$\sum_{i=1}^N (y(v_i) - f(v_i; a))^2$$

There are several parameters to find the best-fit parameters by using different method, such as, Newton-Rapson method, the Steepest Descent method, the Levenberg-Maequard method, and Nelder-Mead simplex method [172-173]. Curve- fitting requires an initial guess for the parameters which will eventually be the main determinant for the best fit. Those parameters can be counted as the position, width, area and band characteristics of each band, where the total

number of the bands will be additional parameters by itself. Usually a baseline with one or more parameters is included in the model or baseline correction is performed before curve-fitting. By means of such a mathematical approach, curve-fitting enables the determination of the relative sub-volume that are superposed a main band. The process is applicable to the inorganic and organic spectra, (like phosphate and collagen spectra).

The amide I profile has been deconvoluted by applying the Lorentzian shape function [175]. The resolution enhancement factor γ , representing the full width at half height (FWHH) of the widest resolvable peak as shown in the following equation:

$$f(x) = e^{2\pi\gamma x}$$

Where x is the data array [176]. This function is multiplied with the Fourier transformed trace and then reverse Fourier yielding the deconvoluted trace as demonstrated in figure 3.8. Deconvolution aims to increase the apparent noise sample data; there are some advantages to be gained by simultaneously applying a low Bessel smoothing filter, especially when taking a second derivative of the deconvoluted data.

3.9.1 Second derivative spectra

Susi and Byler, 1986, recommended that the derivative spectra are one of the best methods to remove the baseline effects and resolution enhancement [175]. This method has become common applying to correct baseline effects in spectra for the purpose of creating robust calibration models. The 1st derivative of a spectrum is simply a measurement of the slope of the spectral curve at every point. The slope of the curve is not affected by baseline offsets in the spectrum. The 2nd derivative is a measurement of the change in the slope of the curve. There are many ways to calculate derivatives. One of the easiest is by using the method of simple differences based on this equation

$$A_i = A_{i+1} - A_i$$

But this way is not always used to calculate real derivatives. In fact, since it attempts to estimate the derivative from the between-point differences, it just succeeds in enhancing the noise in the spectrum. The Savitzky-Golay method and Gap method are much better algorithms to calculate

derivatives [177]. Both of these algorithms use information from localized segment of the spectrum to calculate the derivatives at a particular wavelength rather than the difference between adjacent data point.

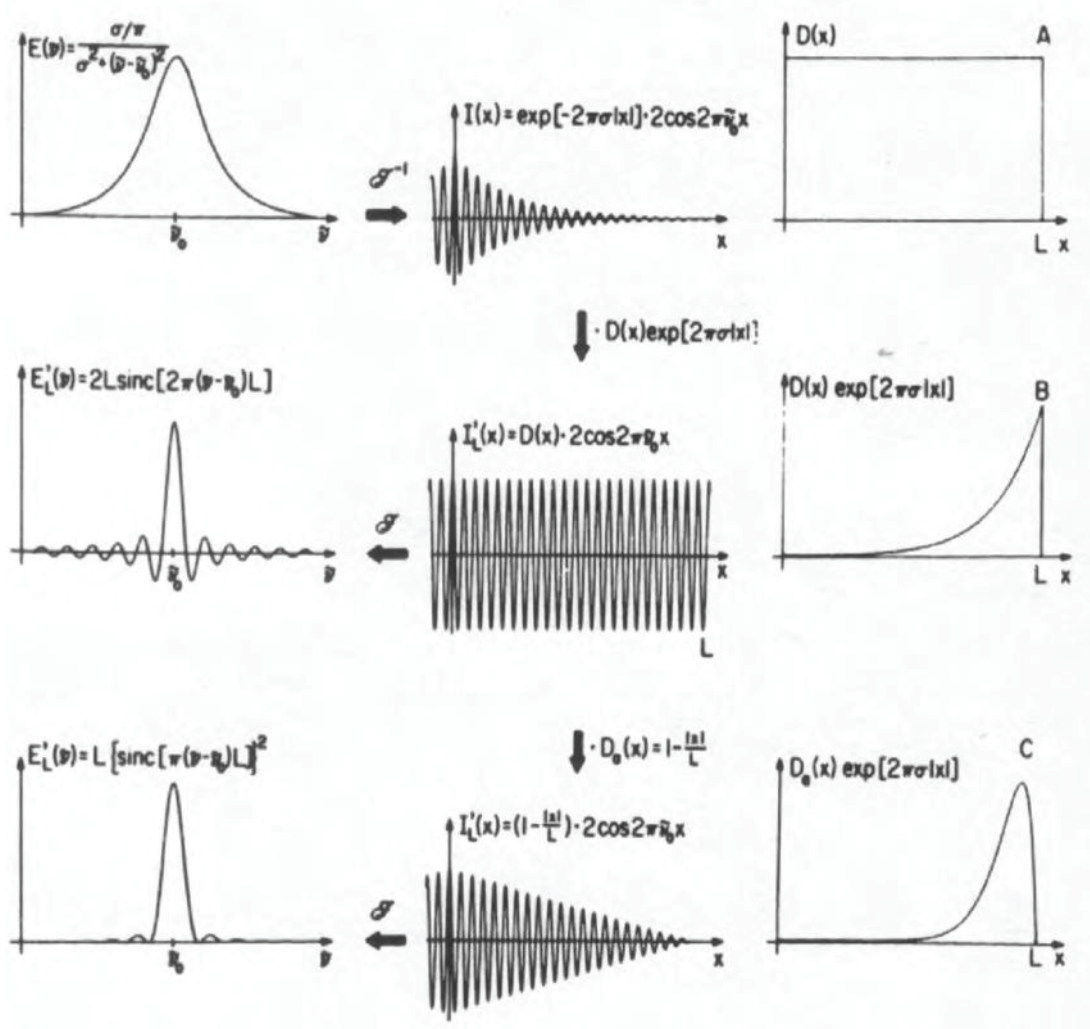


Fig 3.9: Fourier self deconvolution in details starting with a Lorentz line [176].

3.9.2 Gaussian curve fitting

In curve fitting we have raw data and a function with unknown coefficients. We want to find values for the coefficients such that the function matches the raw data as well as possible.

The “best” values of the coefficients are the ones that minimize the value of Chi-square. Chi-square is defined as

$$\sum_i \left(\frac{y - y_i}{\sigma_i} \right)^2$$

Where y is a fitted value for a given point, y_i is the measured data value for the point and σ_i is an estimate of the standard deviation for y_i .

Peak fitting can be extremely useful for determining the the exact peak position, widths, height and areas of a set overlapping peak (figure 3.9).

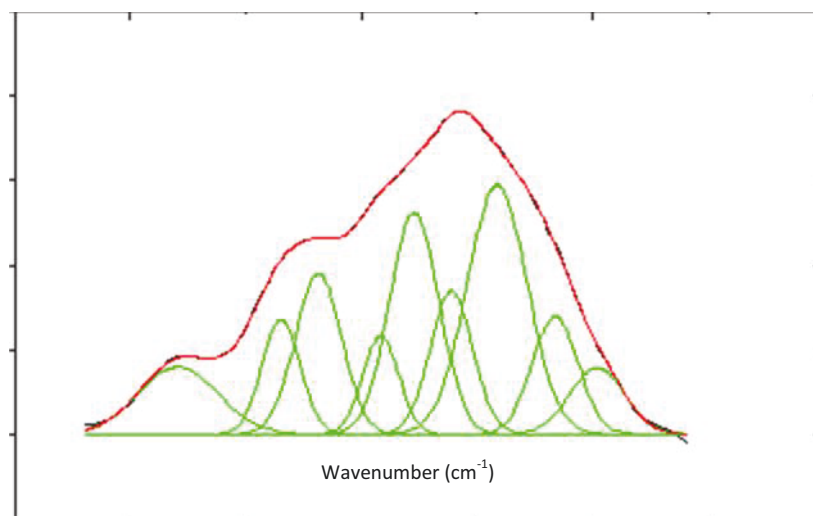


Fig. 3.10: Gaussian curve-fitting of a sample spectrum: original spectrum (black), fitted trace (red) and calculated bands (green).

Calculating the exact positions and numbers of peaks except, in an indirect fashion by examining the residual error of the fit for a different number of fitted peaks. Curve fitting is an iterative process and may need to be performed many times to achieve good results. The first iteration is used as the initial guesses for the second iteration and so forth.

3.10 Materials

3.10.1 Dental materials

In this investigation we have used the following samples of teeth from different places and ages. 14 non-cariou, human teeth were collected under informal consent from patient children and adults in Hacetape Hospital-Turkey. 10 non-cariou, human teeth (children and adults) were provided from Dentistry College, University Hospital Jena, Germany. 25 ancient samples (1000-2000 years), not affected by cariou or sediment, were collected from archaeological site at south Jordan so called Khirbet adh-Dharih.

In modern teeth, soft tissue remnants were quickly removed from the root surfaces, after which the teeth were stored in an aqueous solution of 0.5% chloramine-T at 4 °C before use. The teeth were transferred to room temperature 24 h before experimental procedures. The Turkish specimens were stored in an aqueous solution of 4% formalin to inhibit the microbial growth until used. Specimens were embedded in autopolymerizing polymethylmethacrylate (PMMA). Saw, stainless steel with galvanic diamond coating, grain size 120 micron and 4 cm diameter, (KOMET, GERMANY) was used to generate a 1-2 mm thick slice. The specimens were manually polished before the measurements have done. On the hand, German samples were prepared for this investigation, as longitudinal oro-vestibular sections through the central part of the teeth (1 mm in thickness). The teeth were fastened to a cylindrical carrier using autopolymerizing resin (Kallocryl CPGM rot, SPEIKO[®] - Dr. Speier GmbH Münster, Germany) and adjusting the section plane parallel to the sawing blade. Afterwards, the teeth were completely covered with resin. The sections were made with constant water-cooling using the low-speed saw microtome LEITZ-1600 (Leica Mikrosysteme Vertrieb GmbH Bensheim, Germany). The archaeological teeth samples also have been cut to generate slices with 1-2 mm thickness and were polished manually. We could distinguish them (adult or children) by the size of tooth.

3.10.2 Sample analysis

a) ATR-FTIR spectroscopy and imaging

A FTIR imaging system (Figure 3.10) combining a spectrometer (model 670, Varian, USA) with microscope 64×64 focal plane array detector (model 620, Varian) was used to acquire the spectra in the interval 900-4000 cm^{-1} at a spectral resolution of 4 cm^{-1} . Single spectra were carried out by Mercury Cadmium Telluride (MCT) detector from 750 to 4000 cm^{-1} . The microscope chamber was in a home build box and purged by dry air to reduce spectral contributions from water vapor. Analysis were conducted in reflection mode by attenuated total reflection (ATR) based on a Germanium (Ge) crystal and 64 scans were collected for each point.



Fig. 3.11: Varian model 670, equipped with a microscope model 620, of a FTIR microscopic imaging.

b) Raman spectroscopic imaging

Raman spectra and images were collected by using a Raman microspectrometer (Kaiser Optical System, AnnArbor, MI, USA) excited by a 785nm laser of single mode diode laser (Toptica, Germany) as shown in figure 3.11. Operating at excitation power of 100 mW with a 100x/NA 0.9 objective (Nikon, Japan). The scattered Raman signal was detected on a Peltier-cooled, back-illuminated, deep-depletion CCD chip (Andor, Ireland). Spectra were obtained over the spectral region of 200 to 3450 cm^{-1} at spectral resolution of 4 cm^{-1} with a step size of 1 μm . All spectra were background-corrected for dark counts, corrected for cosmic spikes, intensity-calibrated and wavenumber-calibrated by the Holograms software (Kaiser).

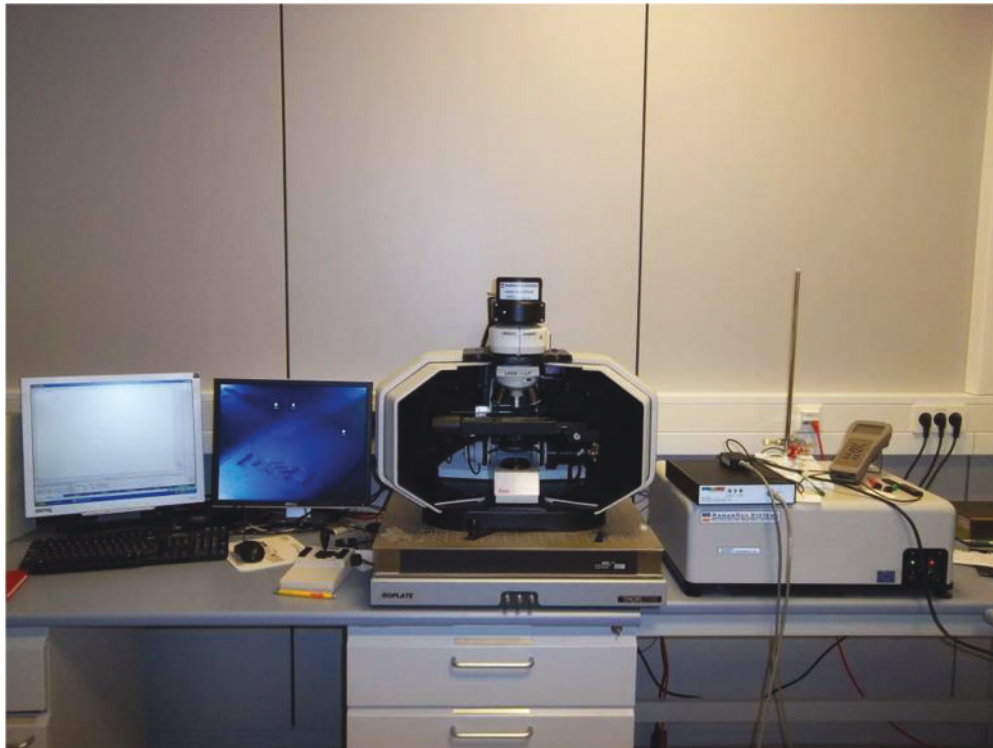


Fig. 3.12: Raman microspectrometer (Kaiser Optical System, AnnArbor, MI, USA)

3.10.3 Spectral data analysis

Mathematical algorithms usually were used to analyze the chemical image or the single point spectra. These algorithms are applied to show the physical and chemical effects and characterize quantitative or qualitative contributions of individual sample components. As common in hard tissue, the spectral analysis technique is based on the univariate analysis (such as band intensities, intensity ratios and bandwidths), as well as the multivariate analysis was used to unveil some features of the transition area (DEJ). IR and Raman spectra of human dentin and enamel teeth from different dataset were cut over the region 750 to 1800 cm^{-1} and 800-1800 cm^{-1} respectively. All data set were imported into (Cytospec Inc, USA) (www.cytospec.com) and mapping imaging spectra were adjusted using polynomial baseline correction.

Origin Pro 8.5 (Originlab, USA) (www.originlab.com) was used to analyze the acquired IR and Raman spectra data to reveal the subbands which have been used in this study by curve-fitting process of phosphate IR profile under the spectral region from 900 to 1200 cm^{-1} , amide I envelope of IR and Raman spectral region of 1590 – 1720 cm^{-1} , and the weak shoulder of 850 to 900 cm^{-1} of carbonate CO_3^{2-} ν_1 . The Gaussian shape was considered and a linear baseline was assumed. Also we imported Raman spectra into Origin Pro Lab to determine the Full-Width at Half-Maximum (FWHM) of phosphate band at 960 cm^{-1} .

3.10.4 Tooth slice

Figure 3.12 represents photographs of teeth slices illustrating the enamel, dentin and the transition area from the enamel to the dentin (DEJ) of Turkish, German and Jordanian teeth samples. The tooth was embedded in resin before sawing. Regions of interest were selected which represent enamel and dentin as illustrated on graphs. Where the black squares represent the positions of imaging measurements of pure enamel or dentin, and the red ones are the transition area of the dentin enamel junction positions.

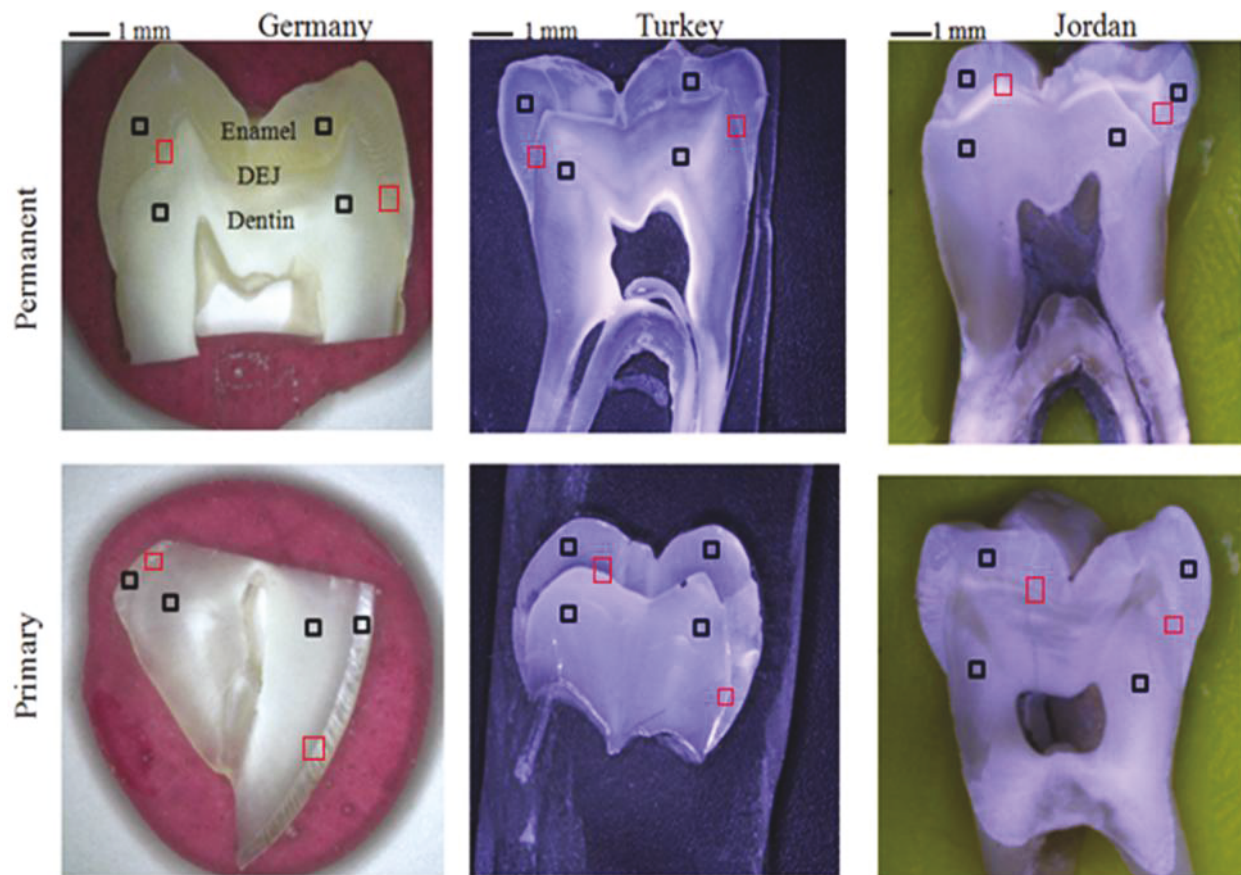


Fig. 3.13: Representative photograph of teeth slices from permanent and primary teeth illustrating the enamel and dentin. Boxes indicate where the spectral maps were obtained.

Chapter 4

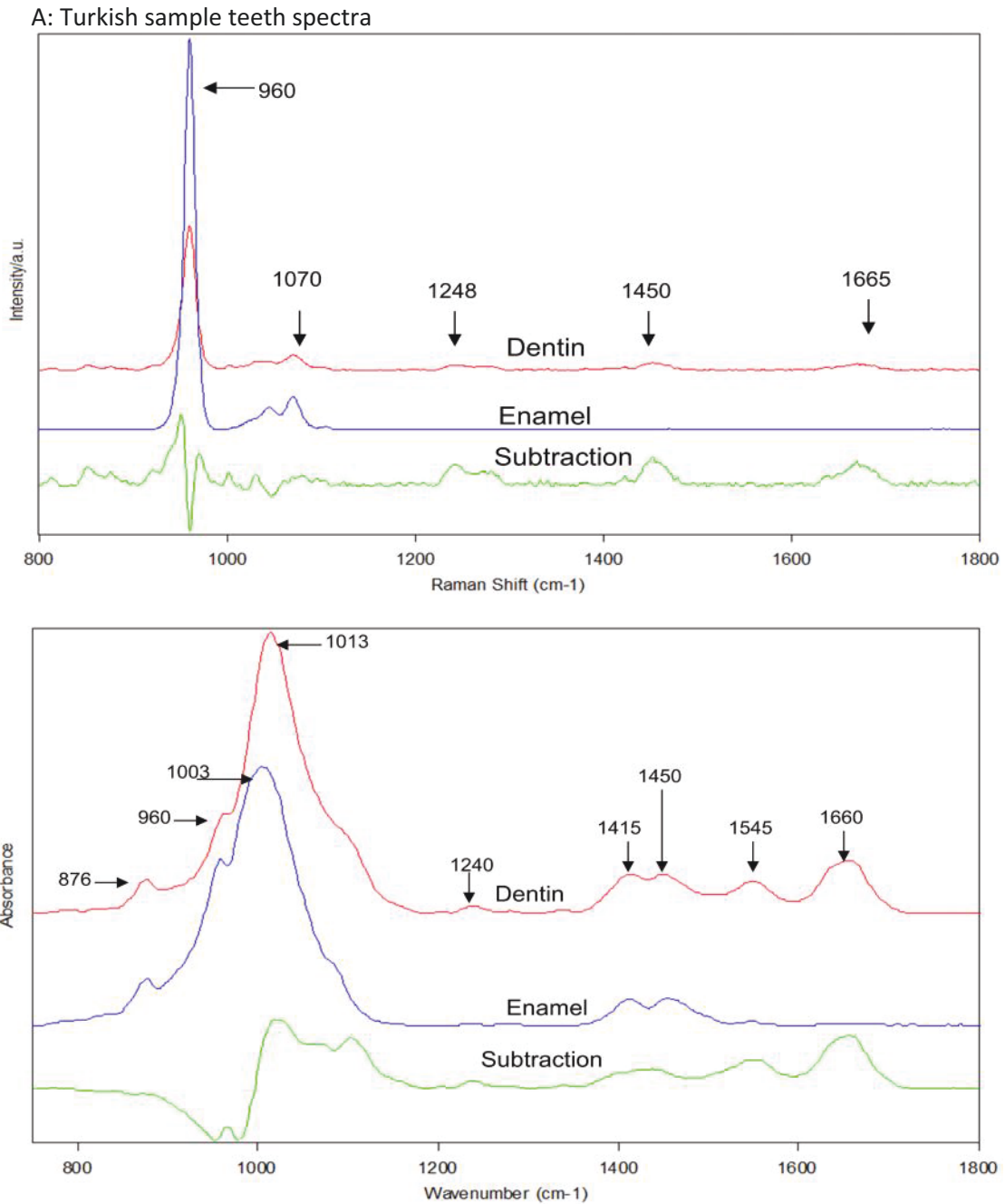
Result and discussion

Over the last 20 years, the superior chemical specificity and spatial resolution afforded by microRaman and FTIR spectroscopies have been utilized increasingly in a large number of applications. However, it has failed to meet its full potential for a wide range of sample analyses because of the relatively slow speed of spatial mapping and imaging technologies. New developments in technology have enabled the potential of Raman and FTIR spectroscopies to elucidate chemical, structural, and distribution information. (Refer to chap. 3 section 3.9.2). In this chapter we explain the imaging parameters of IR & Raman spectroscopies, such as, mineral to matrix ratio, carbonate to phosphate ratio, cross-links and crystallinity.

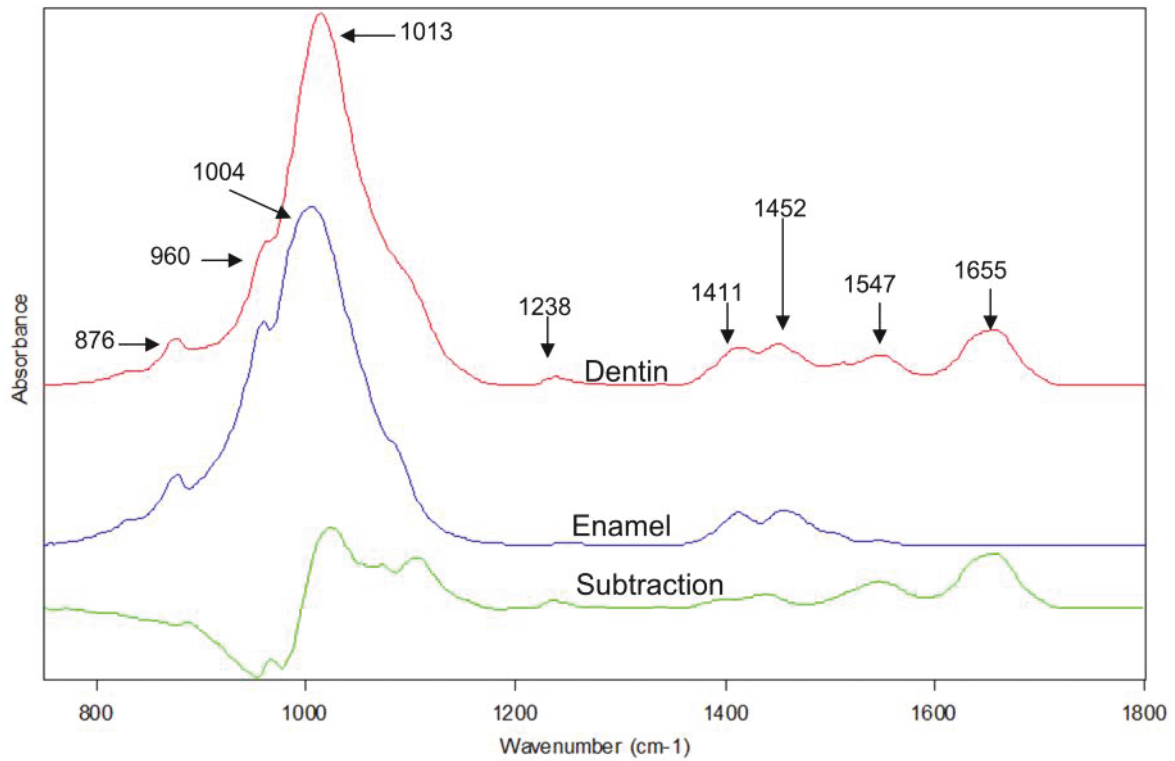
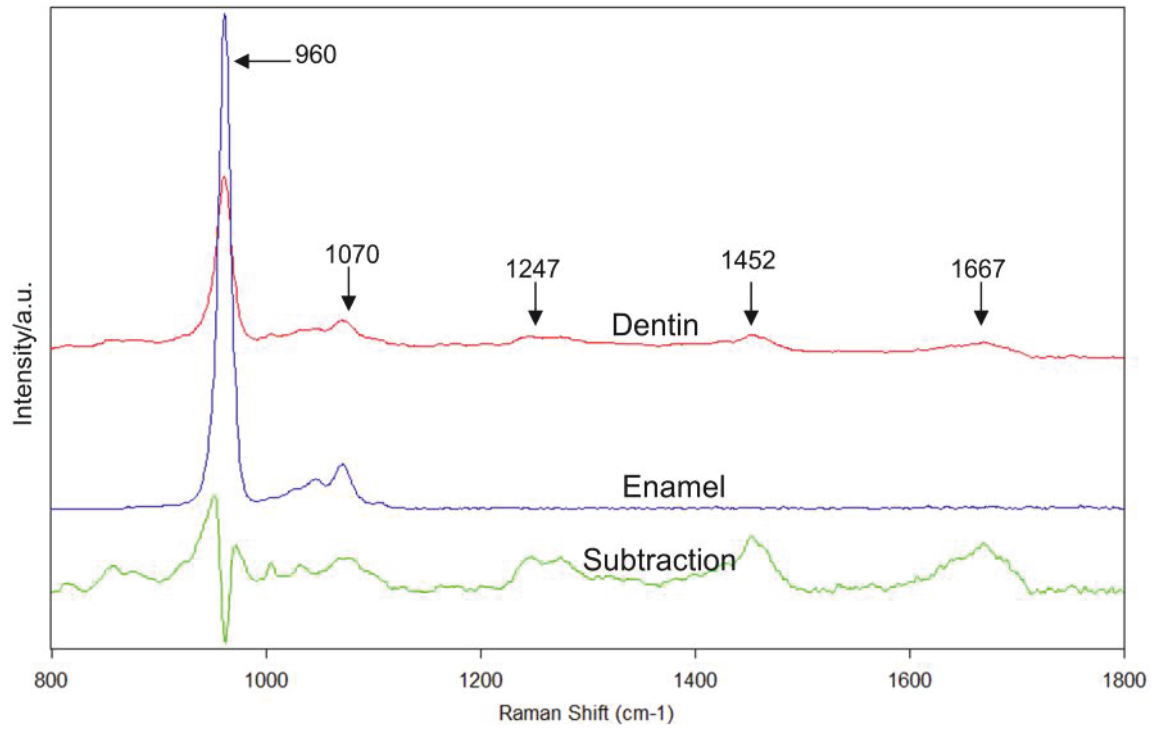
4.1 IR and Raman teeth Spectra

Figure 4.1A, B & C represents the typical IR (750-1800 cm^{-1}) and Raman spectra (800-1800 cm^{-1}) of human dentin and enamel in order to the provided place of samples. The difference spectrum of dentin minus enamel was calculated to better visualize the organic bands. The IR spectra region from 900-1200 cm^{-1} related to mineral contents and 1200-1800 cm^{-1} region based on protein, which is collagen type I. The significant shift of $10 \pm 2 \text{ cm}^{-1}$ clearly appeared on all IR spectra of dentin and enamel from permanent and primary teeth spectra. These significant shifts might be due to the different contents of inorganic materials from the enamel to the dentin. The wave number shifted also could be related to the mineralized tissue stress. The IR intense peak at 1013, 1003 cm^{-1} for the dentin and enamel respectively, assigned to be a component of the $\nu_1\nu_3$ phosphate envelope in poorly crystalline apatites attributed to HPO_4^{-2} . In Raman spectra of the human dentin and enamel, the bands associated with inorganic component (mineral) appeared in the spectral range from 900 to 1100 cm^{-1} , including ν_1 and ν_3 vibration bands. The organic components (collagen) appeared in the spectral region of 1200 to 1720 cm^{-1} . Moreover, the most intense peak on Raman spectra is the symmetric stretch vibration of PO_4^{-2} at 960 cm^{-1} , whereas this peak appears as a shoulder weak and its width broader on IR spectra. The difference spectra are more similar in modern teeth (German and Turkish Teeth) than the archaeological ones (Jordanian teeth). For example, Amide III at 1240 cm^{-1} in modern samples clearly appeared, while it is absent in the archaeological ones, this difference is due to the degradation process of

organic components during the time decay on that samples. Also the archaeological difference spectrum showed an intense peak at 1048 cm^{-1} relevant to ν_3 of PO_4^{2-} . Another difference between Raman and IR teeth spectra is amide II at 1455 cm^{-1} which does not appear in Raman scattering. The organic and inorganic peaks are listed in Chap. 2 table 2.1.



B: German sample teeth spectra



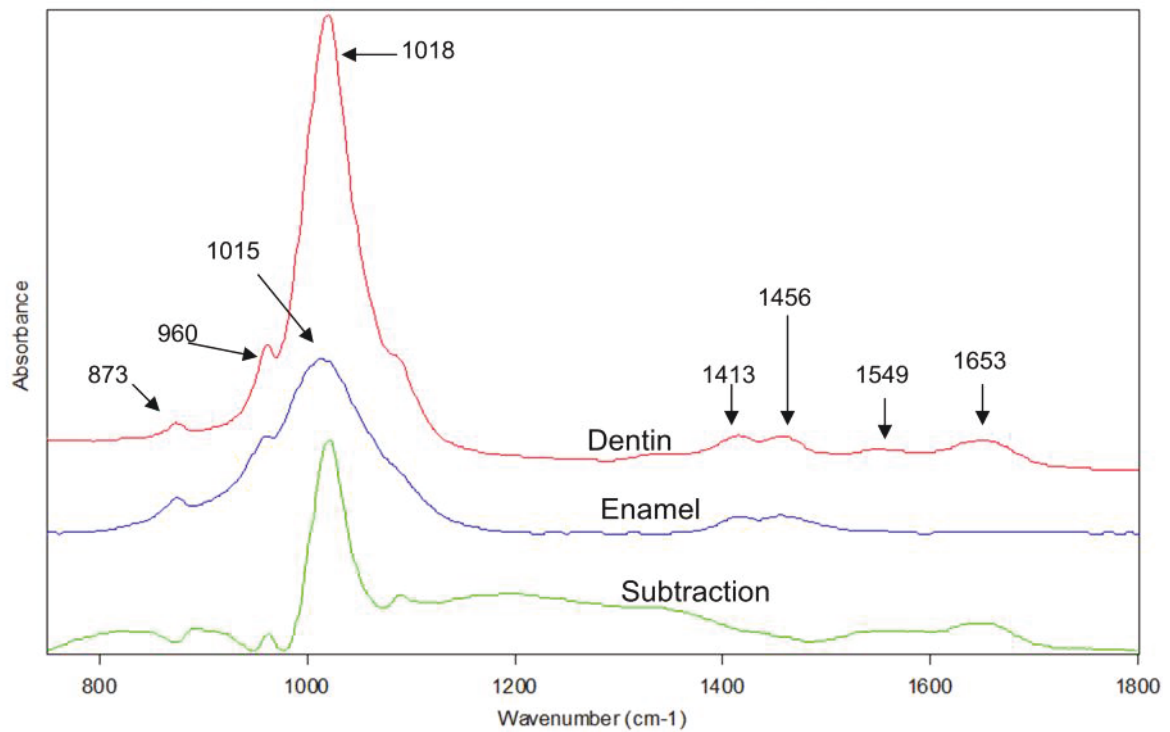
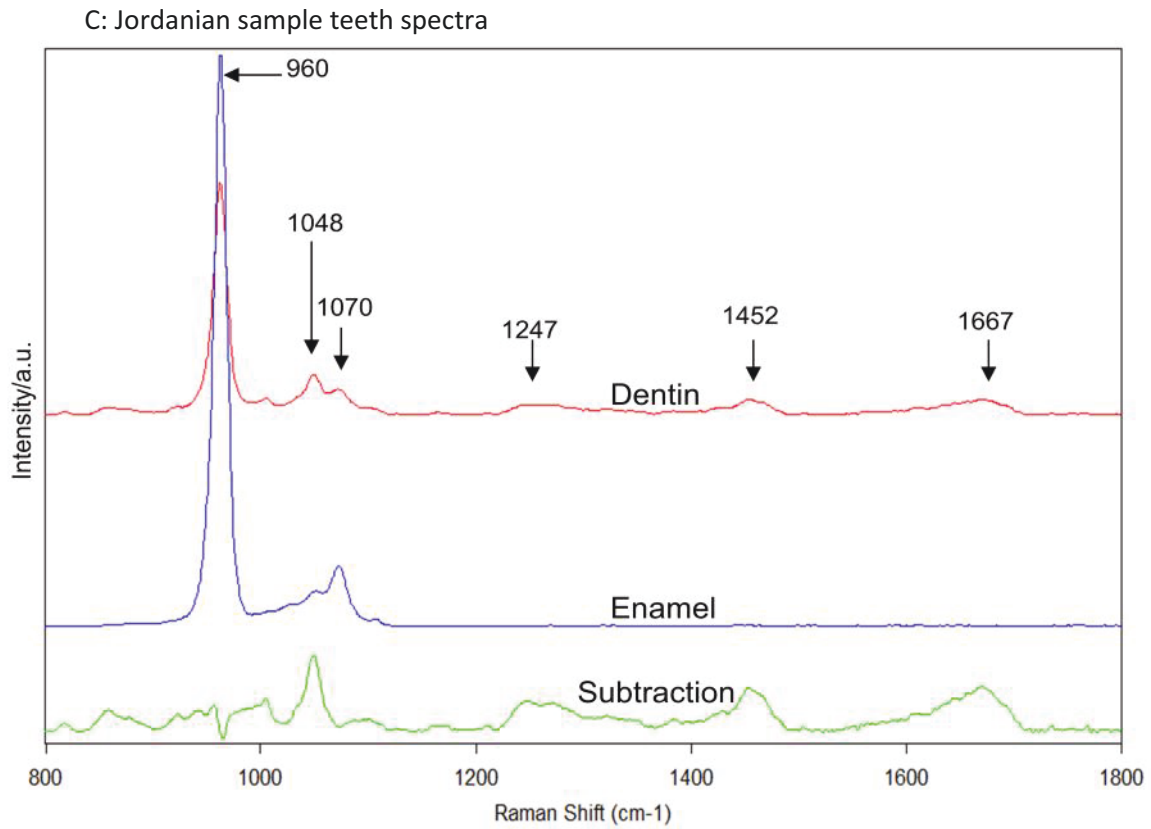


Fig. 4.1: representative the typical infrared spectra (750-1800 cm⁻¹) and Raman spectra (800-1800 cm⁻¹) of permanent dentin and enamel with difference spectra (dentin – enamel) from Turkish (A), German(B) and Jordanian (C) samples teeth.

4.2 Curve-fitting results

Figure 4.2.1 shows the ATR-FTIR curve-fitting with Gaussian distribution of the $\nu_1\nu_3$ of phosphate. We used a Gaussian shape and a linear baseline was assumed. Peak finding based on the second derivative method was applied to find out the subbands, the peak filtering depend on peak height with no smooth. The $\nu_1\nu_3$ of phosphate was fitted under the area 900 to 200 cm^{-1} with five components at ($960, 1020, 1030, 1055, 1110\text{ cm}^{-1}$), where 960 cm^{-1} associated to the ν_1 of PO_4^{-2} , 1020 cm^{-1} has been assigned to HPO_4^{-2} in poorly crystalline apatite, 1030 cm^{-1} peak was assigned to apatitic phosphate, 1055 cm^{-1} is related to ν_3 of PO_4^{-2} , and 1110 cm^{-1} peak is present in nanocrystalline apatites and it has been associated to non-apatitic phosphate or HPO_4 in poorly crystalline apatite.

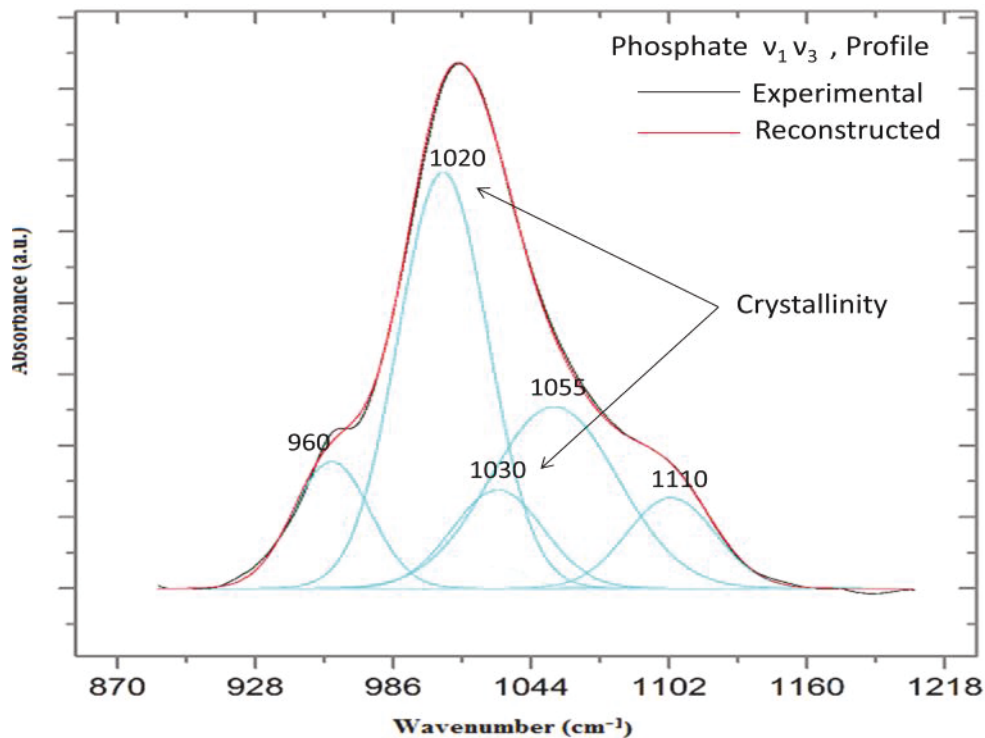


Fig. 4.2.1: Curve-fitting analysis of $\nu_1\nu_3$ phosphate of IR spectra.

Figure 4.2.2 is shown the fitting analysis of amide I profile in IR spectrum (A) and in Raman spectrum (B). In IR spectrum, it contains six major components. They are located at 1610 cm^{-1} (aromatic rings), 1630 cm^{-1} (β -sheets), 1645 cm^{-1} (random coils), 1660 cm^{-1} (α -helix), 1678 cm^{-1} (β -sheets) and 1690 cm^{-1} (turns). On the other hand, curve-fitting analysis of the same region of amide I profile in Raman spectra identified nine components (aromatic rings, two times β -sheets, random coils, α -helix, turns and three components at 1654, 1685 and 1700 cm^{-1}). Collagen cross links provide the fibrillar collagen matrices with properties like tensile strength and viscoelasticity. The relative peak height at 1660 to 1690 cm^{-1} was used to analyze the crosslinks [107, 115]

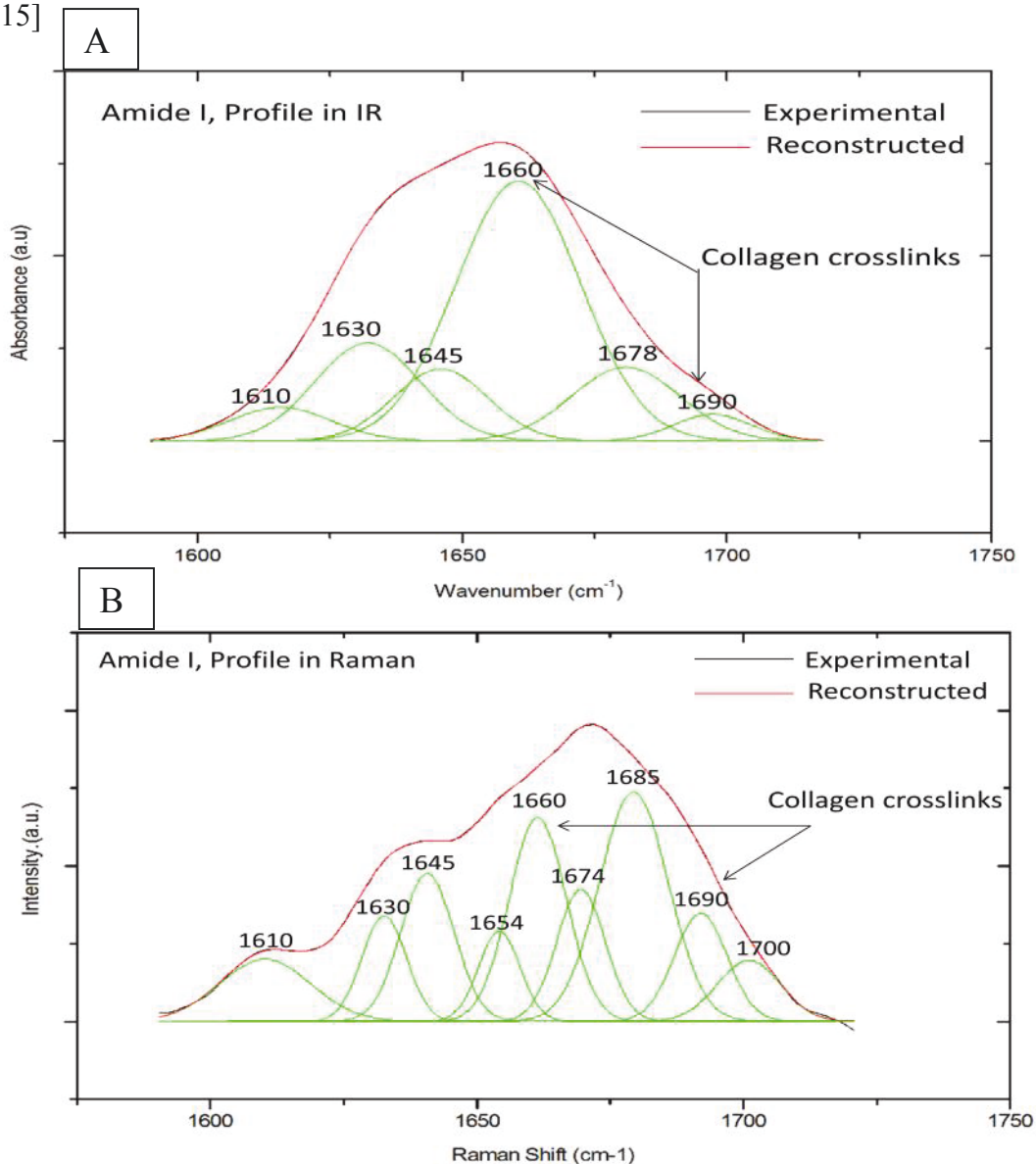


Fig. 4.2.2: Curve-fitting analysis of amide I profile of IR (A) and Raman (B) dentin spectra.

The carbonate spectral area ν_2 of CO_3^{2-} at 876 cm^{-1} from 850 to 900 cm^{-1} also was subjected to the curve-fitting process of the permanent and primary teeth spectra to study the carbonate substitution in the dental tissues. Figure 4.1.3 shows the curve-fitting analysis of the carbonate IR area in the permanent teeth spectra (C) and primary ones (D). The data revealed that permanent enamel and dentin spectra contained two components, while three components in primary enamel and dentin spectra. The peaks were assigned to ν_2 of CO_3^{2-} (A2-type carbonate) at 860 cm^{-1} , the peak at 871 cm^{-1} related to ν_2 of CO_3^{2-} (B-type carbonate) and the third peak at 878 cm^{-1} is assigned to ν_2 of CO_3^{2-} (A-type carbonate) [178]. It is the first time (not previously observed for my knowledge) that A2-type carbonate has been reported in living dental tissue in primary teeth of enamel and dentin IR spectra.

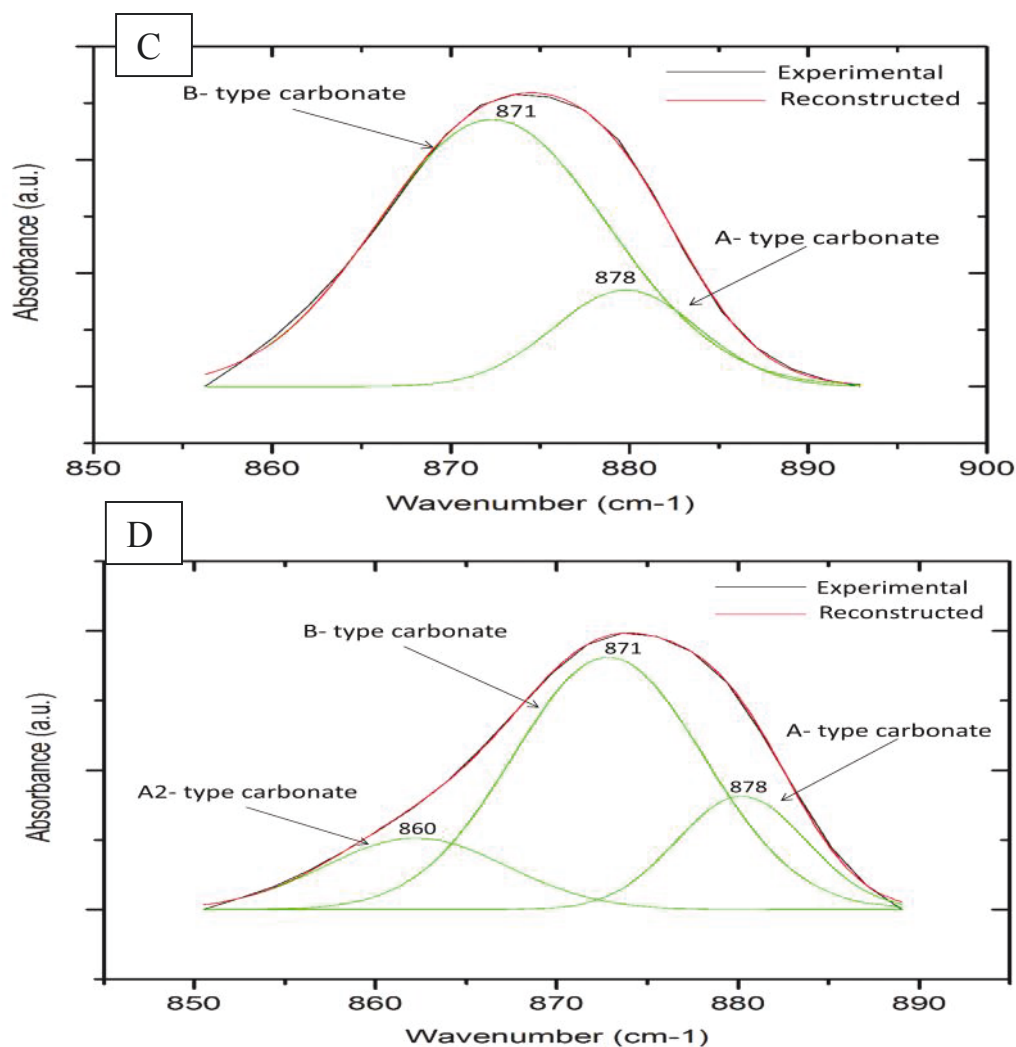


Fig. 4.2.3: Curve-fitting analysis of carbonate IR permanent (C) and Raman (D) teeth spectra.

4.3 Carbonate substitution on the apatite structure

The hydroxylapatite lattice in living organism is substituted by different cations to assist maintaining a normal metabolism. Carbonate substitution on the biological performance of HAP affects important on its properties like solubility and reactivity. In this study carbonate contents were studied from the area of the CO_3^{2-} components at 866 cm^{-1} of A, A2 (hydroxyl site, at 878cm^{-1} , 860cm^{-1}) and B (phosphate site, at 871cm^{-1}), in human dental tissues of permanent and primary teeth. Compared to the human dentin of permanent teeth spectra the best fitting of carbonate area in primary human teeth spectra was with three components, the third component at 860cm^{-1} was assigned to A2-type carbonate [179] or the labile carbonate . The absence of third component of A2-type carbonate from permanent teeth might be related to the mineral maturity (crystallinity). It is well known that the crystallinity increases when crystal are larger and more perfect (i.e., less substitution). The hydroxyapatite crystals in teeth are imperfect due to other anions and cations, especially magnesium, chloride, carbonate, and fluoride ions. Table 3 is shown the intensity ratio of A, A2 & B-type carbonate to the ν_1 mode of PO_4 at 960 cm^{-1} , and the amount of each component is given in percentage terms, by dividing the area of the one carbonate band component by the area of the sum of all carbonate components.

	tissue	B-type/P-O	A-type/P-O	A2-type/P-O	I_B/I_{A2-A}	Area B%	Area A%	Area A2%
Turkey	Per.dentin	1.2 ± 0.09	0.44 ± 0.03	-----	2.7	$84.4 \pm 4.5\%$	$14.6 \pm 4.6\%$	-----
	Per.enamel	0.75 ± 0.12	0.32 ± 0.01	-----	2.3	$74.8 \pm 5\%$	$25.2 \pm 5\%$	-----
	Pri.dentin	1.3 ± 0.3	0.61 ± 0.1	0.21 ± 0.06	1.6	$64.6 \pm 4\%$	$25.2 \pm 2.8\%$	$6.8 \pm 1.8\%$
	Pri.enamel	0.62 ± 0.6	0.36 ± 0.03	0.14 ± 0.01	1.24	$64.3 \pm 2.6\%$	$23.1 \pm 2.6\%$	$12.3 \pm 0.7\%$
Germany	Per.dentin	1.2 ± 0.2	0.71 ± 0.05	-----	1.7	$82 \pm 3.6\%$	$16.4 \pm 3.3\%$	-----
	Per.enamel	0.48 ± 0.3	0.47 ± 0.09	-----	1	$77.6 \pm 3\%$	$22.4 \pm 2.6\%$	-----
	Pri.dentin	1.5 ± 0.2	0.63 ± 0.02	0.37 ± 0.3	1.5	$69.4 \pm 3\%$	$20 \pm 3.2\%$	$10.3 \pm .8\%$
	Pri.enamel	0.8 ± 0.6	0.44 ± 0.02	0.22 ± 0.02	1.2	$60.3 \pm 3\%$	$25.6 \pm 2.8\%$	$14.1 \pm 0.5\%$

Table 3.1: Properties of IR subbands of A, A2 & B-type carbonate.

Due to our computation, the carbonate content of primary teeth (enamel and dentin) is higher than carbonate content in permanent teeth. The higher content in primary teeth might be one of several factors of faster carious growing in primary teeth compared to permanent teeth [180]. The intensity ratio of B-type to P-O was always higher compared to the intensity ratio of A-type to P-O in all dental tissues (enamel and dentin) from the permanent and primary teeth spectra of German and Turkish samples. In the permanent tissues the B to A-type relative carbonate content is approximately 2.7, 1.7 in the dentin and 2.3, 1 in the enamel of German and Turkish samples respectively. Whereas that value is 1.5 for the primary dentin and 1.2 in primary enamel by consideration of the A2-type carbonate, these values indicate that much more carbonate ions are placed on the phosphate site than on the hydroxyl site in the crystal structure of HA. The percentage area of B-type carbonate occupied larger area under the ν_2 of CO_3^{2-} profile, which could be considered as an indicator for its important role as a major substitution site in crystal structure of HA.

4.4 Mineral to matrix ratio

The mineral phase in mature teeth (dentin and enamel) represents the major part of its dry weight. The mineral in dentin is very similar to the bone mineral and it is an analog of the naturally occurring mineral hydroxyapatite, whose unit cell can be represented as $\text{Ca}_{10}(\text{PO}_4)_6(\text{OH})_2$ [179, 181]. On the other hand, there is presently some confusion surrounding the taxonomy and terminology of dentin extracellular matrix components, which partly arose from an earlier characterization of the matrix components based on biochemical purification from tissues and from the possible discrepancies in characterization of the matrix components between different species. However, little is known about the chemical nature of the organic matrix of enamel, although it presumably plays an essential part in the initiation and organization of the growth of hydroxyapatite crystals.

Figure (4.3, A, B) demonstrates the ATR-FTIR and Raman variation of the mineral-to-matrix ratio in the permanent and primary dentin of German and Turkish samples (A) and the archaeological samples (B) based on the integrated IR area of phosphate ($900\text{-}1200\text{cm}^{-1}$) to the IR area of amide I band ($1590\text{-}1720\text{cm}^{-1}$) and ($900\text{-}1000\text{cm}^{-1}$) to the area of amide I band for

Raman images. The mineral/matrix quantity is the average ratio constructed from IR image with $n = 4096$, the value of n is the number of the pixels/image that used in this computation. The mineral/matrix ratio is linearly related to the mineral content, or “ash weight” widely used as an index of mineral quantity [182]. Therefore, it is an indicator of the relative quantity of mineral in calcified tissue. It is evident from fig.4A & B that mineral quantity do not differ between the permanent and primary dentin. The mineral content in sound dentin (no plaque caries) of permanent and primary teeth could be independent of maturity. In comparison, the Turkish teeth samples showed the highest mineral contents inside the HA lattice, while the German teeth have lower mineral contents, even lower than the ancient (Jordanian) teeth samples, fig B, in consideration of the degradation process. These differences could be related to the weather of diet and the different environments in those places.

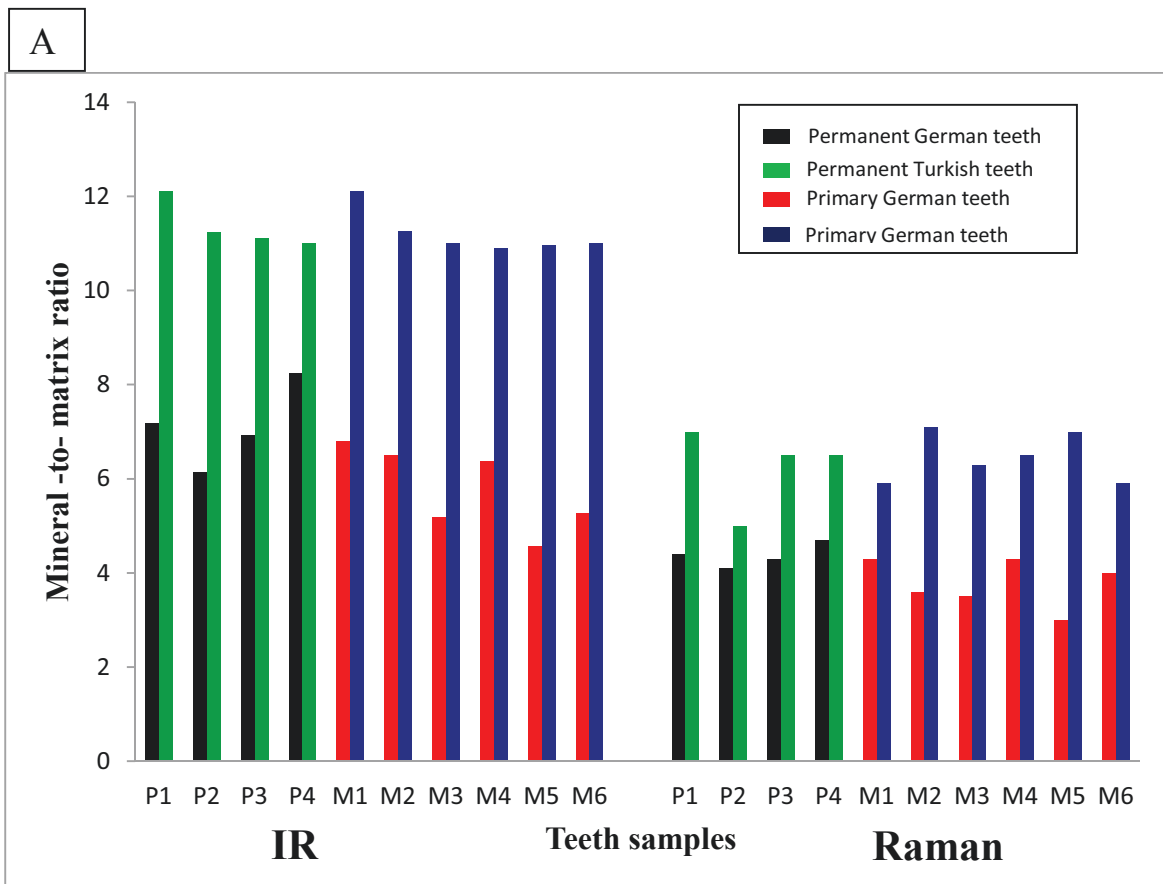


Fig. 4.3A: ATR-FTIR and Raman images variation of mineral-to-matrix ratio of permanent and primary (German & Turkish) teeth.

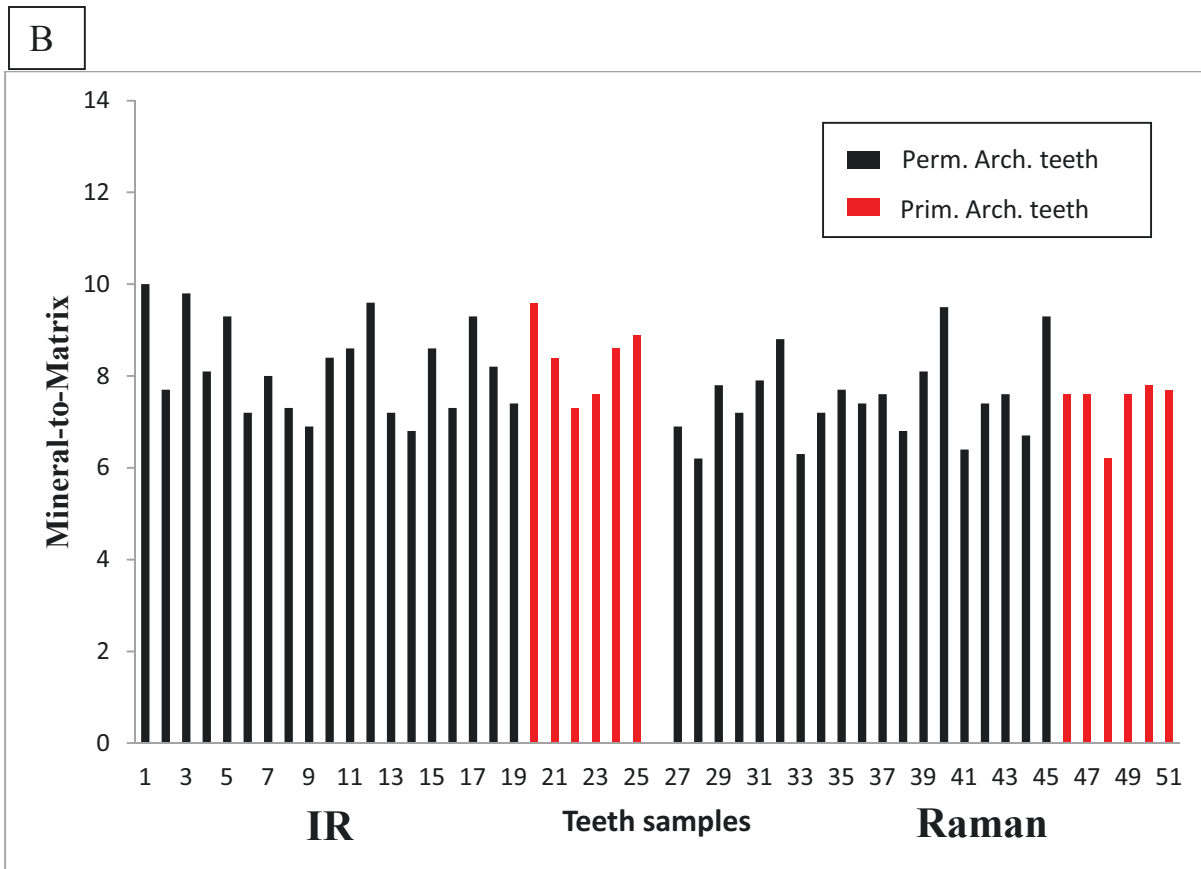


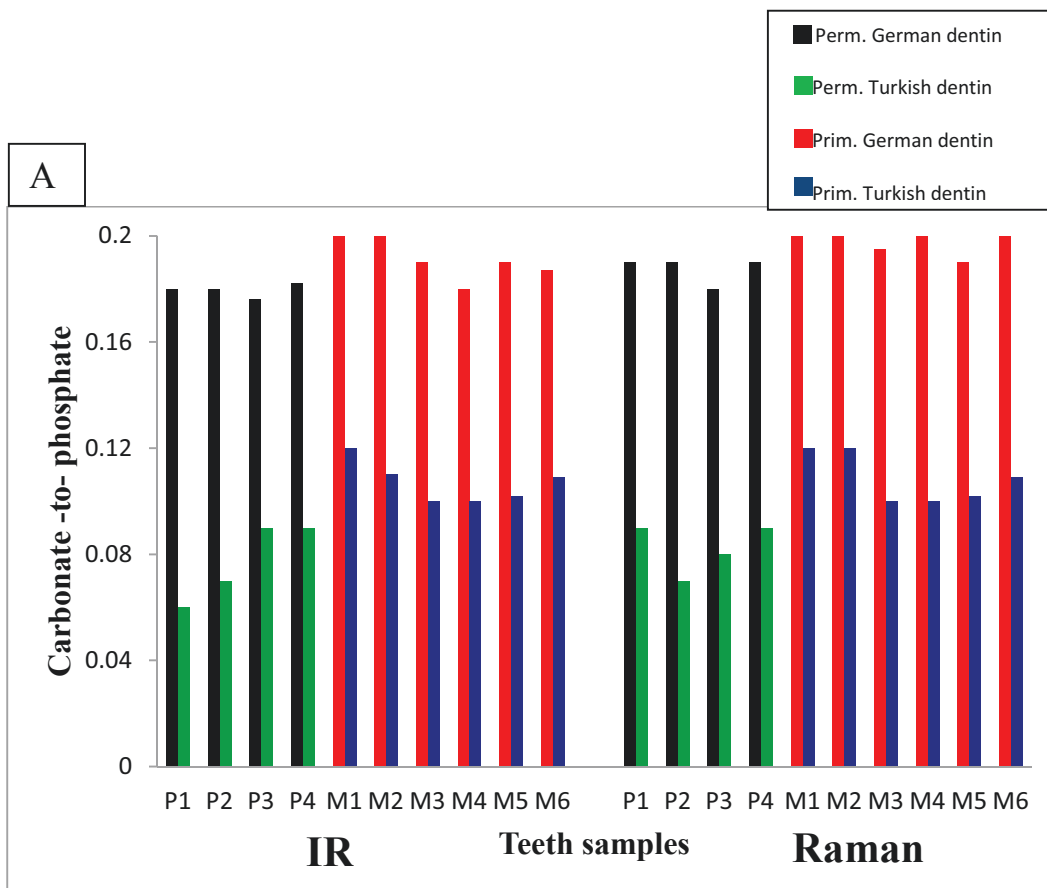
Fig. 4.3B: ATR-FTIR and Raman images variation of mineral-to-matrix ratio of permanent and primary Jordanian (Archaeological) teeth.

4.5 Carbonate to phosphate ratio

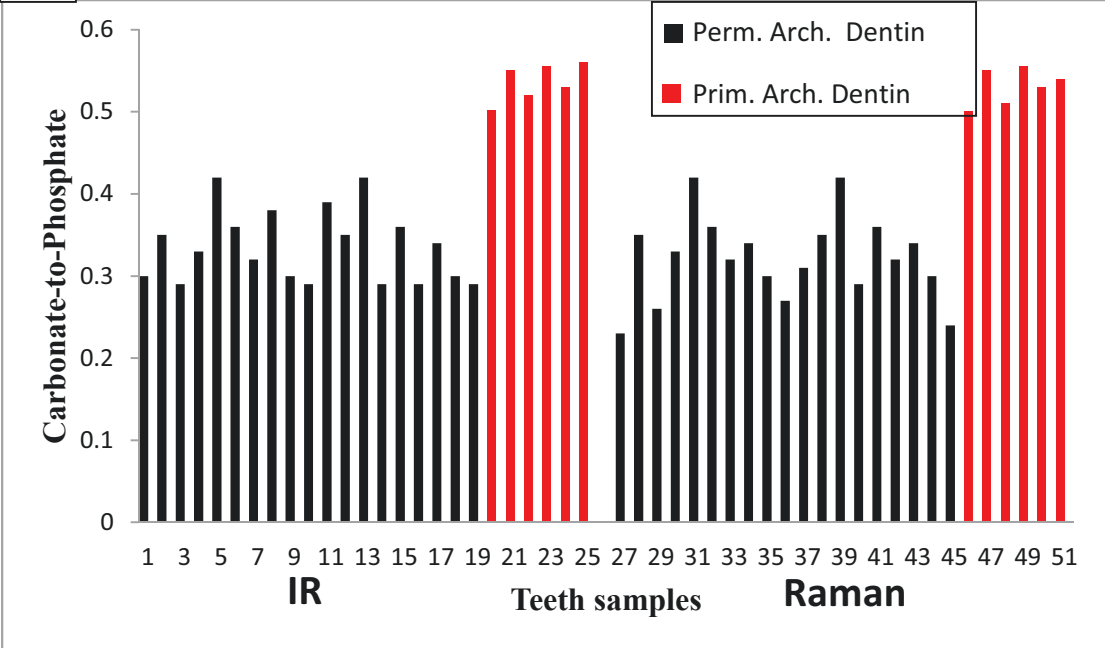
The relative carbonate content can easily be detected by using vibrational spectroscopy (IR & Raman) of the apatites. Intensity ratio of band B-type carbonate at 1415 cm^{-1} to PO_4^{-3} ν_3 mode subband at 1030 cm^{-1} was used to study carbonate-to-phosphate ratio (C/P) relevant to IR images. On the other hand, the intensity ratio of band B-type carbonate at 1070 cm^{-1} to PO_4^{-3} ν_3 mode at 960 cm^{-1} on Raman images was used to reveal the difference in carbonate ratio of the permanent and primary teeth. The reason of selected carbonate band at 1415 cm^{-1} on IR images is that band does not overlap with the absorbance of other functional groups. Carbonate-to-phosphate ratio related to tissue carbonate content as determined by elemental analysis. Figure 4.4 A, B, C and D shows the higher carbonate content in primary teeth compared to permanent teeth in all over the

data set from the different places (Turkey, Germany and Jordan), The variation from permanent to primary teeth gave the same trend, but the difference was in the quantity of intensity ratio which means the contents in carbonate varies inside the HA lattice in order to the age and the place of sample. The higher contents of carbonate was found in archeological samples which might be based on the increasing of substitution process during the lifetime, especially in the site of A-type carbonate inside the HA lattice. Also it could be attributed to the fact that the hydroxyl site can accept more vacancies than the phosphate site, and the CO_3^{-2} has consequently more degree of freedom that causes the increase of disorder as well as the presence of hydroxide ions can be replaced by fluoride which decreases apatite solubility [183].

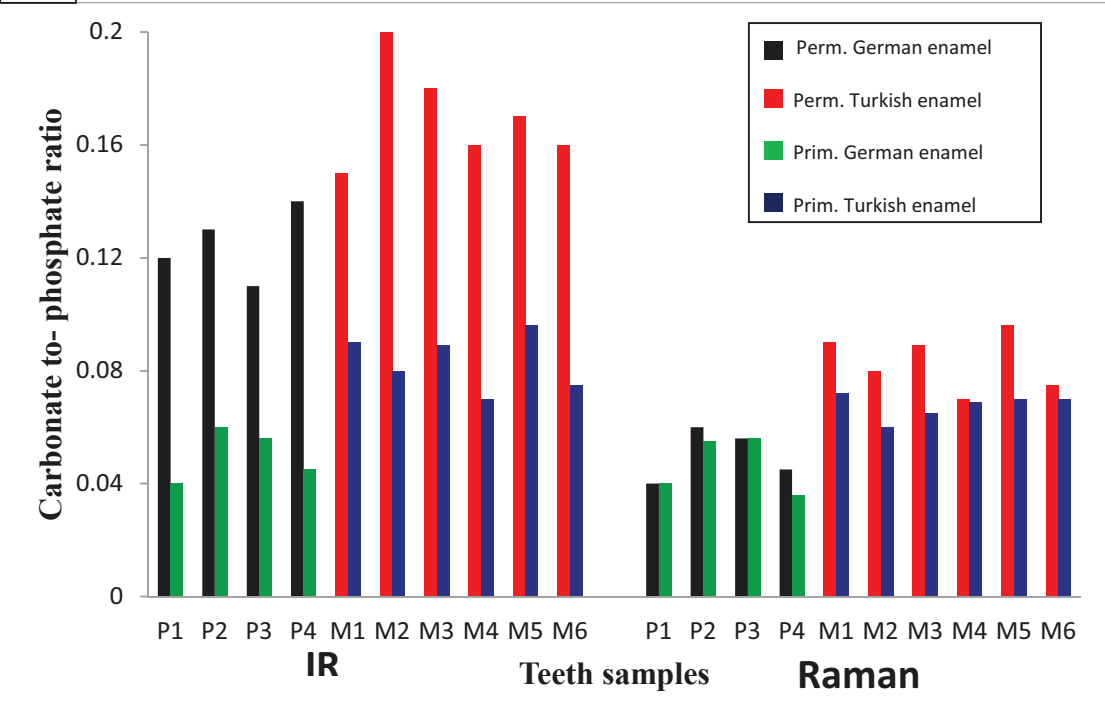
The carbonate to phosphate intensity ratio of Raman and IR data indicates that the permanent enamel of Turkish, German and Jordanian teeth is greater than the primary enamel. The same result of carbonate to phosphate intensity ratio is found inside the HAP lattice of the dentin, whereas the ratio is higher in permanent dentin compared to the primary dentin.



B



C



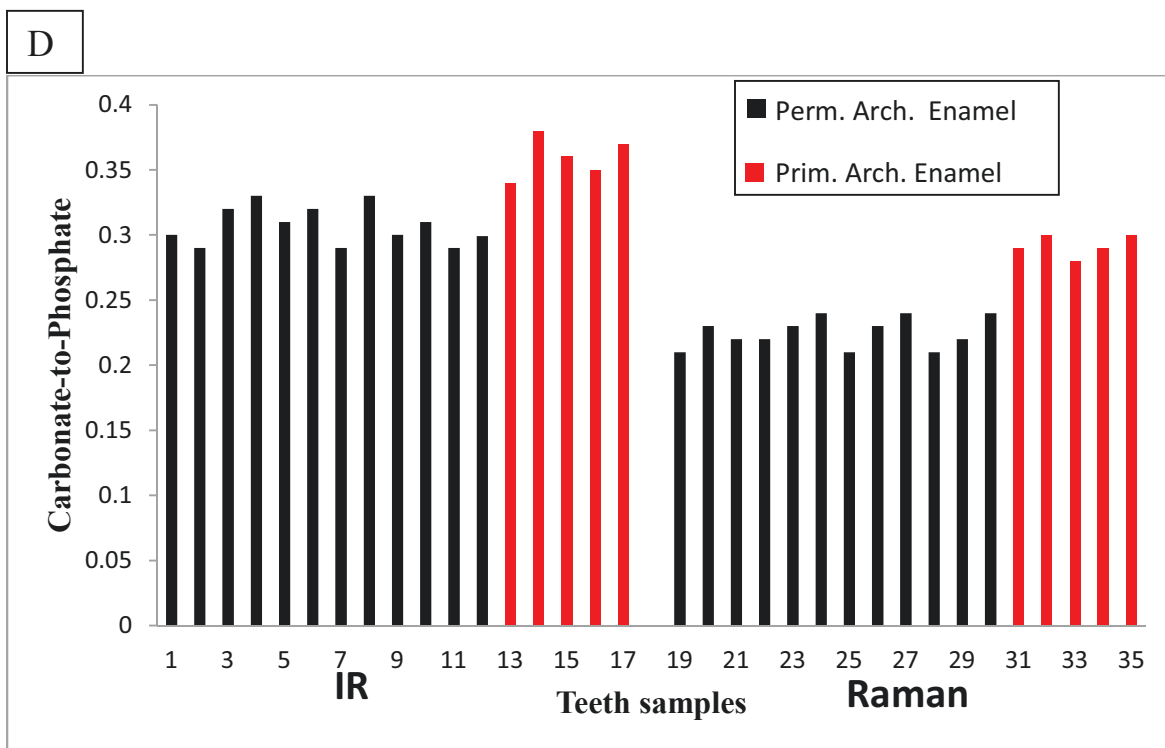


Fig. 4.4: ATR-FTIR and Raman mapping of variation of carbonate to phosphate ratio in permanent & primary teeth (dentin & enamel). A is the dentin samples of German and Turkish teeth, B is the dentin of archaeological teeth, C is the enamel of German and Turkish teeth and the last figure D is constructed from the enamel zones of the archaeological samples.

4.6 Cross-links

Collagen fibrils provide the mechanical support that enabled large multicellular animals to evolve on earth [184-185]. The tensile strength of collagen depends on the formation of covalent intermolecular cross-links between the individual protein subunits [186]. It has long been noted that the cross-linking of collagen in bone, and other tissues that mineralize (dentin, calcified tendons) is distinctive, and probably functionally related to the intimate relationship between mineral crystallites and the packing arrangement of collagen molecules in fibrils [187-188]. The structural quality of the trabecular architecture of human cancellous bone was found to be linked to the ratio of pyrrole to pyridinoline cross-links [189]. Also, a change in the cross-linking

pattern along turkey tendons just before they mineralize suggests a causative relationship between cross-linking quality and mineralization [190]. In a fracture repair model, the ratio of hydroxylysyl pyridinoline (HP) / Lysylpyridinoline (LP) and hydroxylysine content of the callus collagen was strongly related to the degree of fibril mineralization [191]. Methods for detecting cross-linking residues spectroscopically in sections of bone tissue using FTIR show promise in exploring this further [107, 192]. Pyrrole cross-links, which are not stable to acid hydrolysis, are difficult to quantify and characterize. A method that uses biotinylated Ehrlich's reagent to derivatize the residues prior to isolation has been reported [193]. Lysyl pyridinoline, a recognized biomarker of bone collagen, has now been synthesized as a standard and reagent source for developing biomarker immunoassays [194].

Dentin is a composite material containing mineral nanocrystallites and a protein matrix that is a predominantly cross-linked type I collagen. The two subbands at 1660 and 1690 cm^{-1} are indicative of secondary structure changes associated with collagen crosslinking and the intensity ratio of that subbands is frequently used to calculate the nonreducible/reducible crosslinks ratio [195]. The variation of collagen cross-links index is measured as changes in the amide I envelope. The biochemical analysis of collagen model peptides showed that Pyridinoline (Pyr) crosslinks resulted in a band at 1660 cm^{-1} , and Dehydro-dihydroxy-lysinonorleucine (de-DHLNL) crosslinks in a band at 1690 cm^{-1} .

It is known that the content of (de-DHLNL) crosslinks decrease with bone collagen maturity, while Pyr crosslinks increases [117]. On the other hand, the concentrations of (LP) and (HP) collagen crosslinks in dentin have been studied to assess if that concentrations increase during lifetime. The result was reported that the concentrations of HP and LP did not increase with age and varied between individuals of the same age and that determination of dentinal concentrations of HP and LP cannot be used to determine the individual age. However, in our study we found that the collagen crosslinks index based on intensity ratio of 1660 to 1690 cm^{-1} is higher in primary dentin from both methods (IR and Raman) compared to permanent dentin in German and Turkish teeth samples, Fig.4.5A. Unlike the permanent teeth collagen crosslinks index appeared to be constant in primary teeth especially on Raman results. Fig.4.5B shows the Raman results of collagen crosslinking in the archaeological specimens. Due to the degradation of organic materials the results show the lower index of crosslinking compared to the modern samples. Raman spectroscopy is more sensitive to detect the low amount of proteins inside the

dentin than the IR instrument especially in ancient teeth. Whereas the data showed only Raman result of collagen crosslinking index of the archaeological samples.

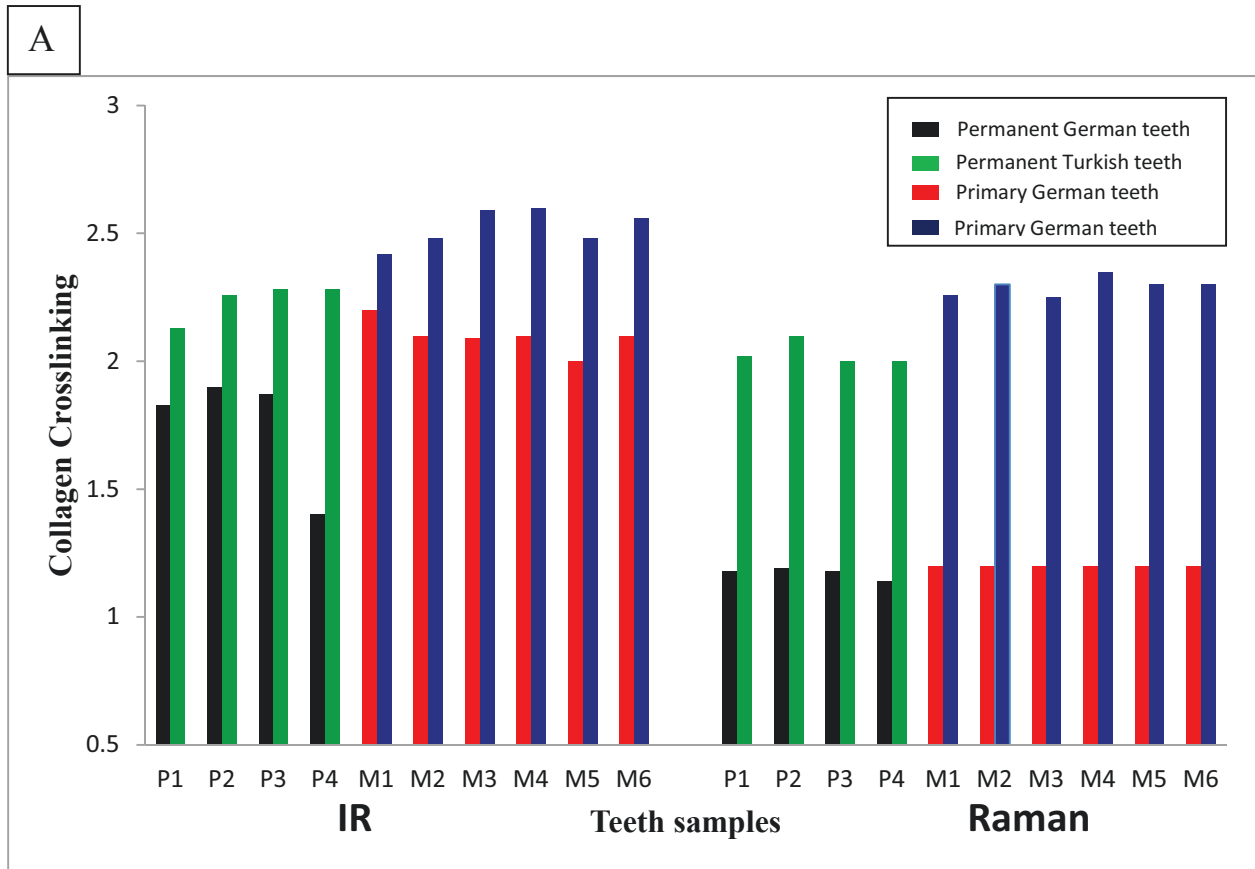


Fig. 4.5 A: ATR-FTIR and Raman variation of collagen crosslinking index of permanent & primary of German & Turkish teeth.

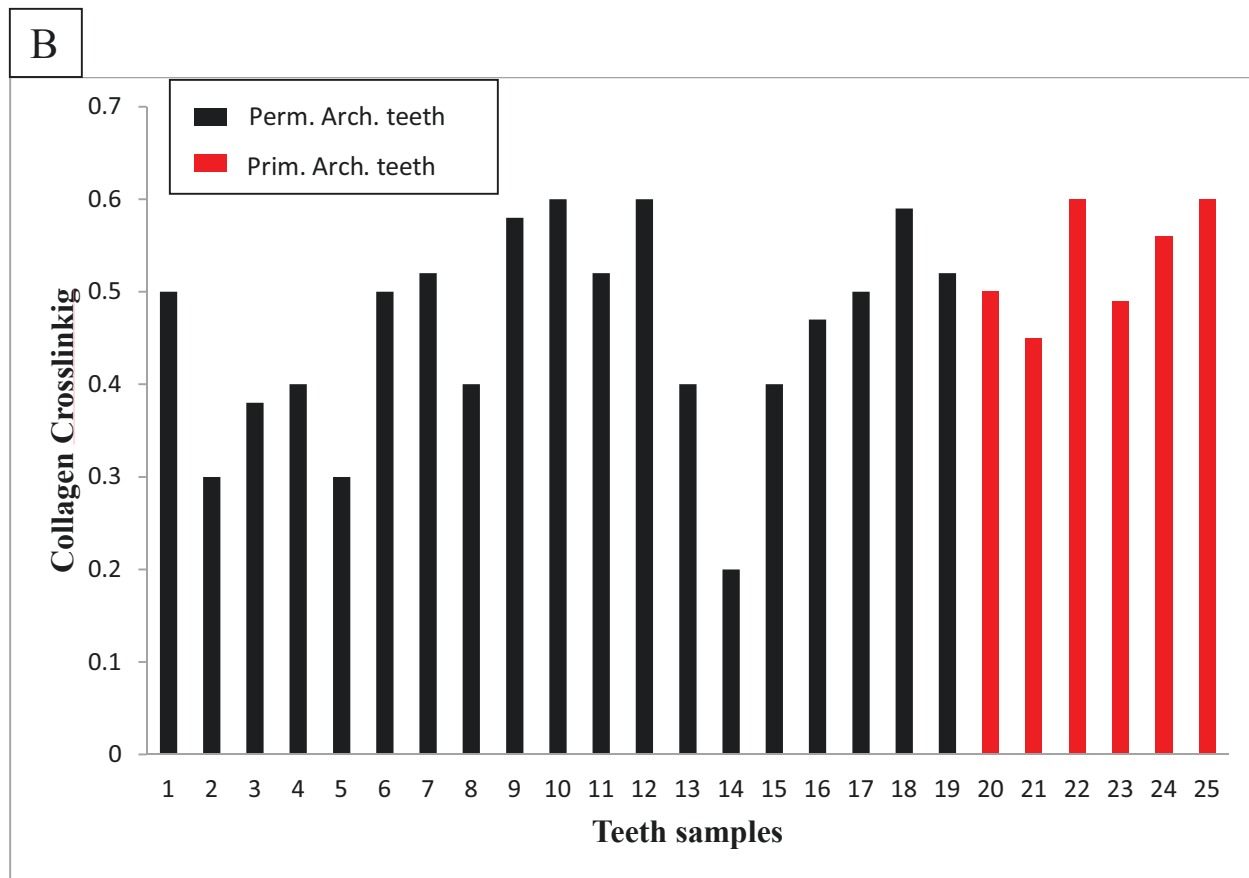


Fig. 4.5 B: Raman variation of collagen crosslinking index of permanent & primary of Archaeological teeth.

4.7 Crystallinity

Crystallinity is not only important for understanding biomineralization, it is also related to the maturation and mechanisms of growth of calcium phosphates in biological tissues. Figure 4.6 (A&B) represents the intensity ratio of IR subbands at 1030 and 1020 cm^{-1} which are related to $\text{PO}_4^{-3} \nu_3$ and HPO_4^{-2} respectively of modern teeth (A) and archaeological teeth (B). This ratio has become a standard largely used in the literature to study the crystallinity and it reflects phosphate stoichiometric and non-stoichiometric environments and it is related to the crystal size and perfection as determined by X-ray diffraction line broadening [197]. On the other hand, mineral crystallinity is directly proportional to the inverse of Raman peak width of P-O at 960 cm^{-1} corresponding to the symmetric stretching vibrational of the PO_4^{-3} . The higher mineral crystallinity is correlated the narrow peak width. The broader the spectral bandwidth is correlated with the lower the degree of the mineral crystallinity. It was reported that the crystal structure of

mineral in enamel and dentin is different [35, 198-200]. These differences are related to the width and shape of phosphate peak at 960 cm^{-1} , based on the Raman results a significant variation in the width of Phosphate band human dental enamel and dentin of the permanent and primary teeth, listed in table 4.1. The results showed the higher mineral crystallinity was observed for the permanent enamel tissue compared to other tissues. IR results figure 4.6 A & B observed the crystallinity is different in the enamel compared to the lower crystallinity in modern samples (German & Turkish samples). The crystallinity index of permanent enamel is higher in comparison to other permanent and primary modern tissues. The IR results based on archaeological teeth Fig.4.6B showed that the crystallinity index does not differ between the permanent and primary teeth. On the other hand, Raman results based on the width variation of phosphate peak at 960 cm^{-1} , (table 4.1) showed the crystallinity increased in the order: primary dentin < permanent dentin < primary enamel < permanent enamel.

Crystallinity was analyzed [] using the same 1030/1020 relative peak heights ratio that was used here. It was reported that dentin at the mineralization front, which was considered to constitute the earliest formed dentin, is poorly crystalline. The same study reported that the HPO_4^{2-} decrease during maturation in dentin. Several studies of maturation in synthetic apatites [197] or bone [79, 97, 98, and 201] also showed mineral crystallinity analyzed by either X-ray diffraction or spectroscopically increasing with tissue age. The finding agreed with previous works which are mentioned above, whereas the permanent teeth samples (dentin & enamel) have higher mineral crystallinity than the primary samples.

In general, the dentin HAP and the enamel HAP have different crystallinity. The crystallinity of enamel HAP is much higher than that of dentin HAP of modern samples (German and Turkish), which means that the HAP in enamel is regularly arranged, and in dentin the arrangement of HAP is different from the enamel HAP. As a comparison, mineral crystallinity of the German teeth samples is reported to be higher than the mineral crystallinity of Turkish teeth samples in Raman and IR results. This difference could be related to the environment or the diet of samples donors.

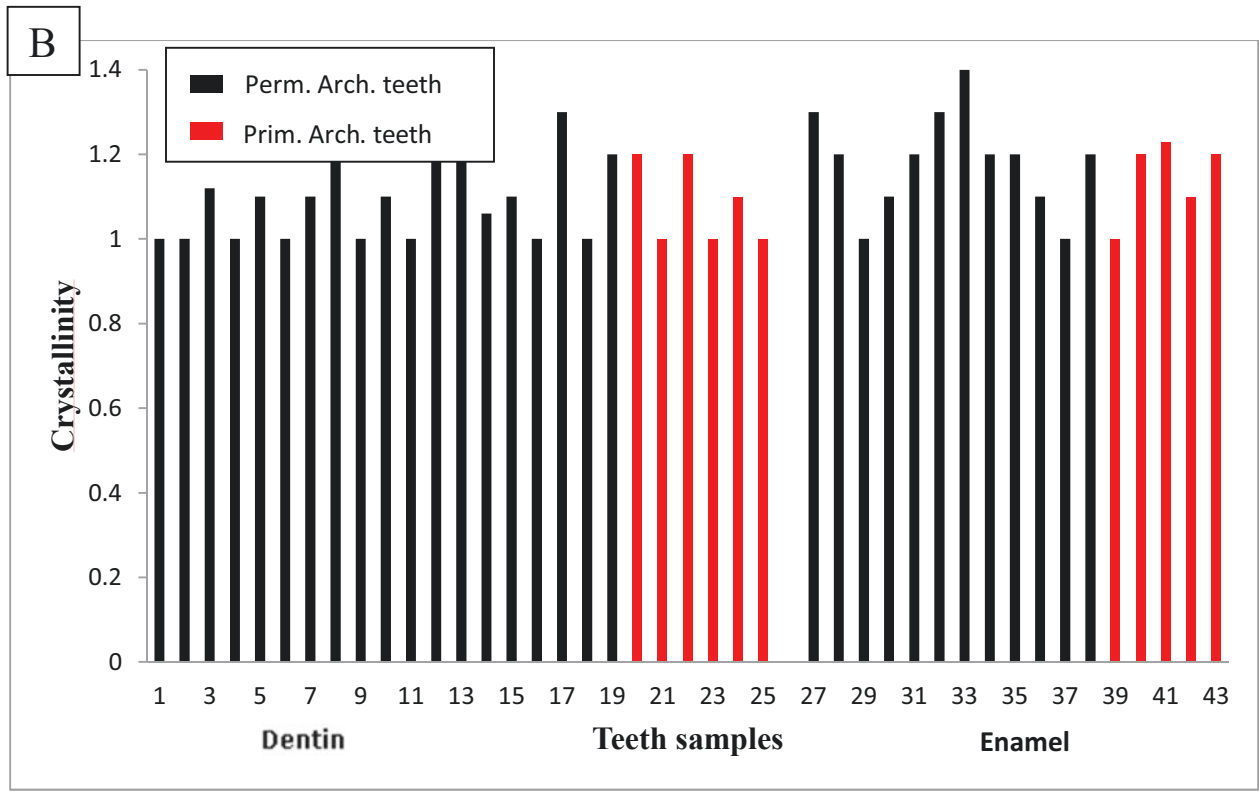
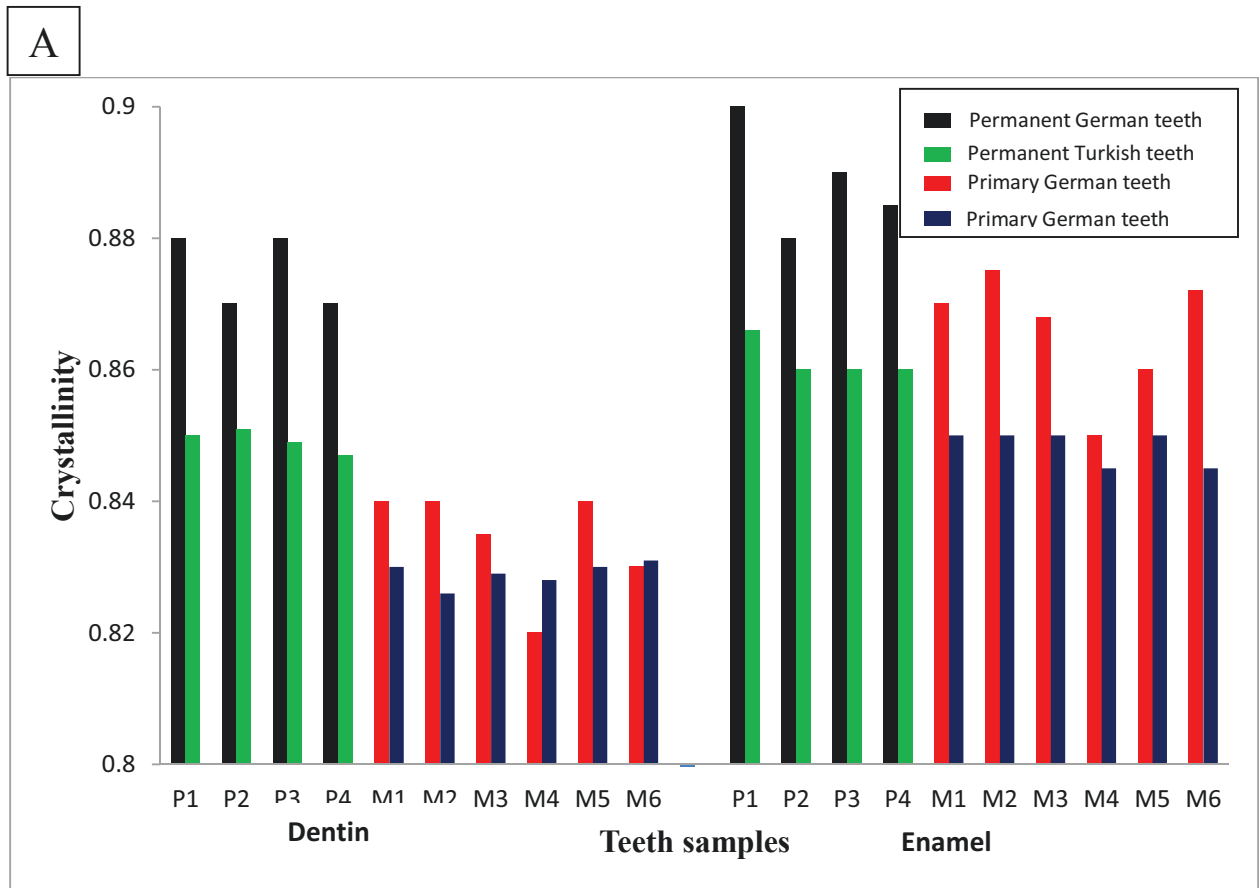


Fig 4.6 A & B: ATR-FTIR variation of mineral crystallinity index of permanent & primary teeth.

Teeth samples	FWHM(cm^{-1}) of Enamel	FWHM(cm^{-1}) of Dentin
Turkey (permanent)	13.6 \pm 0.43	17.1 \pm 0.16
(primary)	13.8 \pm 0.5	17.2 \pm 0.47
Germany (permanent)	13.8 \pm 0.12	17.6 \pm 0.56
(primary)	14.7 \pm 0.66	18.5 \pm 0.37
Archaeology (permanent)	14.1 \pm 0.99	15.8 \pm 0.88
(primary)	13.1 \pm 0.97	17.5 \pm 0.38

Table 4.1: The band width of the ν_1 phosphate band of human dental tissues from the permanent and primary teeth spectra \pm the standard deviation.

As a result, the imaging parameters (mineral to matrix ratio, carbonate to phosphate ratio, crystallinity and substitution in HA lattice) to characterize the calcified tissues are correlated. On the other hand, the crystallinity gives essential information in growth of calcium carbonate, and it is well known that the most of the calcium in the human body is stored in the bones and teeth; also the bones and teeth are not permanent or unchanging structure. In fact, they are being constantly broken down and rebuilt. It is essential to keep a certain steady level in the blood. If blood calcium carbonate levels are too low the body will break down the bones and teeth to increase the blood calcium carbonate levels. If the calcium levels in the blood are high, then the body uses the extra calcium carbonate to rebuild the bones and teeth. Du to that of calcium levels in blood and the break down and rebuilt again, the differences in quantities of imaging compositions might be explained for German teeth compared to the Turkish teeth.

4.7 Raman dating of the archaeological teeth

Raman spectroscopy has been applied in archaeology to identify and study the archaeological materials. In this work we investigated many ancient teeth samples from a historical site in Jordan, as we showed in previous sections. The age of these samples was not known. However, Carbon-14 or radiocarbon is a method to date the archaeological, geological,

and hydrological samples. There are three types of isotopes of carbon on earth. 99% of the carbon is carbon- 12, 1% of carbon- 13, and carbon- 14 occurs in trace amounts, 1 part per trillion of the carbon. The half-life of carbon- 14 is 5370 ± 40 years and it decays into nitrogen-14 through beta decay. The cost of radiocarbon dating varies between different laboratories, but it is not cheap. The high cost is because it is a job to date a sample. It takes a long time to change the carbon materials into the form it needs to be able to be dated.

Furrier transform Raman was used to analyze ancient teeth (150 to about 6000 years ago) [202]. The authors used the carbon- 14 to determine the age of those samples, and then they examined the age results by comparing to the intensity ratio of CH₂ Raman peak at 2941 cm⁻¹ to the intense peak of phosphate band at 960 cm⁻¹. They concluded the final result as shown in figure 4.7A. In this work we used that investigation to estimate the age of the archaeological samples. It is a simple way to date the ancient teeth in order to the intensity ratio of the organic Raman spectral band at 2941 cm⁻¹ to the inorganic Raman spectral band at 960 cm⁻¹. Figure 4.7B shows the relative intensities I_{2941} / I_{960} of Jordanian ancient teeth. The 10 samples which have intensity ratio less or equal to 0.1 (under the green line) were estimated to be in time period of (1000-2000 years ago) and the rest (more than 0.1) are in range of 1000 years ago or less. Carbon- 14 was used to date some samples of bones found from the same excavation of teeth site and the results (data not shown) were in agreement to Raman results of teeth dating.

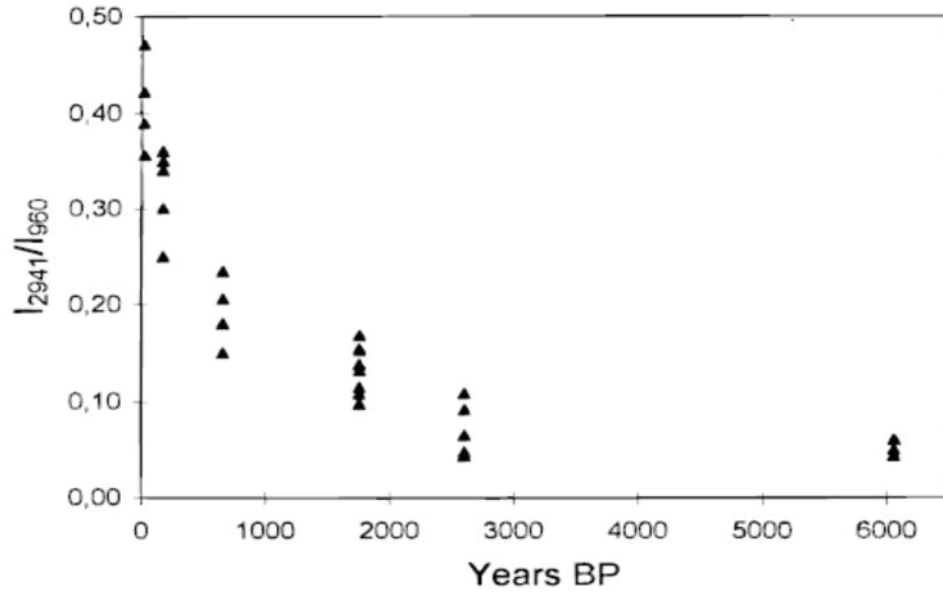


Fig. 4.7 A: I_{2941} / I_{960} relative intensities as a function of tooth burial period [202].

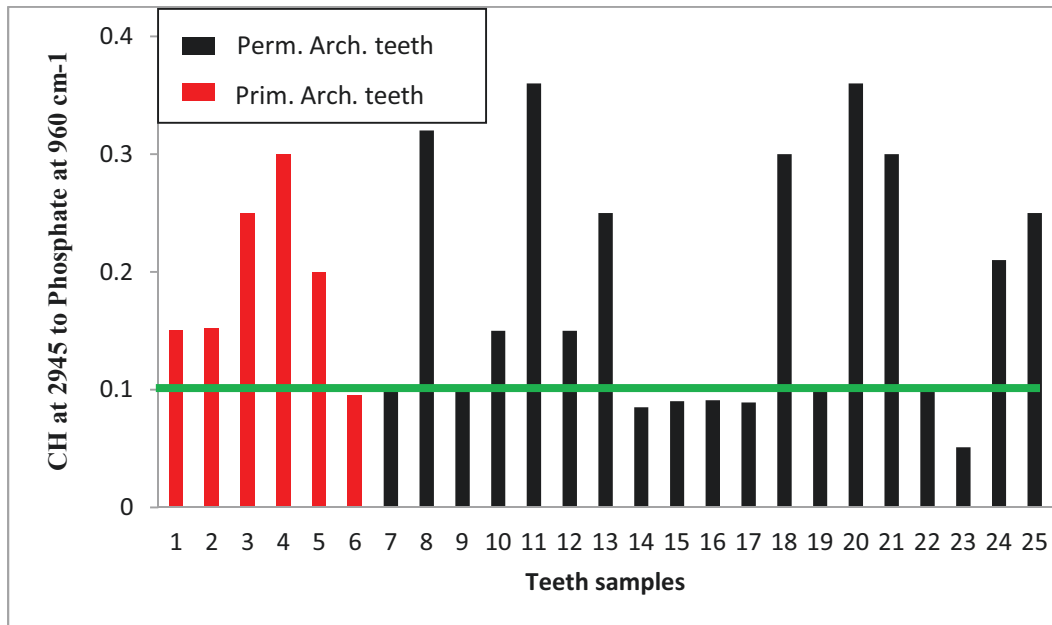


Fig 4.7 B: I_{2941} / I_{960} relative intensities of Jordan ancient teeth.

Chapter 5

Result and discussion (dentin enamel junction)

The DEJ is the initial location for cells that are responsible for the secretion of enamel and dentin. It is thought that the DEJ is greatly influenced by enamel knots that form before the mineralization of the tissue secret [203]. Lucas (2004) describes that the first enamel formed, at the DEJ, has not been well studied, and appears to have a random orientation under light microscope [204]. In this work we presents the application of multivariate analyses to analyze micro-Raman spectral imaging data in reference to the dentin enamel interface as well as the comparison with univariate analysis. The univariate statistical methods such as mapping of specific functional group peak intensities do not always detect functional group positions and quantities due to peak overlapping. Multivariate methods usually use to detect the variations in the spectra that are difficult to observe using univariate methods. Figure 5.1 represents a photograph of a tooth slice, where spectral maps were obtained. The imaging parameters of measurements have been mentioned in chap. 3 section 3.9.2 b.

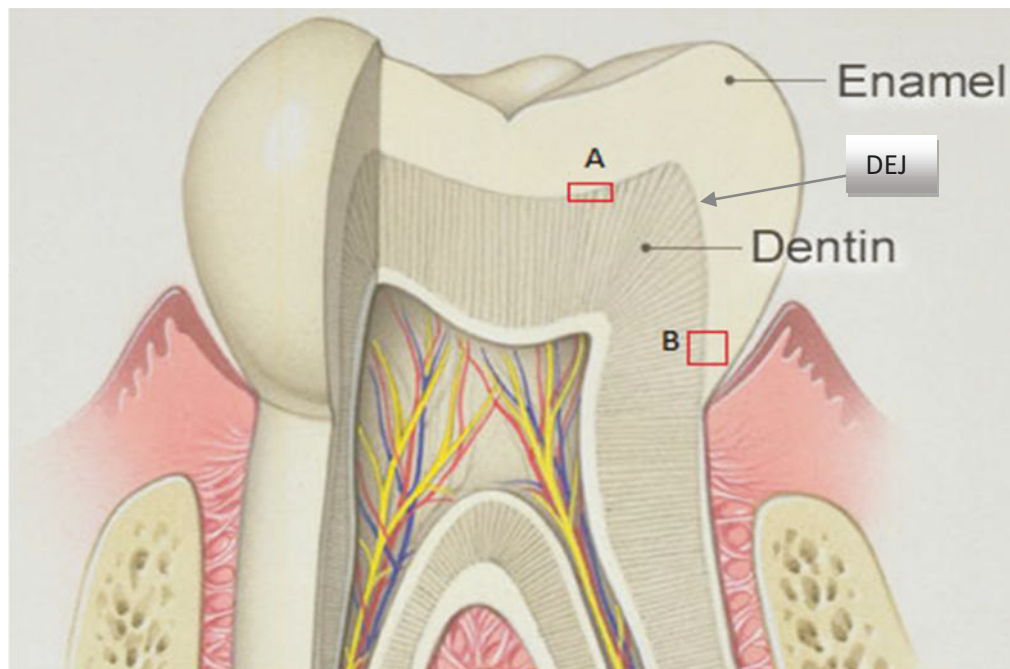


Fig. 5.1: scheme of a cross-sectional tooth slice illustrating where spectral maps were obtained. where A is an occlusal position and B a cervical position.

5.1 Univariate analysis result

Representative Raman mapping results of the DEJ at occlusal and cervical sites of a human tooth are shown in Fig. 5.2 A and B, respectively. Raman images were obtained based on the intensity ratios of CH at 1450 cm^{-1} (matrix) to phosphate at 960 cm^{-1} (mineral). The relative matrix/mineral (1450/960) ratios are represented by the color differences. Red/pink color represents the lower relative ratio (Enamel), while green/yellow/orange represents the higher relative ratio (dentin). A region where the color changes from blue or sky blue is related to the DEJ transition zone. Comparison of the two images indicates that the width

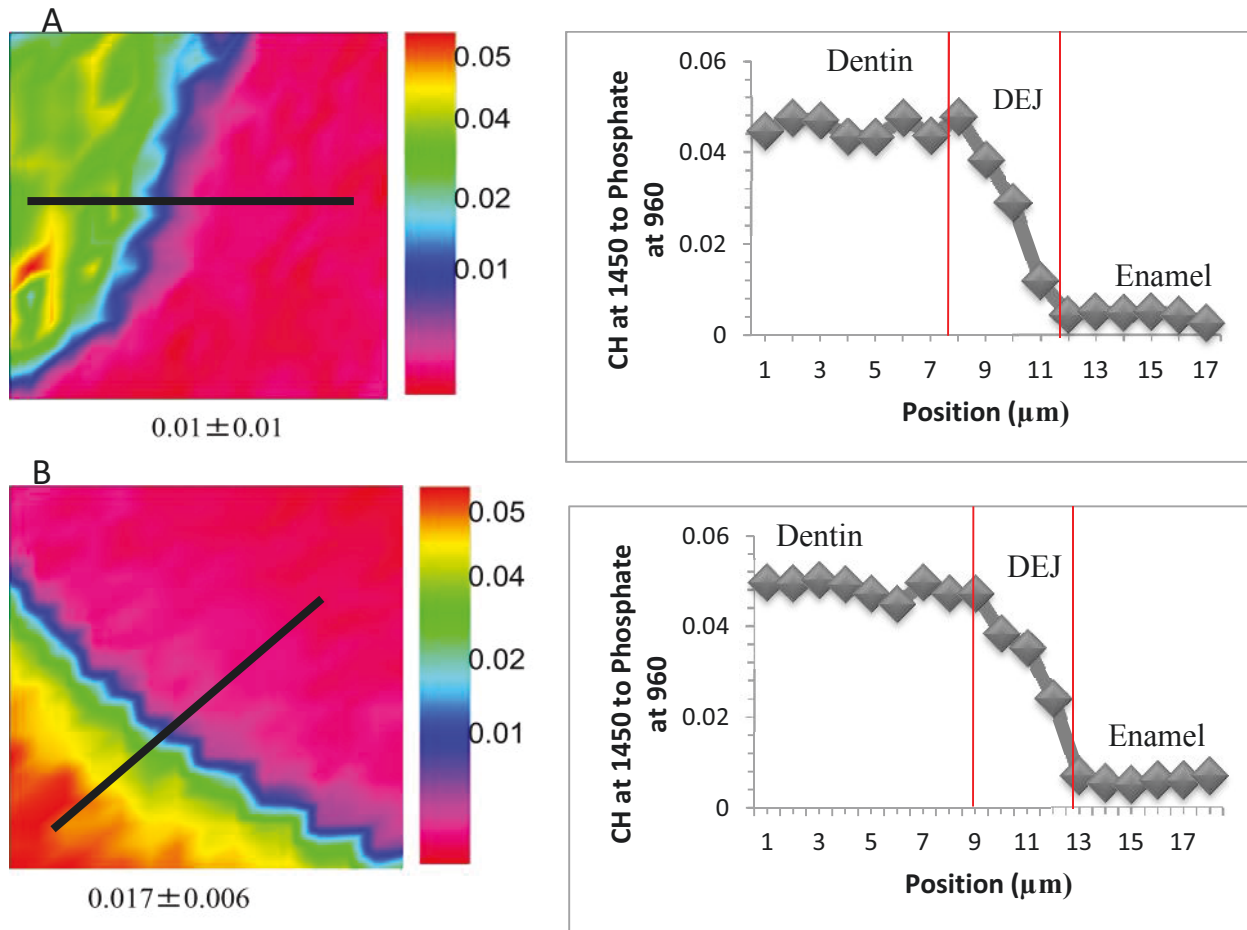


Fig. 5.2: Representative Raman images and relative intensity ratios of the DEJ based on intensity ratios of 1450/960 at occlusal (A) and cervical (B) positions for permanent teeth. The bold black line represents the position where the DEJ determined.

Red/pink color represents the lower relative ratio (Enamel), while green/yellow/orange represents the higher relative ratio (dentin). A region where the color changes from blue or sky blue is related to the DEJ transition zone. Comparison of the two images indicates that the width

of DEJ transition zone at cervical position is the same of at occlusal position, and it equals to 4 μm . The representative relationships of the carbonate to phosphate (1070/960) ratios as a function of positions across the DEJ transition zone are shown in Fig. 5.3A and B. The matrix/mineral ratios of the DEJ were higher than those of enamel and lower than those of dentin. These ratios of the DEJ gradually increased during the transition from the enamel to dentin zone. The width of transition zone equals to 5 μm at both positions (occlusal & cervical).

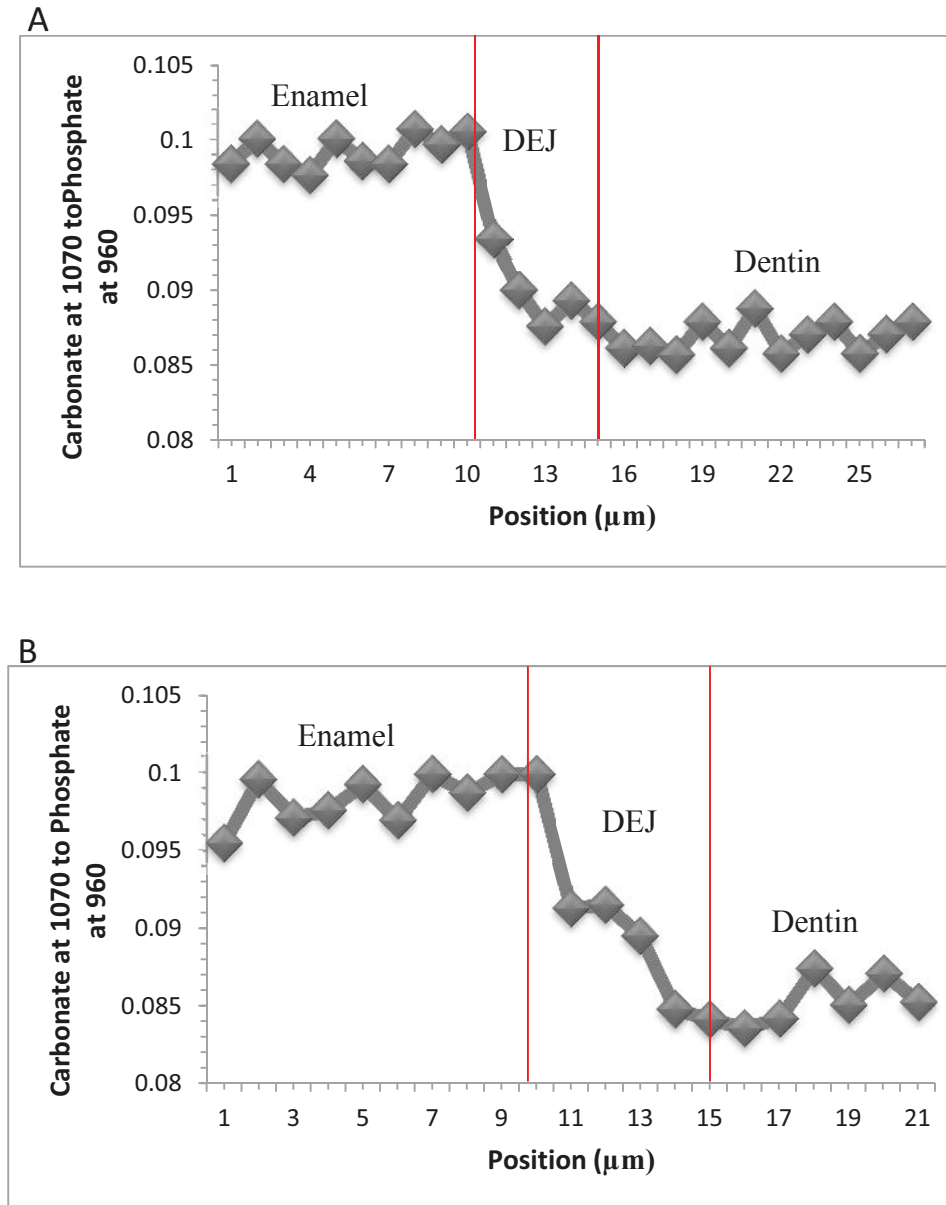


Fig. 5.3: relative intensity ratios of 1070/960 across the enamel/DEJ/dentin zone at occlusal (A) positions and at cervical (B) positions.

On the other hand, average Raman spectra from the dentin and DEJ area in the protein- derived spectral region of 1200- 1750 cm^{-1} are shown in figure 5.4A, in which the vibration peak of CH at 1450 cm^{-1} was selected as internal standard for the normalization adjustment. As compared to dentin spectra, the amide I peak increased, but the amide III peak decreased in the DEJ spectra. Also the average spectra from the dentin and DEJ zone in the spectral region of 900- 1200 cm^{-1} are shown in figure 5. 4B. The spectra were normalized based on phosphate peak at 960 cm^{-1} . The spectra showed that the peak at 1070 cm^{-1} which is related to the carbonate type-B from the DEJ spectra is higher than the carbonate peak from the dentin average spectra.

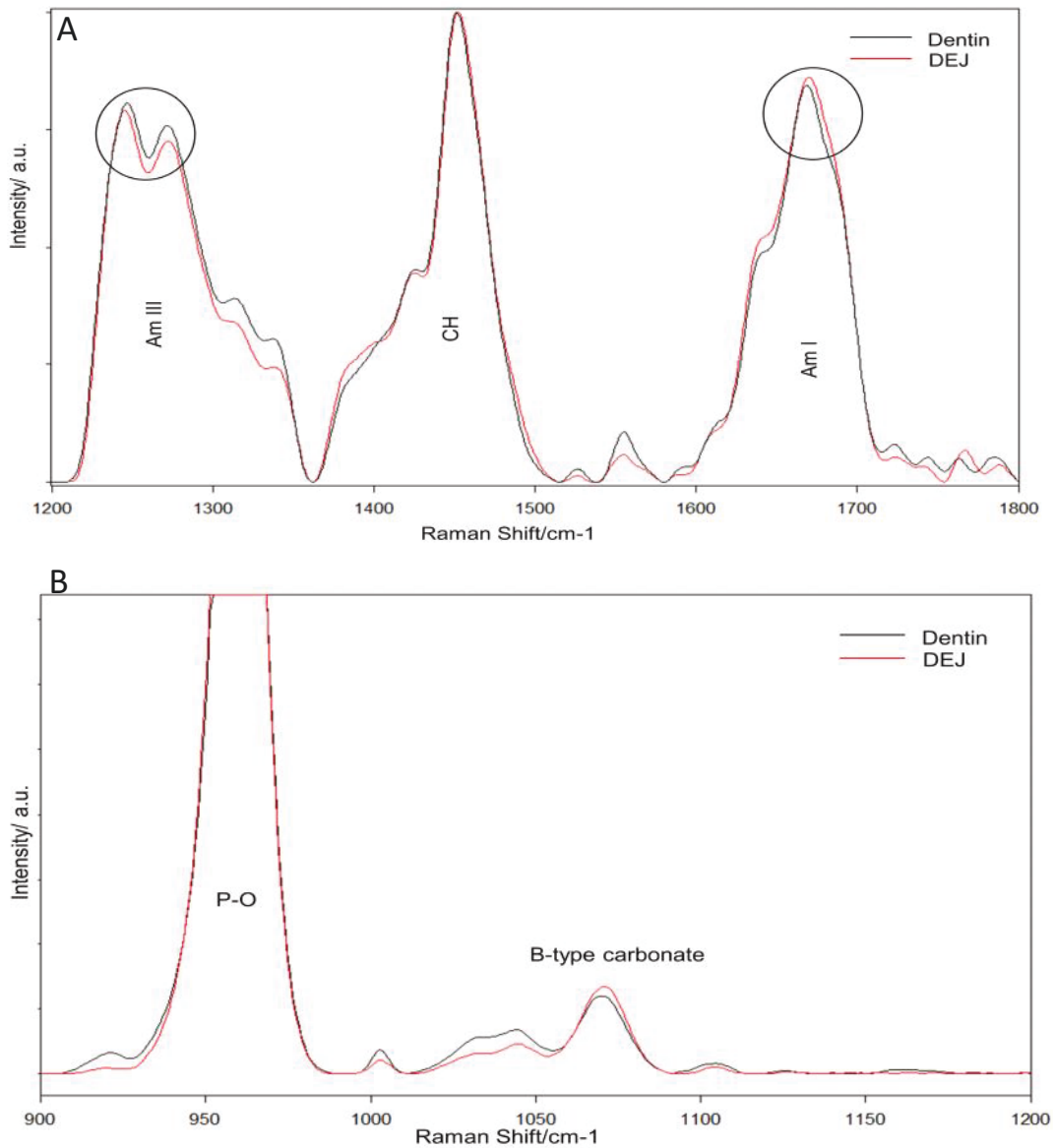


Fig. 5.4: Raman spectra in protein-derived (A) and in mineral-derived (B) spectral regions from dentin and the DEJ.

5.2 Multivariate analysis result

Raman spectra collected are often contaminated with various interfering signals. The sources of interference include fluorescence and stretching of spectral intensity amplitudes. The amplitude stretching (intensity variations) could be due to specimen inclination, variation in specimen thickness and absolute intensity of light. For instance, mineral and protein contents of dentin show variations compared to the enamel. In order to eliminate interfering signals and bring the spectra to a common platform of comparison, some preprocessing were performed. Data was carried out as we mentioned in chap. 3, by using the Cytospec software and MatLab procedures written in-lab. A baseline correction by polynomial fitting of a second degree was used to remove of the florescence background with no smoothing.

Figure 5.5 A, B representative the average Raman clustering image with three components and its related spectra. The size of image is $70\ \mu\text{m} \times 70\ \mu\text{m}$ in the spectral range from 600 to $1800\ \text{cm}^{-1}$. The transition zone in blue color clearly appeared without fixed width across enamel (in red) to the dentin of green color.

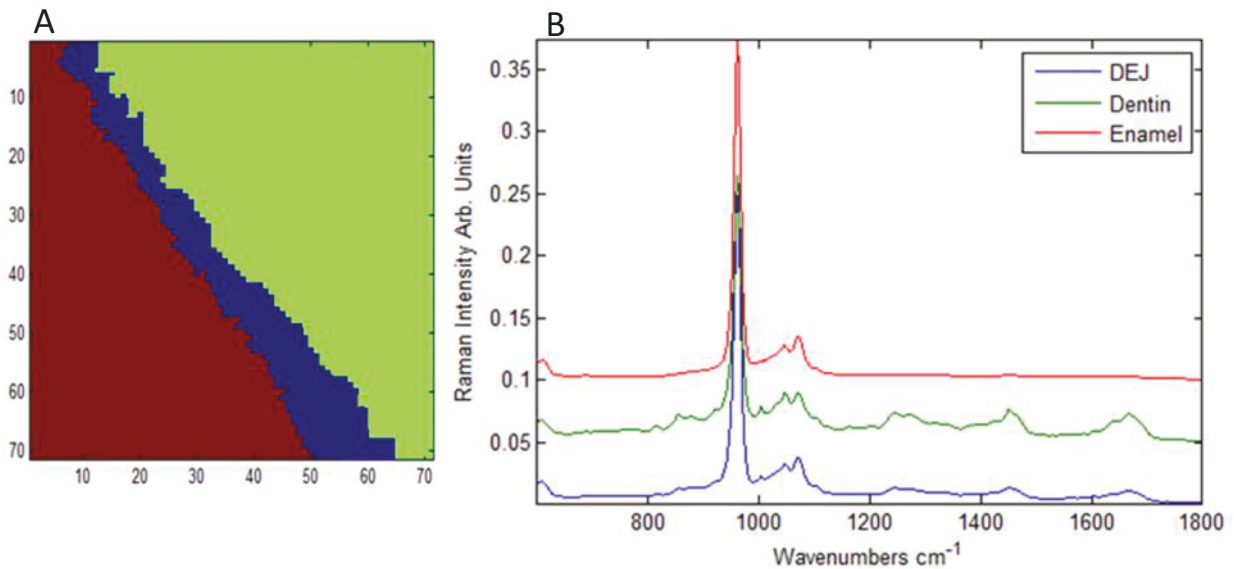
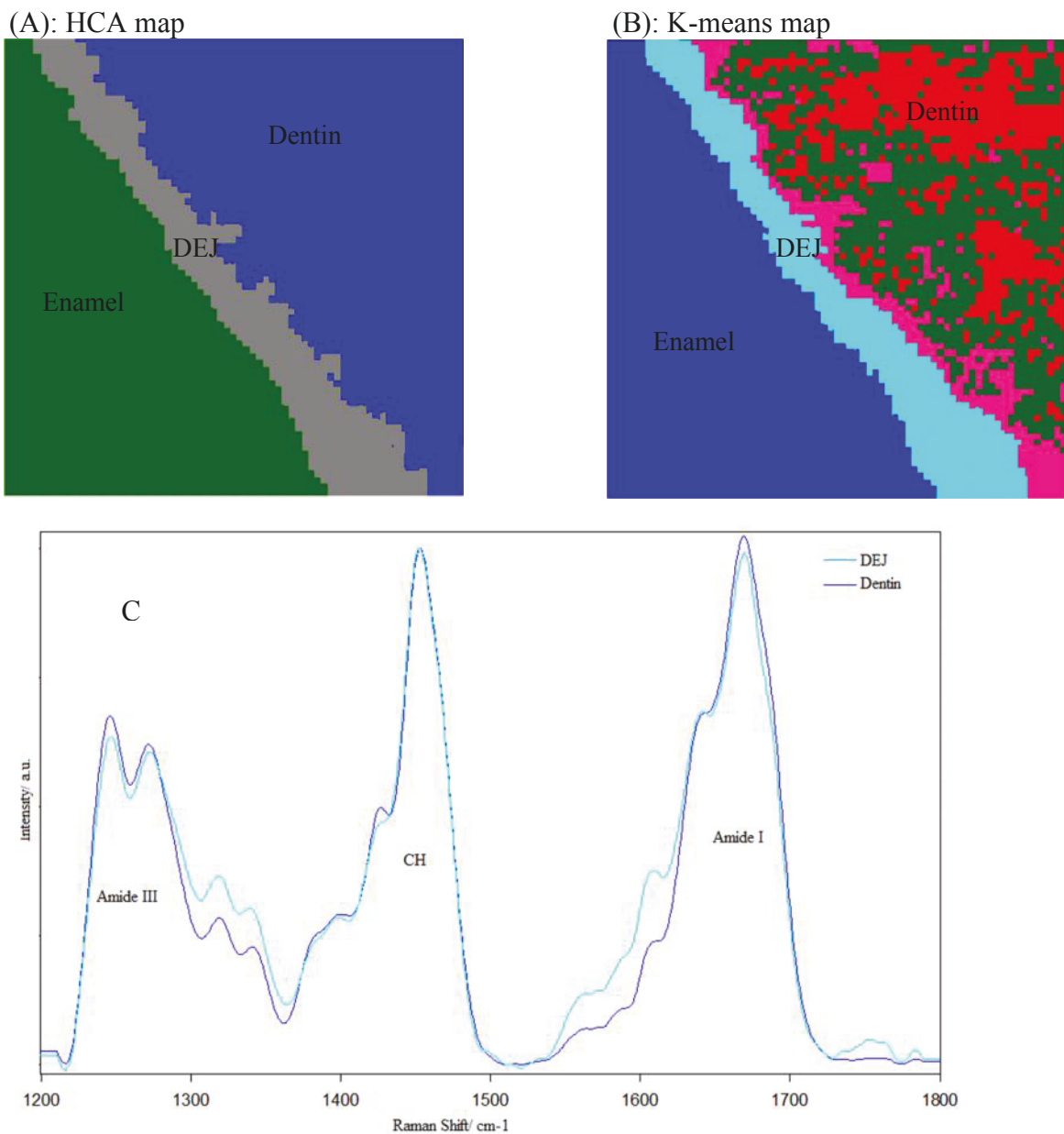


Fig. 5.5: representative average Raman clustering image (A) with three components and its related spectra (B).

5.2.1 K-Means Cluster & hierarchical cluster analysis result

Cluster analysis is an unsupervised statistical method of grouping the data, without a priori knowledge of its nature. The initial centroids of K-means clustering are randomly chosen. The distances are calculated between a spectrum and the centroid. Then each spectrum is assigned to the cluster whose centroid is nearest and the data set is grouped into a preselected number (K) of clusters. Figure 5.6A, B, C & D shows the HCA & k-means cluster analysis maps of 70 μm X 70 μm of Raman image A& B and Raman averaged spectra of protein and mineral region C & D.



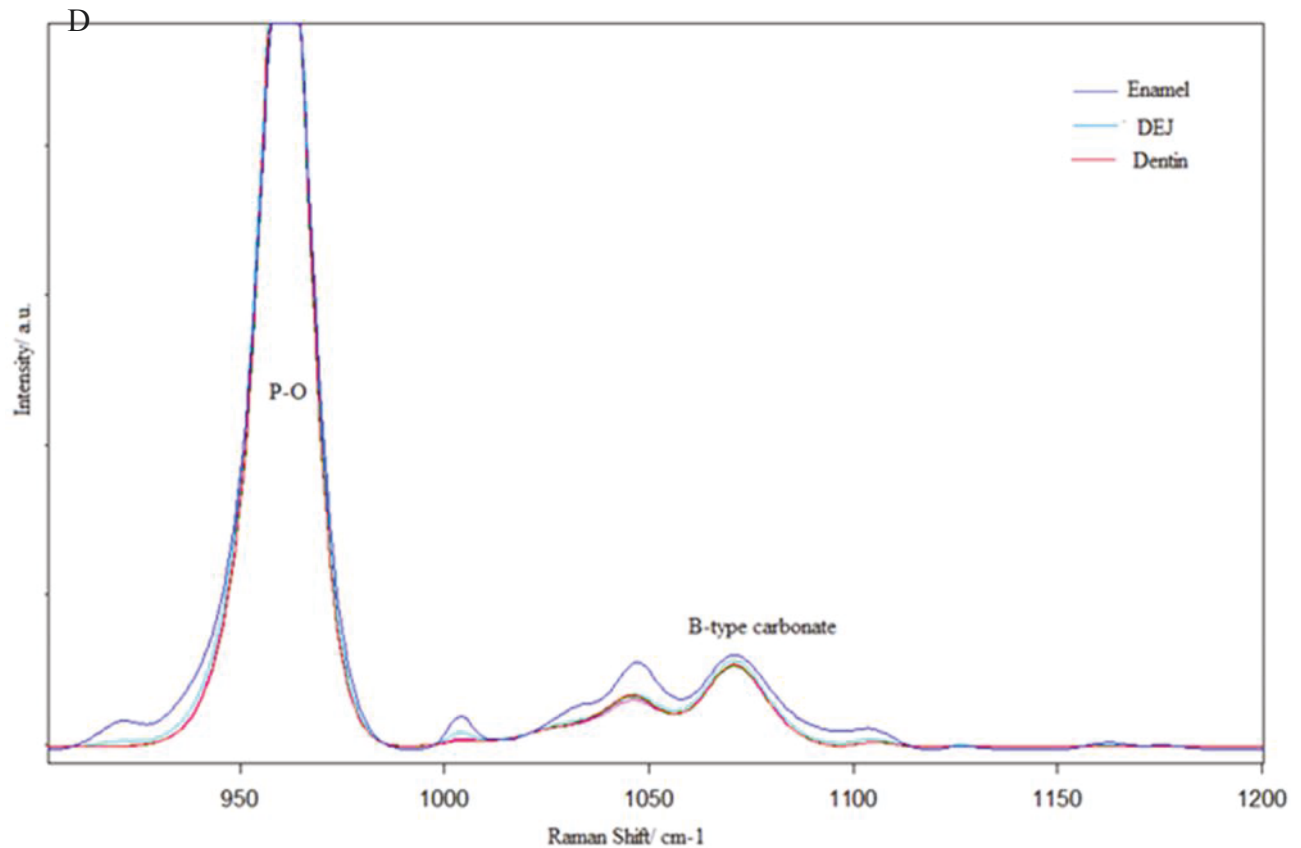


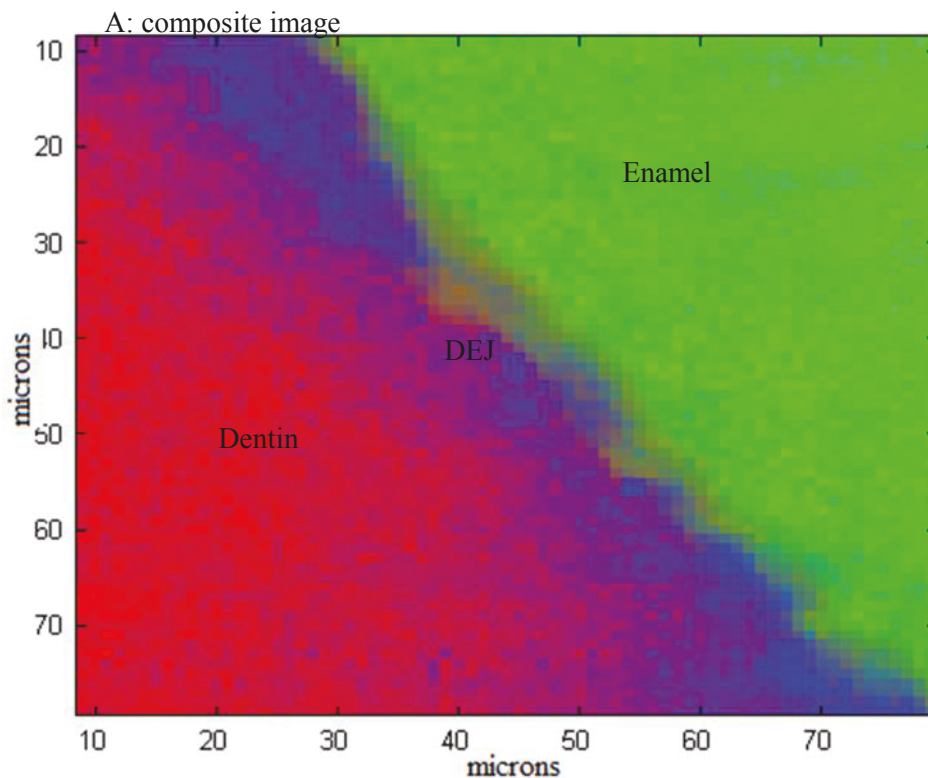
Fig. 5.6: Map of hierarchical cluster analysis (A) and map of k-means cluster analysis (B) of a 70 x 70 Raman image from a permanent human teeth. The cluster averaged Raman spectra derived from k-means cluster analysis of protein region from 1200 to 1800 cm^{-1} (C) and the Raman averaged spectra of mineral region constructed from k-means analysis of mineral spectral region of 900 – 1200 cm^{-1} (D).

HCA and K-means cluster analysis showed identical result to distinguish the transition zone of DEJ across the enamel and dentin. The cluster analyses do not give a fixed width for the DEJ. The width was varied from 12 μm in wider width to the narrow width of 6 μm . In HCA we were used three clusters (enamel, DEJ, and dentin). While in K-means analysis five clusters were used (fig. 5.6 B). The first two clusters were related to the enamel and DEJ and the rest were attributed to dentin region. Dentin contains around 75% in mineral (HAP) and 25% proteins and water. On the hand the enamel contains 99% in mineral which looks like a homogeneous layer. Based on that different content the K-means cluster analysis carried out by using more than three clusters to give agreement result with the HCA cluster analysis. On the other hand the molecular features of DEJ in comparison to the dentin and enamel were the same results from HCA and K-

means cluster analysis. In protein spectral Raman region (fig. 5.6 C) after normalization based on CH band, the amide I and amide III peaks in dentin were higher than DEJ spectra peaks. The mineral Raman spectral region (figure 5.6 D), the spectra were normalized to phosphate peak at 960 cm^{-1} . The carbonate peaks at 1070 cm^{-1} were higher in enamel and at the same time this peak was increased on DEJ compared to the dentin spectra peaks.

5.2.2 Vertex component analysis (VCA).

VCA offers an unsupervised solution to the blind source separation problem. VCA represents the image raw data in a space of smaller dimensionality aiming to retain all relevant information and it calculates endmembers instead of loadings. Scope of VCA is that endmembers represent spectra of most dissimilar chemical constituents. Then, scores denote the concentration of the endmember spectra. The VCA algorithm iteratively projects data onto a direction orthogonal to the subspace spanned by the endmembers already determined. Figure 5.7 shows the Raman image of vertex component analysis, the composite image (A) and the first three components and its related spectra (B).



B: Score plots and the endmembers

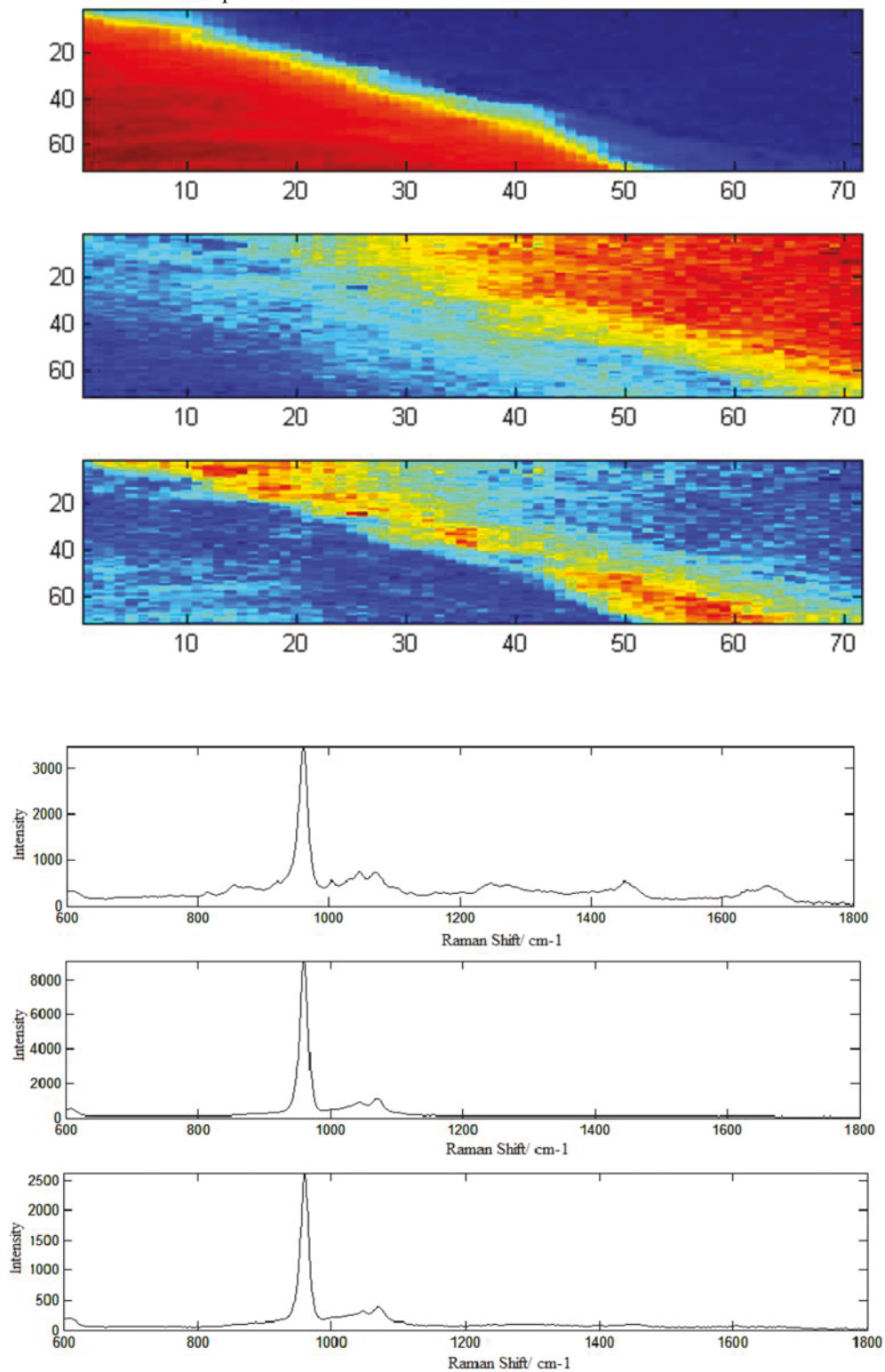


Fig. 5.7: Composite image of vertex component analysis (A) of a 70 x 70 Raman image from a permanent human tooth, of the first three components (B) are shown: dentin, enamel and DEJ, respectively.

The vertex component analysis based on three components, dentin in red, DEJ in blue and the enamel in green fig. 5.7A showed that the DEJ width varies from 12 microns in some positions to 6 microns on another positions. On the hand, the organic components in DEJ were not clearly observable compared to the dentin, while the mineral in DEJ clearly appeared to be higher than dentin in comparison to the intensity quantity of the phosphate band at 960 cm^{-1} in respect to figure 5.7 B.

Usually the interface between two materials with different mechanical properties like elasticity is a weak link in structure. The DEJ zone acts to transfer applied loads from the enamel to dentin like during the masticatory or impact and also to inhibit the crack propagation. However, many different instruments have been used to identify the DEJ, such as SEM, Raman spectroscopy and optical spectroscopy. The researchers were reported different width to the transition area, for example it was reported that the DEJ width varies from 50 to 100 μm [30], 10 μm [205] and around 2-3 μm [35]. Recently, the researchers have been investigated that the DEJ width depends on the intratooth [31], and they reported that the mean width is $12.9 \pm 3.2\ \mu\text{m}$ at occlusal position and $6.3 \pm 1.3\ \mu\text{m}$ at cervical position. To date, there has been minimal chemical information related to the DEJ transition zone due to its small size [31]. In our study, chemical compositions parameters (mineral to matrix ratios) were used to measure the width and as well as to investigate some chemical features by comparing them to the chemical properties of enamel or dentin. In terms of organic matrix, the spectral region of amides I and III were thought to be the best possible region for studying the protein structural changes [206-207]. The position and intensity of these amide bands are sensitive to the molecular conformation/structure of the polypeptide chains [208] and/or orientation of collagen/proteins [209]. To the best of our knowledge it is the first time that we used the multivariate analysis in detection of transition zone. The obtained results from different algorithms (HCA, K-means cluster and VCA) were indicated that the width of transition zone was not fixed and it varies as a function of position in microscale regardless of location (occlusal or cervical). However, the chemical structure features based on multivariate analysis suggested that the amide I and amide III peaks decreased in DEJ in comparison to the dentin Raman peaks (fig. 5.6C). The decrease in these peaks could be related to the increasing disorder of the functional groups in organic matrix [210]. These spectral differences indicate that the structure of organic matrix in the dentin and DEJ was diverse. Formation of the DEJ begins at the early stages of tooth morphogenesis and is thought to be

linked to a mixture of dentin proteins secreted by odontoblasts and enamel proteins from ameloblasts [210-212]. The proteins associated with DEJ formation and collagen fibril bundles that cross the transition zone and insert into enamel [30] might be responsible for the variations and distribution deviations in composition and structure of the organic matrix within the DEJ. In respect to the inorganic component variations, it was reported that the mineral in dentin and enamel is different [199-200, 213]. Based on results of VCA analysis (figure 5.7B) the width and shape of phosphate peak at 960 cm^{-1} of dentin and DEJ spectra were similar indicating the mineral crystallinity within the DEJ is not much different from the mineral of dentin. Moreover the intensity of carbonate at 1070 cm^{-1} increased from dentin to enamel across the DEJ area (figure 5.6 D) indicating the lower carbonate contents in dentin.

In summary, the results suggested that the width of transition zone did not have a specific width and it was varied from $12\text{ }\mu\text{m}$ to the narrow width of $6\text{ }\mu\text{m}$. also, the molecular features of DEJ differed in comparison to the enamel or dentin chemical properties. These results probably give more information besides the previous ones in the literature for understanding of the critical zone. On the other hand, DEJ analysis based on the teeth primary samples (data not shown) showed the same results of permanent teeth samples.

Chapter 6

Conclusion and future work

In this study of this dissertation, permanent and primary human teeth from different ages and places (Germany, Turkish, and Jordan) were analyzed by ATR-FTIR and Raman imaging to study the composition parameters (mineral to matrix ratio, carbonate to phosphate ratio, crosslinking and crystallinity). Substitution inside the HAP lattice of permanent and primary teeth for the dentin and enamel of German and Turkish samples was analyzed in respect to the weak shoulder of IR carbonate peak 876 cm^{-1} by using the curve-fitting process. On the other hand, Raman imaging was used to investigate the transition zone of DEJ. Chemical and molecular properties of DEJ were detected based on univariate and multivariate analysis.

The results obtained from the ATR-FTIR spectroscopy were in agreement to results from Raman technique. The mineral to matrix ratios in all different samples from different places of permanent teeth (dentin and enamel) were not able to distinguish and no significant variation was found in comparison to primary sample teeth (enamel and dentin). The carbonates to phosphate ratios of dentin (permanent and primary) were higher than ratios of enamel (permanent and primary). Lower cross linking index were observed in permanent dentin than the primary dentin. Moreover, the mineral crystallinity of enamel (permanent and primary) was higher compared to the mineral crystallinity of dentin (permanent and primary). However, the trend of composition parameters was similar in all different dataset from different places, but the values were different. These differences might be related to the diet and the nature of that place of sample donor. The relative type of carbonate substitution (substitution for phosphate or hydroxyl ions or presence of labile carbonate of A2) was also found to vary significantly from permanent samples (dentin and enamel) to primary ones. It was found that the $I_B/I_A = 2.7$ and 1.7 in human dentin, approximately 2.3 and 1 in human enamel from permanent Turkish and Germany human teeth samples respectively. On the other hand, the I_B/I_{A+A2} was found to be around 1.5 in human dentin and approximately 1.2 in human enamel of primary teeth samples from German and Turkish places respectively. (Where the I_B is the intensity ratio of B-type carbonate peak at 871 cm^{-1} to the phosphate peak at 960 cm^{-1} , I_A is the intensity ratio of A-type carbonate peak at 878 cm^{-1} to the phosphate peak at 960 cm^{-1}). Moreover, Raman spectroscopy has been successfully

used to estimate the age of Jordanian samples (Archaeological teeth) by using the intensity ratio of CH stretching band at 2941 cm^{-1} to the intense phosphate band at 960 cm^{-1} .

The dentin enamel junction is a critical zone because of its small size. Raman imaging showed that the estimated DEJ width based on different algorithms analysis such as, HCA, K-means cluster and vertex component analysis did not have a fixed width and it varied from $14\text{ }\mu\text{m}$ to $6\text{ }\mu\text{m}$. The analysis of univariate analysis reported that the width is around $4\text{ }\mu\text{m}$ in respect to the intensity ratios of $1450(\text{CH, matrix})/960(\text{P-O, mineral})$, which decreased gradually to nearly zero across the dentin-enamel junction. Spectral differences in both organic and inorganic matrices across the DEJ were also noted. For instance, the amide I and amide III peaks increased within dentin Raman spectra compared to the DEJ Raman spectra. Also the carbonate contents were higher in DEJ than the dentin layer by consideration of higher intensity of carbonate peak at 1070 cm^{-1} . The endmembers derived from the VCA algorithm showed similarity of shape and width of phosphate band at 960 cm^{-1} in DEJ and dentin Raman spectra which mean that the mineral crystallinity of DEJ was not much different in comparison to the dentin crystallinity.

Based on the above findings, possible further research directions include:

More detailed investigation on composition parameters within nanoscale by using further instrumentation such as, SEM, AFM, and XRF.

Large images of whole teeth to detect the transition zone (DEJ) with respect to new software for analysis.

In this work the modern samples provided from Germany (city of Jena) and from city of Hacettepe in Turkey. So, more samples from different countries and different cities will give more understanding of teeth nature and it will give good statistical results.

References

1. N. D. Shashikiran, S. Gunda, V. V. Subba Reddy; Comparison of Resin-Dentine interface in primary and permanent teeth for three different durations of dentine etching. *J., Indian Soc Pedo Prev Dent.* **(2002)** 20 (4): P. 124-131.
2. Ash, M. Major, Jr. and S. J. Nelson; *Dental anatomy, physiology, and occlusion*, 8th ed., Philadelphia: W.B. Saunders, **(2003)** 8th ed., ISBN 0-7216-9382-2
3. Ross, H. Michael, I. Gordon Kaye, P. Wojciech; *Histology: a text and atlas.* **(2003)** 4th edition. Page 450. ISBN 0-683-30242-6.
4. P. F. Gonçalves, E. A. Sallum, A. W. Sallum , M. Z. Casati, S. d. Toledo, F. H. N. Junior; Dental cementum reviewed: Development, structure, composition, regeneration and potential functions. *Braz J Oral Sci.* **(2005)** 4(16): P. 651-658
5. FS.Weine , *Endodontic Therapy*, 5th edn. St Louis: Mosby-Yearbook Inc., **(1996)**: 243.
6. J.W.Simmelink; *Histology of enamel.* In: Avery JK (ed). *Oral development and histology.* Baltimore: Williams & Wilkins, **(1987)**: 140-51.
7. M. d. P.Gutiérrez-Salazar, J. Reyes-Gasga; Microhardness and chemical composition of human tooth. *Materials Research.* **(2003)** 6 (3): P. 367-373.
8. S. F. Rosenstiel, M. F. Land, J. Fujimoto; *Contemporary fixed prosthodontics.* St. Louis: Mosby-Year Book; **(2005)**:51
9. H.H.K. Xu, D.T. Smith, S. Jahanmir, E. Romberg, J.R. Kelly, V.P. Thompson and E.D. Rekow; Indentation damage and mechanical properties of human enamel and dentin. *J Dent Res* **(1998)** 77(3): P. 472-480
10. C. Robinson, J. A. Weatherell , A.S. Hallsworth; Variation in composition of dental enamel within thin ground tooth sections. *Caries Res.* **(1971)** 5: P. 44-57.
11. J. A. Weatherell, C. Robinson, A.S. Hallsworth; Variation in the chemical composition of human enamel. *J. Dent Res.* **(1974)** 53 P. 44-57.
12. Ross, H. Michael, I. Gordon, Kaya, P. Wojciech; *Histology: a text and atlas.* (Baltimore: Lippincott Williams & Wilkins) **(2002)** 4th ed. P. 441
13. A. B. Belcourt, High molecular weight proteins in developing enamel. Their probable interaction. In: *Tooth Enamel IV.* R.W. Fearnhead and S. Suga, eds. Elsevier Science Publishers, Amsterdam, **(1984)** pp. 540-542
14. A. B. Belcourt, A.G. Fincham, and J.D. Termine; Bovine high molecular weight amelogenin proteins. *Calcif. Tissue Int.* **(1983)**, 35: P. 111-114.
15. R. K. Nalla, J.H. Kinney, A. P. Tomsia AP, R. O. Ritchie. Role of alcohol in the fracture resistance of teeth. *J Dent Res.* **(2006)** 85(11): P. 1022-6.
16. R. K. Nalla, J.H. Kinney, A. P. Tomsia AP, R. O. Ritchie. Role of alcohol in the fracture resistance of teeth. *J Dent Res.* **(2006)** 85(11): P. 1022-6.
17. S. J. Jones, A. Boyde; *Ultrastructure of dentin and dentinogenesis.* In: *Dentin and dentinogenesis.* Linde J, editor. Boca Raton: CRC Press, **(1984)** P. 81-134
18. M. G. Buonocore; A simple method of increasing the adhesion of acrylic filling materials to enamel surfaces. *J Dent Res.* **(1955)** 34: P. 849-853
19. R. Garberoglio, M. Brännström; Scanning electron microscopic investigation of human dentinal tubules. *Arch Oral Biol* **(1976)** 21: P. 355-362

20. D. H. Pashley; Dentin: A dynamic substrate- a review. *Scanning Microscop* (1989) 3: P. 161-174.
21. T. Yamada, K. Nakamura, M. Iwaku, T. Fusayama. The extent of the odontoblastic process in normal and carious human dentin. *J Dent Res.* (1983) 62: P. 789-802.
22. W. T. Butler; Dentin extracellular matrix and dentinogenesis. *Oper Dent.* (1992) 5: P. 18-23
23. R. Z. LeGeros; Calcium phosphates in enamel, dentine and bone; in Myers HM (ed): *Calcium Phosphates in Oral Biology and Medicine.* Basel, Karger, (1991) 15 P. 108–129
24. G. W. Marshall, Jr, S. J. Marshall, J. H. Kinney, M. Balooch; The dentin substrate: structure and properties related to bonding. *J. Dent.* (1997): 25(6) P. 441-58
25. E. Mahoney, F. S. Ismail, N. Kilpatrick, M. Swain; Mechanical properties across hypomineralized/hypoplastic enamel of first permanent molar teeth. *Eur. J. Oral Sci.* (2004) 112 (6):P. 497–502
26. S. J. Marshall, M. Balooch, S. Habelitz, G. Balooch, R. Gallagher, G. W. Marshall; The dentin–enamel junction—a natural, multilevel interface. *Journal of the European Ceramic Society.* (2003) 23: P. 2897–2904
27. D. K. Whittaker; The enamel–dentine junction of human and *Macaca irus* teeth: a light and electron microscopic study. *J. Anat.*, (1978) 125 P. 323–335
28. S. Bechtle, T. Fett, G. Rizzi, S. Habelitz, A. Klocke, G. A. Schneider; Crack arrest within teeth at the dentinoenamel junction caused by elastic modulus mismatch. *J.biomaterials.* (2010).01.127: P. 1- 20
29. P. Tafforeau, T. M. Smith; Nondestructive imaging of hominoid dental microstructure using phase contrast X-ray synchrotron microtomography. *Journal of Human Evolution.* (2008) 54 P. 272- 278
30. C. P. Lin, W. H. Douglas, S. L. Erlandsen; Scanning electron microscopy of type I collagen at the dentin–enamel junction of human teeth. *J. Histochem. Cytochem.* (1993) 41, P. 381–388
31. C. Xu, X. Yao, M. P. Walker, and Y. Wang; Chemical / Molecular structure of the dentin-enamel junction is dependent on the intratooth location. *Calcif Tissue Int.* (2009): 84 (3) P. 221- 228.
32. S. T. Rasmussen; Fracture Properties of human teeth in proximity to the dentinoenamel junction. *J Dent Res.* (1984) 63: P. 1279-83
33. C. P. Lin, W. H. Douglas; Structure-property relations and crack resistance at the bovine dentin-enamel junction. *J Dent Res.* (1994) 73: P. 1072-8.
34. V. Imbeni, J. J. Kruzic, G. W. Marshall, S. J. Marshall, R. O. Ritchie; The dentin-enamel junction and the fracture of human teeth. *Nat Mater.* (2005) 4: P. 229-32.
35. G. Balooch, G. W. Marshall, S. J. Marshall, O. L. Warren, S. A. S. Asif, M. Balooch; Evaluation of a new modulus mapping technique to investigate microstructural features of human teeth. *J Biomech.* (2004) 37: P. 1223-32.
36. I. Urabe, M. Nakajima, H. Sano, J. Tagami; Physical properties at the dentino-enamel junction region. *Am J Dent.* (2000) 13: P. 129-35.
37. R. R. Gallagher, S. G. Demos, M. Balooch, G. W. Marshall, Jr, S. J. Marshall; Optical spectroscopy and imaging of the dentin-enamel junction in human third molars. *J Biomed Mater Res A.* (2003) 64: P. 372–377.
38. S.L.Wen.; Human enamel structure studied by high resolution electron microscopy. *Electron Microscopy Reviews.* (1989) 2 (1): P. 1-16

39. K. Sudarsanan, P. E. Machkie, R. A. Young; Comparison of synthetic and mineral fluorapatite, $\text{Ca}_5(\text{PO}_4)_3\text{F}$, in crystallographic detail. *Mater Res Bull.* (1972) 7, P. 1331-8.
40. J. C. Elliott, P. E. Mackie, R. A. Young; Monoclinic hydroxyapatite. *Science.* (1973) 180, P. 1055-7.
41. F. H. Jones; Teeth and bones: applications of surface science to dental materials and related biomaterials. (2001) 42. P. 75-205.
42. L. Calderin, M. J. Stott; Electronic and crystallographic structure of apatites. *Physical Review.* (2003): B 67, 134106.
43. M. Vallet-Regi, J. M. Gonzalez-Calbet; Calcium Phosphates as Substitution of Bone Tissues. *Progress in Solid State Chemistry.* (2004): 32, P. 1-31
44. R. Zapanta-LeGeros; Calcium phosphates in oral biology and medicine, Karger, (1991) New York, NY, USA.
45. J. C. Elliot; Structure and chemistry of the apatites and other calcium orthophosphates, Elsevier. (1994): Amsterdam, Netherlands.
46. N. Roveri, E. Foresti, M. Lelli, I. G. Lesci, M. Marchetti; Microscopic investigations of synthetic biomimetic hydroxyapatite. *Microscopy: Science, Technology, Applications and Education.* (2010) 3, P. 1868-79.
47. B. Palazzo, M. Iafisco, M. Laforgia, N. Margiotta, G. Natile, C. L. Bianchi, D. Walsch, S. Mann, N. Roveri; Biomimetic hydroxyapatite-drug nanocrystals as potential bone substitutes with antitumor drug delivery properties. *Advanced Functional Materials.* (2007): 17 (13) P. 2180-2188.
48. A. Tampieri, G. Celotti, E. Landi; From biomimetic apatites to biologically inspired composites. *Analitical Bioanalitical Chemistry.* (2005) 381, P. 568-576.
49. M. Iafisco, B. Palazzo, M. Marchetti, N. Margiotta, R. Ostuni, G. Natile, M. Morpurgo, V. Gandin, C. Marzano, N. Roveri; Smart delivery of antitumoral platinum complexes from biomimetic hydroxyapatite nanocrystals, *Journal of Material Chemistry.* (2009): 19, P. 8385-8392
50. S. V. Dorozhkin and E. Matthias; Biological and medical significance of calcium phosphates, *Angewandte Chemie International Edition.* (2002): 41, P. 3130-3146, 2002.
51. G. Daculsi, J. M. Boulter, R. Z. LeGeros, and W. J. Kwang; Adaptive crystal formation in normal and pathological calcifications in synthetic calcium phosphate and related biomaterials," *International Review of Cytolog.* (1997): 172, P. 129-191.
52. Th. Leventouri, A. Antonakos, A. Kyriacou, R. Venturelli, E. Liarokapis, V. Perdikatsis; Crystal structure studies of human dental Apatite as a function of age. *Internatinal Journal of Biomaterials.* (2009): 2009, P. 1155- 60 (Article ID 698547).
53. A. Bigi, E. Boanini, C. Capuccini, and M. Gazzano; Strontium-substituted hydroxyapatite nanocrystals. *Inorganica Chimica Acta.* (2007) 360, P. 1009-1016.
54. N. K. Tripathy, P. N. Patel, and A. Panda, "Preparation, IR, and lattice constant measurements of mixed (Ca + Cu + Zn) hydroxylapatites. *Journal of Solid State Chemistry.* (1989): 80, P. 1-5
55. A. Bigi, E. Foresti, M. Gandolfi, M. Gazzano, and N. Roveri; Inhibiting effect of zinc on hydroxylapatite crystallization. *Journal of Inorganic Biochemistry.* (1995) 58, P. 49-58,
56. S. V. Chiranjeevirao, J. Hemmerle, J. C. Voegel, and R. M. Frank; A method of preparation and characterization of magnesium-apatites. *Inorganica Chimica Acta,* (1982): 67, P. 183-187

57. A. Bigi, G. Falini, E. Foresti, A. Ripamonti, M. Gazzano, and N. Roveri; Magnesium influence on hydroxyapatite crystallization. *Journal of Inorganic Biochemistry*. **(1993)**: 49, P. 69-78.
58. M. D. O'Donnell, Y. Fredholm, A. de Rouffignac, and R. G. Hill; Structural analysis of a series of strontium-substituted apatites. *Acta Biomaterialia*. **(2008)**: 4, P. 1455-1464
59. I. R. Gibson, S. M. Best, and W. Bonfield; Chemical characterization of silicon-substituted hydroxyapatite. *Journal of Biomedical Materials Research*. **(1999)**: 44, P. 422-428
60. E. Fujii, K. Kawabata, K. Ando, K. Tsuru, S. Hayakawa, and A. Osaka; Synthesis and structural characterization of silica-hybridized hydroxyapatite with gas adsorption capability. *Journal of the Ceramic Society of Japan*. **(2006)**: 114, P. 769-773
61. A. R. Stéphane, N. Michel, B. A. Didier, R. Christian, D. Philippe, S. Laurent, J. M. Pierre; Behavior of human osteoblastic cells on stoichiometric hydroxyapatite and type A carbonate apatite: Role of surface energy. *Journal of Biomedical Materials Research*. **(2000)**: 50, P. 353-364
62. D. G. Nelson and J. D. Featherstone; Preparation, analysis, and characterization of carbonated apatites. *Calcified Tissue International*. **(1982)**: 34 (2) P. S69-81
63. M. Vignoles, G. Bonel, and R. Young; Occurrence of nitrogenous species in precipitated B-type carbonated hydroxyapatites. *Calcified Tissue International*. **(1987)**: 40, P. 64-70
64. J. Barralet, S. Best, and W. Bonfield; Carbonate substitution in precipitated hydroxyapatite: an investigation into the effects of reaction temperature and bicarbonate ion concentration. *Journal of Biomedical Materials Research*. **(1998)**: 41, P. 79-86
65. K. Haruo, I. Atsuo, M. Shunpei, L. Pierre, O. Kenji, I. Noboru, and T. Tetsuya; Stimulatory effect of zinc-releasing calcium phosphate implant on bone formation in rabbit femora. *Journal of Biomedical Materials Research*. **(2000)**: 50, P. 184-190
66. P. Meunier, C. Roux, E. Seeman, S. Ortolani, J. E. Badurski, T. D. Spector, J. Cannata, A. Balogh, E. M. Lemmel, S. Pors-Nielsen, R. Rizzoli, H. K. Genant, J. Y. Reginster; The effects of strontium ranelate on the risk of vertebral fracture in women with postmenopausal osteoporosis. *New England Journal of Medicine*. **(2004)**: 350, P. 459-468
67. G. Gasquères, C. Bonhomme, J. Maquet, F. Babonneau, S. Hayakawa, T. Kanaya, and A. Osaka; Revisiting silicate substituted hydroxyapatite by solid-state NMR. *Magnetic Resonance in Chemistry*. **(2008)**: 46, P. 342-346
68. L. Yanbao, L. Dongxu, and W. Wenjian; Preparation of nano carbonate-substituted hydroxyapatite from an amorphous precursor. *International Journal of Applied Ceramic Technology*. **(2008)**: 5, P. 442-448
69. T. Attin, B. Dumont, W. Buchalla; Fluoride uptake in caries, eroded and sound enamel after application of a 2000 ppm fluoride solution. *Dtsch Zahnärztl Z*. **(2000)**: 55, P.455-460.
70. H. C. W. Skinner; Biominerals. *Mineralogical Magazine*. **(2005)**: 69, P. 621-641
71. J. Elliott, D. Holcomb, R. Young; Infrared determination of the degree of substitution of hydroxyl by carbonate ions in human dental enamel. *Calcified Tissue International*. **(1985)**: 37, P. 372-375

72. G. Penel, G. Leroy, C. Rey, and E. Bres; MicroRaman spectral study of the PO₄ and CO₃ vibrational modes in synthetic and biological apatites. *Calcified Tissue International*. **(1998)** 63, P. 475-481
73. J. C. Labarthe, G. Bonel, G. Montel; Structure and Properties of B-Type Phosphocalcium Carbonated Apatites, *Ann Chem (Paris)*. **(1973a)**: 8, 289
74. J. C. Elliott, G. Bonel, J. C. Trombe; Space group lattice constants of Ca₁₀(PO₄)₆CO₃. (1980). *J. Appl. Cryst.* **(1980)**: 13, P. 618-621
75. R. M. Wilson, J. C. Elliott, S. E. P Dowker; Rietveld refinement of the crystallographic structure of human dental enamel apatites. *American Mineralogist*. **(1999)**: 81, P. 1406–1414.
76. H. Morgan, R.M. Wilson, J.C. Elliott, S.E.P Dowker, P. Anderson; preparation and characterization of monoclinic hydroxyapatite and its precipitated carbonate apatite. *Biomaterials*. **(2000)**: 21, P. 617-627
77. G. Xu, I. A. Aksay, J. T. Groves; Continuous crystalline carbonate apatite thin films, A biomimetic approach. *Journal of the American Chemical Society*. **(2001)**: 123, P. 2196-2203.
78. C. Rey, A. Hina; Surface reactivity of bone mineral crystals, a model for bioactive orthopaedic materials, *Bioceramics*. **(1995)**: 8, P. 55-60.
79. C. Rey, V. Renugopalakrishnan, B. Collins, M. J. Glimcher; A resolution-enhanced fourier transform infrared spectroscopic study of the CO₃²⁻ ion in the mineral phase of enamel during its formation and maturation. *Calcified Tissue International*. **(1991)**: 49, P. 259-268.
80. R. A. Pekauskas, I. Pullman; Radiogenetic free radicals as molecular traps in bone. *Calcified Tissue Research*. **(1978)**: 25, P. 37-43.
81. Y. Seutsugu, I. Shimoya, J. Tanaka; configuration of carbonate ions in apatite structure determined by polarized infrared spectroscopy. *Journal of the American Ceramic Society*. **(1998)**: 81, P. 746-748
82. D. G. A. Nelson, B. E. Williamson; Low temperature laser Raman spectroscopy of synthetic apatite and dental enamel. *Australian Journal of Chemistry*. **(1982)**: 35, P. 715-727.
83. R. Legros, N. Balmain, and G. Bonel; Structure and composition of the mineral phase of periosteal bone. *Journal of Chemical Research*. **(1986)** P. 8-9.
84. K. Beshah, C. Rey, M. J. Glimcher, M. Schimizu, and R. G. Griffin; Solid state carbon-13 and proton NMR studies of carbonate-containing calcium phosphates and enamel. *Journal of Solid State Chemistry*. **(1990)**: 84, P. 71-81,
85. M. R. Rogel, H. Qiu, G. A. Ameer; The role of nanocomposites in bone regeneration. *J Mater Chem*. **(2008)**:18, P. 4233–41.
86. S. Weiner, H. D. Wagner; The material bone: structure-mechanical function relations. *Annu Rev Mater Sci*. **(1998)**: 28, P. 271–98
87. E. A. Cowles, M. E. DeRome, G. Pastizzo, L. L. Brailey, G. A. Gronowicz; Mineralization and the expression of matrix proteins during in vivo bone development. *Calcif. Tissues Int*. (1998): 62 (1), P. 74-82
88. H. Ehrlich, P. G. Koutsoukos, K. D. Demadis, O. S. Pokrovsky; Principles of demineralization: Modern strategies for the isolation of organic frameworks. Part II. Decalcification, *Micron*. **(2009)**: 40, P. 169-193

89. R. Mendelsohn, A. Hassankhani, E. DiCarlo, A. L. Boskey; FT-IR microscopy of endochondral ossification at 20 μ spatial resolution. *Calcified Tissue International*. **(1989)**: 44(1), P. 20-24.
90. C. Rey, K. Beshah, R. Griffin, M. J. Glimcher; Structural studies of the mineral phase of calcifying cartilage. *Journal of Bone and Mineral Research*. **(1991)**: 6(5) P. 515-525.
91. C. P. Tarnowski, M. A. Ignelzi Jr, M. D. Morris; Mineralization of developing mouse calvaria as revealed by Raman microspectroscopy. *Journal of Bone and Mineral Research*. **(2002)**: 17(6), P. 1118-1126.
92. I. About, M. J. Bottero, P. de Denato, J. Camps, J. C. Franquin, T. A. Mitsiadis; Human dentin production in vitro. *Experimental Cell Research*. **(2000)**: 258(1), P. 33-41.
93. E. Atti, S. Gomez, S. M. Wahl, R. Mendelsohn, E. P. Paschalis, A. L. Boskey; Effects of transforming growth factor-beta deficiency on bone development: a Fourier transform-infrared imaging analysis. *Bone*. **(2002)**: 31(6), P. 675-684.
94. B. B. Tomazic, W. E. Brown, F.J. Schoen; Physicochemical properties of calcific deposits isolated from porcine bioprosthetic heart valves removed from patients following 2-13 years function. *Journal of Biomedical Materials Research*. **(1994)**: 28(1), P. 35-47.
95. N. P. Camacho, W. J. Landis, A. L. Boskey; Mineral changes in a mouse model of osteogenesis imperfecta detected by Fourier transform infrared microscopy. *Connective Tissue Research*. **(1996)**: 35(1-4), P. 259-265.
96. L. M. Miller, J. T. Novatt, D. Hamerman, C. S. Carlson; Alterations in mineral composition observed in osteoarthritic joints of cynomolgus monkeys. *Bone*. **(2004)**: 35(2), P. 498-506.

97. E. P. Paschalis, O. Jacenko, B. Olsen, R. Mendelsohn, A. L. Boskey; Fourier transform infrared microspectroscopic analysis identifies alterations in mineral properties in bones from mice transgenic for type X collagen. *Bone*. **(1996)** 19(2), P. 151-156.
98. E. P. Paschalis, F. Betts, E. Di Carlo, R. Mendelsohn, A. L. Boskey; FTIR microspectroscopic analysis of normal human cortical and trabecular bone. *Calcified Tissue International*. **(1997)**: 61(6), P. 480-486.
99. K. Gökduman; Effects of hydrogen peroxide bleaching on human dentin and enamel microstructure and function: Middle East Technical University, **(2005)**. P. 75
100. A. Carden, M. D. Morris; Application of vibrational spectroscopy to the study of mineralized tissues (review). *J Biomed Opt*. **(2000)**: 5(3), P. 259-68.
101. L. Bachmann, R. Diebolder, R. Hibst, D. M. Zzell; Infrared absorption bands of enamel and dentin tissues from human and bovine teeth. *Appl Spectr Rev*. **(2003)**:38(1), P. 1-14.
102. Y. Liu, Hsu C-YS; Laser-induced compositional changes on enamel: A FT-Raman study. *J Dent*. **(2007)**: 35, P. 226-30.
103. G. Penel, G. Leroy, C. Rey, E. Bres; MicroRaman spectral study of the PO₄ and CO₃ vibrational modes in synthetic and biological Apatites. *Calcif Tissue Int*. **(1998)**: 63, P. 475-81.
104. A. Boskey, N.P.Camacho; FT-IR imaging of native and tissue engineered bone and cartilage. *Biomaterials*, **(2007)**: 28, p. 2465-2478.

105. C. I. Smith, C. M. Nielsen-March, M. E. E. Jans, M. J. Collins; Bone diagnosis in the European Holocene I: patterns and mechanisms. *Journal of Archaeological science* (2007): 34, p. 1485-1493.
106. D. Pienkowski, T. M. Doers, M. C. Monier-Faugere, Z. Geng, N. P. Camacho, A. L. Boskey, H. H. Malluche; Calcitonin alters bone quality in beagle dogs. *J Bone Miner Res.* (1997):12, P. 1936–1943
107. E. P. Paschalis, K. Verdelis, S. B. Doty, A. L. Boskey, R. Mendelsohn, M. Yamauchi; Spectroscopic characterization of collagen cross-links in bone. *J Bone Miner Res.* (2001):16, P. 1821–1828
108. R. K. Nalla, M. Balooch, J. W. Ager JW 3rd, J. J. Kruzic, J. H. Kinney, R. O. Ritchie; Effect of polar solvent on the fracture resistance of dentin: role of water hydration. *Acta Biomater.* (2005): 1 (1), P. 31-43.
109. E.P. Paschalis, E. DiCarlo, F. Betts, P. Sherman, R. Mendelsohn, A.L. Boskey; FTIR microspectroscopic analysis of human osteonal bone. *Calcif. Tissue Int.* (1996): 59, P. 480-487
110. A. Awonusi, M. Morris, M. Tecklenburg; Carbonate assignment and calibration in the Raman spectrum of apatite. *Calcif. Tissue Int.* (2007): 81 (1), P. 46-52.
111. D. Farlay, G. Panczer, C. Rey, P. Delmas, G. Boivin; Mineral maturity and crystallinity index distinct characteristic of bone mineral. *J Bone Miner Metab.* (2010): 28 (4), P. 433-445.
112. L. M. Miller, V. Vairavamurthy, M. R. Chance, R. Mendelsohn, E. P. Paschalis, F. Betts, A. L. Boskey; In situ analysis of mineral content and crystallinity in bone using infrared micro-spectroscopy of the ν_4 PO_4^{3-} vibration. *Biochim Biophys Acta.* (2001): 1527, P. 11-19.
113. D. Faibish, S. M. Ott, A. L. Boskey; Mineral changes in osteoporosis: A review. *Clinical Orthopaedics and Related Research.* (2006): 446, P. 28-38.
114. E. P. Paschalis, E. Shane, G. Lyritis, G. Skarantavos, R. Mendelsohn, A. L. Boskey; Bone fragility and collagen cross-links. *J Bone Res.* (2004): 19 (12), P. 2000-2004
115. A. Carden, R. A. Rajachar, M. D. Morris, D. H. Kohn; Ultrastructural Changes Accompanying the Mechanical Deformation of Bone Tissue: A Raman Imaging Study. *Calcified Tissue Int.* (2003):72, P. 166–175.
116. M. D. Morris, W. F. Finney; Recent development in Raman and infrared spectroscopy imaging of bone tissue. *Spectroscopy-an International Journal.* (2004): 18 (2), P. 155-159.
117. K. Otsubo, E. P. Katz, G. L. Mecham, M. Yamauchi; The COOH terminal locus of free aldehyde in bone collagen: The loss of crosslinking connectivity with mineralization. *Biochemistry.* (1992): 31, P. 396–402
118. S. B. Finn; Morphology of the primary teeth. In: Finn SB, editor. *Clinical pedodontics*. 4th ed. Philadelphia: WB Saunders; (1973).
119. A. F. S. Borges, R. A. Bitar, K. R. Kantovitz, A. B. Correr, A. A. Martin, R. M. Puppini-Rontani; New perspectives about molecular arrangement of primary and permanent dentin. *Applied Surface Science.* (2007): 254, P. 1498–1505
120. P. Spencer, Y. Wang, M. P. Walker, J. R. Swafford. Molecular structure of acid-etched dentin smear layers- in situ study. *J Dent Res.* (2001): 80, P. 1801-7.

121. J.D. Featherstone, J.R. Mellberg; Relative rates of progress of artificial carious lesions in bovine, ovine and human enamel. *Caries Res.* (1981): 15, P. 109-114.
122. F. Gilchrist, A. Santini, K. Harley, C. Deery; The use of micro-Raman spectroscopy to differentiate between sound and eroded primary enamel. *Int J Paediatr Dent.* (2007): 17 (4), P. 274-280
123. G. Kingberg, C. Hagberg, J. G. Noren, S. Nietzsche; Aspects on dental hard tissues in primary teeth from patient with Ehlers-Danlos syndrome. *Int J Paediatr Dent.* (2009): 19 (4), P. 282-90.
124. K. Verdeils, L. Lukashoval, J. T. Wright, R. Mendelsohn, M. G. Peterson, S. Doty, A. L. Boskey; Maturation changes in dentin mineral properties. *Bone.* (2007): 40 (5), P. 1399-407.
125. V. Zavala-Alonso, J. P. Loyola-Rodriges, H. Terrones, N. Patino-Marin, G. A. Martinez-Castanon, K. Anusavice; Analysis of the molecular structure of human enamel with fluorosis using micro-Raman spectroscopy and compare it with that of healthy enamel. *Journal of Oral Science.* (2012): 54 (1), P. 93-98.
126. M. T. Kirchner, H. G. M. Edwards, D. Lucy, A. M. Pollard; Ancient and modern specimens of human teeth: a Fourier transform Raman spectroscopic study. *Journal of Raman Spectroscopy.* (1997): 28, P. 171-178.
127. G. Pezzotti; Raman piezo-spectroscopic analysis of natural and synthetic biomaterials. *Anal Bioanal Chem.* (2005): 381, P.577-90.
128. G. Pezzotti; Introducing a unique measurement for biomaterial nanomechanics. *Key Eng Mater.* (2003): 240-242, P. 893-900.
129. J. A. Timlin, A. Carden, M. D. Morris, R. M. Rajachar, D. H. Kohn; Raman spectroscopic imaging markers for fatigue-related microdamage in bovine bone. *Anal Chem.* (2000): 72, P. 2229-36.
130. R. Z. LeGeros, G. Bonel, R. Legeros; Types of H₂O in human enamel and in precipitated apathies. *Calcif Tissue Res.* (1978):26, P. 111-8.
131. M. G. Sowa, H. H. Mantsch; FT-IR photoacoustic depth profiling spectroscopy of enamel. *Calcif Tissue Int.* (1994): 54, P. 481-5.
132. P. Fattibene, A. Caros, V. De Coste, A. Sacchetti, A. Nucara, P. Postrino, P. Dore; A comparative EPR, infrared and Raman study of natural and deproteinated tooth enamel and dentin. *Phys Med Biol.* (2005): 50P. 1095-108.
133. S. H. Bayari C. Krafft, S. Ide, J. Popp, G. Guven, Z. C. Cehrelif, E. H. Soyug; Investigation of adhesive–dentin interfaces using Raman microspectroscopy and small angle X-ray scattering. *J.Raman Spectrosc.* (2011): 43 (1), P. 6-15.
134. Y. Wang, P. Spencer; Hybridization efficiency of the adhesive dentin inter-face with wet bonding. *J. Dent. Res.* (2003): 82, P. 141-145
135. Y. Wang, P. Spencer; Physicochemical interactions at the interfaces between self-etch adhesive systems and dentin. *J. Dent.* (2004): 32, P. 567-579
136. M. Sato, M. Miyazaki; Comparison of depth of dentin etching and resin infiltration with single- step adhesive systems. *J. Dent.* (2005): 33, P. 475-484.
137. Y.Wang, P. Spencer, X. M. Yao; Micro-Raman imaging analysis of monomer/mineral distribution in intertubular region of adhesive/dentin interfaces. *J. Biomed. Opt.* (2006): 11, 024005

138. A. Santini, V. Miletic; Comparison of the hybrid layer formed by silorane adhesive, one-step self-etch and rinse system using confocal micro-Raman spectroscopy and SEM. *J. Dent.* **(2008)**: 36, P. 683-691.
139. Y. Zou, S. R. Armstrong, J. L. Jessop, Quantitative analysis of adhesive resin in the hybrid layer using Raman spectroscopy. *Biomed. Mater. Res A.* **(2010)**: 94, P. 288-297
140. R. Parthasarathy, G. Thiagarajan, X. Yao, Y.-P. Wang, P. Spencer, Y. Wang; Application of multivariate spectral analysis in micro-Raman to unveil structural/chemical features of the adhesive/dentin interface. *J. Biomed. Opt.* **(2008)**: 13, 014020
141. K. A. Schulze, M. Balooch, G. Balooch, G. W. Marshall, S. J. Marshall; Micro-Raman spectroscopic investigation of dental calcified tissues. *J Biomed Mater Res.* **(2004)**: 69A, P.286-93.
142. Y. Liu, Hsu C-YS. Laser-induced compositional changes on enamel: A FT-Raman study. *J Dent.* **(2007)**: 35, P. 226-30.
143. B. Schrader; *Infrared and Raman spectroscopy.* VCH publisher, weinheim. **(1995)**
144. J. R. Ferraro, K. Nakamoto; *introductory Raman spectroscopy.* Academic press, Boston, **(1994)**.
145. E. Smith, G. Dent, *Modern Raman spectroscopy: A practical approach.* J. willey, Hoboken. **(2005)**.
146. H.G.M. Edwards, J. M. Chalmers, *Raman spectroscopy in archaeology and art history.* The Royal Society of Chemistry. Cambridge, **(2005)**.
147. P. F. McMillan, A. M. Hofmeister; *Infrared and Raman spectroscopy,* in Hawthorne, F. C., (Ed), *Review in Mineralogy.* **(1988)**: 18 (99).
148. F. Sibert, P. Hilderbrandt; *Vibrational Spectroscopy in Life Science.* Wiley-VCH Verlag GmbH & Co. KGaA, Weinheim. **(2008)**
149. D. C. Harris, M. D. Bertolucci; *Symmetry and spectroscopy: an introduction to vibrational and electronic spectroscopy,* Oxford University Press **(1978)**.
150. P. R. Carey; *Biochemical Applications of Raman and Resonance Raman Spectroscopies.* Academic Press **(1982)**.
151. G. Herzberg; *Molecular spectra and molecular structure II: Infrared and Raman spectra of polyatomic molecules,* Krieger Publishing **(1991)**.
152. E. Goormaghtigh, V. Raussens, J. M. Ruyschaert; *Attenuated total reflection infrared spectroscopy of proteins and lipids in biological membranes.* *Biochim. Biophys. Acta.* **(1999)**: 1422, P. 105–185.
153. N. J. Harrick; *Internal Reflection Spectroscopy.* Harrick Scientific Corporation, Ossining, NY, USA **(1987)**.
154. K. Verdelis, M. A. Crenshaw, E. P. Paschalis, S. Doty, E. Atti, A. L. Boskey; *Spectroscopic imaging of mineral maturation in bovine dentin* *J. Dent. Res.* **(2003)**: 82, P. 697–702.
155. K. L. A. Chan, S. G. Kazarian; *New opportunities in micro- and macro-attenuated total reflection infrared spectroscopic imaging: Spatial resolution and sampling versatility.* *Applied Spectroscopy.* **(2003)**: 57 (4), P. 381-389.
156. M. A. Harthcock, S. C. Atkin; *Imaging with functional group maps using infrared microspectroscopy,* *Applied Spectroscopy.* **(1988)**: 42, p. 449-455.
157. Z. Liu, H. Yu, J. F. MacGregor; *Standardization of line-scan NIR imaging systems,* *Journal of Chemometrics.* **(2007)**: 21, p. 88-95.

158. C. D. Tran; Infrared multispectral imaging: Principles and Instrumentation, Applied Spectroscopy Reviews. **(2003)**: 38, p. 133-153.
159. P. Treado, I. W. Levin, E. N. Lewis; Indium Antimonide (InSb) Focal Plane Array (FPA) Detection for Near-Infrared Imaging Microscopy, Applied Spectroscopy. **(1994)**: 48, p. 607-615.
160. P. J. Treado and M. P. Nelson, Raman imaging in Handbook of vibrational spectroscopy, J. M. Chalmers and P. R. Griffiths, Volume 2, John Wiley & Sons, London. **(2002)**: p. 1429-1459.
161. P. Yu; Application of cluster analysis (CLA) in feed chemical imaging to accurately reveal structural-chemical features of feeds and plants within cellular dimension. J. Agric. Food Chem. **(2005 a)**: 53 (8), P. 2872-2880.
162. P. Yu; An emerging method for rapid characterization of feed structures and feed component matrix at a cellular level and relation to feed quality and nutritive value. Arch. Anim. Nutr. **(2006a)**: 60 (3), P. 229-244.
163. P. Yu, C. R. Christensen, D. A. Christensen, J. J. McKinnon; Ultrastructural-chemical make-up of yellow-seeded (*Brassica rapa*) and brown-seeded (*Brassica napus*) canola within cellular dimensions, explored with synchrotron reflection FTIR microspectroscopy. Can. J. Plant Sci. **(2005)**: 85 (3), P. 533-542.
164. H. Martens and T. Naes; Multivariate Calibration, John Wiley & Sons, Chichester, **(1991)**.
165. P. Paatero, U. Tapper; Analysis of different modes of factor analysis as least squares fit problems, Chemometrics and Intelligent Laboratory Systems. **(1993)**: 18, p. 183-194.
166. R. O. Duda, P. E. Hart and D. G. Stork, Pattern Classification, Wiley-Interscience, Chichester, **(2004)**.
167. A. K. Jain, M. N. Murty, P. J. Flynn; Data clustering: a review. ACM computing surveys. **(1999)**: 31 (3) P. 264 - 323.
168. L. Kaufman, P. J. Rousseeuw; Finding groups in data: an introduction to cluster analysis. Wiley, New York. **(1990)**: P. 342.
169. H. C. Romesburg; Cluster analysis for researchers. Lifetime Learning Publications, Belmont, CA. (1984): P. 334.
170. G. Gan, C. Ma, J. Wu; Data Clustering: Theory, Algorithms, and Applications (ASA-SIAM Series on Statistics and Applied Probability). Society for Industrial and Applied Mathematics Philadelphia, PA. (2007): P. 466.
171. M. P. José Nascimento, M. José Bioucas Dias; Vertex Component Analysis: A Fast Algorithm to Unmix Hyperspectral Data. IEEE Transactions on Geoscience and Remote Sensing. (2005): 43 (4), P. 898-910.
172. W. H. Press, S. A. Teukolsky, W. T. Vetterling, B. P. Flannery; Numerical recipes, in: C: The Art of scientific computing, 2nd edn. Cambridge University Press, Cambridge, **(1996)**.
173. M. L. Johnson, L. M. Faunt; Parameter estimation by least-squares methods. Methods Enzymol. **(1992)**: 210, P. 1-37.
174. V. A. Lorenze-Fonfita, E. Padros; curve-fitting of Fourier manipulated spectra comparison apodisation, smoothing, derivation and deconvolution. Spectrochim. Acta Part A. **(2004)**: 60, P. 2703-2710.
175. H. Susi, D. M. Byler; Resolution-enhanced fourier transform infrared spectroscopy of enzymes. Method in Enzymology. **(1986)**: 130, P. 290-311.

176. P.R. Griffiths, J. A. de Haseth; Fourier transform infrared spectroscopy. Chemical Analysis. **(1986)**: 83. John Wiley & Sons, New York.
177. A. Savitzky, M. J. E. Golay; Smoothing and differentiation of the data by simplified least squares procedures. Analytical Chemistry. (1964): 36, (8), P. 1627-39.
178. M. E. Fleet; Infrared spectra of carbonate apatites: n2-Region bands. Biomaterials. **(2009)**: 30 (8), P. 1473-1481.
179. M. Glimcher; The nature of the mineral phases in bone: biological and clinical implications. Metabolic Bone Disease, **1998**. 3rd ed (CA: 1998): p. 23-51.
180. A. B. Sønju Clasen, I. E. Ruyter; Quantitative Determination of Type A and Type B Carbonate in Human Deciduous and Permanent Enamel by Means of Fourier Transform Infrared Spectrometry. Adv Dent Res. **(1997)**: 11(4), P. 523-527.
181. A. L. Boskey; Bone mineralization. In: Bone Mechanics Handbook. Boca Raton, Florida: S.C. Cowin (Ed) CRC Press **(2001)**.
182. D. Pienkowski, T. M. Doers, M. C. Monier-Faugere, Z. Geng, N. P. Camacho, A. L. Boskey, H. H. Malluche; Calcitonin alters bone quality in beagle dogs. J Bone Miner Res. **(1997)**: 12(11): p. 1936-43.
183. A. B. Barry, H. Zhuang, A. A. Baig, W. I. Higuchi; Effect of Fluoride Pretreatment on the Solubility of Synthetic Carbonated Apatite. Calcif Tissue Int. **(2003)**: 72 (3), P. 236-242.
184. J. Y. Exposito, C. Cluzel, R. Garrone, C. Lethias; Evolution of collagens. Anat Rec. **(2002)**: 268 (3), P. 302-316
185. R. P. Boot-Handford, D. S. Tuckwell; Fibrillar collagen: the key to vertebrate evolution? A tale of molecular incest. Bioessays. **(2003)**: 25, P. 142-151.
186. A. J. Bailey, R. G. Paul, L. Knott; Mechanisms of maturation and ageing of collagen. Mech Ageing Dev. **(1998)**: 106, P. 1-56.
187. L. Knott, A. J. Baily; Collagen cross-links in mineralizing tissues: A review of their chemistry, function, and clinical relevance. Bone. **(1998)**: 22 (3), P. 181-187.
188. M. Yamauchi, E. P. Katz; The post translational chemistry and molecular packing of mineralizing tendon collagens. Connect Tissue Res. **(1993)**: 29, P. 81-98.
189. X. Banse, J. P. Devogelaer, A. Lafosse, T. J. Sims, M. Grynopas, et al; Cross-link profile of bone collagen correlates with structural organization of trabeculae. Bone. (2002): 31, P, 70–76
190. L. Knott, J. F. Tarlton, A. J. Baily; Chemistry of collagen cross-linking: biochemical changes in collagen during the partial mineralization of turkey leg tendon. Biochem. J. **(1997)**: 322, P. 535-542.
191. M. H. Wassen, J. Lammenes, J. M. te Koppele, et al; Collagen structure regulates fibril mineralization in osteogenesis as revealed by cross-links pattern in calcifying callus. J Bone Min. Res. **(2000)**: 15, P. 1776-1785.
192. R. D Blanke, T. H. Baldini, M. Kaufman, S. Bailey, et al; Spectroscopically determined collagen Pyr/deH-DHLNL cross-link ratio and crystallinity indices differ markedly in recombinant congenic mice with divergent calculated bone tissue strength. Connect Tissue Res. **(2003)**: 44, P.134–142.
193. J. D. Brady, S. P. Robins; Structural characterization of pyrrolic cross-links in collagen using a biotinylated Ehrlich's reagent. J Biol. Chem. **(2001)**: 276, P. 18812-18818.

194. M. Adamczyk, D. D. Johnson, R. E. Reddy; Collagen cross-links. Synthesis of immunoreagents for development of assays for deoxypyridinoline, a marker for diagnosis of osteoporosis. *Biocunjug Chem.* **(2000)**: 11 (1), P. 124-130.
195. X. Changqi, K. Kunal, Y. Xiamei, W. Yong; Molecular Structural analysis of noncarious Cervical Sclerotic dentin using Raman Spectroscopy. *Journal of Raman Spectroscopy.* **(2009)**: 40 (12), P. 1780-1785.
196. Y. Aıl, I. N. Springer, J. G. Prasse, J. Hedderich, S. Jepsen; Concentration of collagen cross-links in human dentin bears no relation to the individual age. *Int J Legal Med.* **(2002)**: 116 (6), P. 340-343.
197. S. J.Gadaleta, W. J. Landis, A. L. Boskey, R. Mendelsohn; Polarized FT-IR Microscopy of Calcified Turkey Leg Tendon. *Connect Tissue Res.* **(1996)**: 34 (3), P. 203-211.
198. E. C. Moreno, T. Aoba; Comparative solubility study of human dental enamel, dentin, and hydroxyapatite. *Calcif Tissue Int.* **(1991)**: 49, P. 6-13.
199. Y. C. Chiang, B. S. Lee, Y. L. Wang, Y. A. Cheng, Y. L. Chen, J. S. Shiau, D. M. Wang, C. P.Lin; Microstructural changes of enamel, dentin-enamel junction, and dentin induced by irradiating outer enamel surface with CO₂ laser. *Lasers Med Sci.* **(2008)**: (23), P. 41-48.
200. P. Tramini, B. Pélissier, J. Valcarcel, B. Bonnet, L. Maury; A Raman spectroscopic investigation of dentin and enamel structures modified by lactic acid. *Caries Res.* **(2000)**: 34 (3), P. 233-240.
201. L. C. Bonar, A. H. Roufousse, W. K. Sabine, M. D. Grynepas, M. J. Glimcher; X-ray diffraction studies of the crystallinity of bone mineral in newly synthesized and density fractionated bone. *Calcified Tissue International.* **(1983)**: 35 (2), P. 202-209.
202. A. Bertoluzza, P. Brasili, L. Castri, F. Facchini, C. Fagnano, A. Tinti; Preliminary result in dating human skeletal remains by raman spectroscopy. *J. Raman Spec.* **(1997)**: 28, P. 185-188.
203. P. Tafforeau, T. M. Smith; Nondestructive imaging of hominoid dental microstructure using phase contrast X-ray synchrotron microtomography. *Journal of Human Evolution.* **(2008)**: 54, P. 272- 278.
204. P. W. Lucase; Dental functional morphology: how teeth work. Cambridge University Press, Cambridge, UK **(2004)**.
205. G. W. Marshall Jr, M. Balooch, R. R. Gallagher, S. A. Gansky, S. J. Marshall; Mechanical properties of the dentinoenamel junction: AFM studies of nanohardness, elastic modulus, and fracture. *J Biomed Mater Res.* **(2001)**: 54, P. 87–95.
206. B. G. Frushour , J. L. Koenig; Raman scattering of collagen, gelatin, and elastin. *Biopolymers.* **(1975)**: 14, P. 379–391.
207. Y. Wang, P. Spencer; Analysis of acid-treated dentin smear debris and smear layers using confocal Raman microspectroscopy. *J Biomed Mater Res.* **(2002)**: 60, P.300–308.
208. V. Renugopalakrishnan, L. A. Carreira, T. W. Collette, J. C. Dobbs, G. Chandraksasan, R. C. Lord; Nonuniform triple helical structure in chick skin type I collagen on thermal denaturation: Raman spectroscopic study. *Z Naturforsch [C]* **(1998)**: P. 53:383–388.
209. M. Kazanci, P. Roschger, E. P. Paschalis, K. Klaushofer, P. Fratzl; Bone osteonal tissues by Raman spectral mapping: orientation-composition. *J Struct Biol.* **(2006)**: 156, P.489–496.

210. T. Nagano, S. Oida, H. Ando, K. Gomi, T. Arai, M. Fukae; Relative levels of mRNA encoding enamel proteins in enamel organ epithelia and odontoblasts. *J Dent Res.* **(2003)**: 82, P.982–986.
211. C. Begue-Kir, P. H. Krebsbach, J. D. Bartlett, W. T. Butler; Dentin sialoprotein, dentin phosphoprotein, enamelysin and ameloblastin: tooth-specific molecules that are distinctively expressed during murine dental differentiation. *Eur J Oral Sci.* **(1998)**: 106, P. 963–970.
212. A. Nanci, S. Zalzal, P. Lavoie, M. Kunikata, W. Chen, P. H. Krebsbach, et al; Comparative immunochemical analyses of the developmental expression and distribution of ameloblastin and amelogenin in rat incisors. *J Histochem Cytochem.* (1998): 46, P.911–934.
213. E. C. Moreno, T. Aoba. Comparative solubility study of human dental enamel, dentin, and hydroxyapatite. *Calcif Tissue Int.* (1991): 49, P.6–13.